

Inaugural dissertation
for
obtaining the doctoral degree
of the
Combined Faculty of Mathematics, Engineering and Natural
Sciences
of the
Ruprecht - Karls - University
Heidelberg

Presented by
M.Sc. Carlo Bevilacqua
born in: Trani, Italy
Oral examination on 25.10.2022
Heidelberg, Germany

**Advancing Brillouin microscopy as
a tool for studying mechanical
properties in biology with high
resolution**

Referees: Dr. Alba Diz-Muñoz
Prof. Thomas Greb

Abstract

Biological systems are first of all physical systems whose function (or malfunction) is also determined by their response to external and internal forces as well as their physical properties. Therefore, measuring mechanical properties is not only essential for a complete understanding of cell function and organism development but also invaluable in disease diagnosis and treatment. Several techniques are available in the field of mechanobiology (an emerging field that focuses on the role of mechanical forces and properties in biology) to measure mechanical properties but they all virtually rely on analyzing the response of the sample to an external perturbation and have limited three-dimensional capabilities. Instead, Brillouin microscopy is a purely optical technique that requires no contact and no external mechanical perturbation of the sample and can provide 3D maps of viscoelastic properties with (sub)micron resolution. Its first demonstration for 3D imaging of biological samples was accomplished in 2007 and, since then, it has gained increasing interest among biologists for its potentialities.

In this context, one of the aims of my PhD project was to facilitate the use of Brillouin microscopy for addressing biological questions. I did this by equipping a state-of-the-art Brillouin microscope with the add-ons necessary for studying living biological samples (confocal fluorescence and environment control) and by writing an intuitive software interface that would allow non-experts to use the microscope with minimal training. In collaboration with biologists, we investigated several biological questions, some of which produced interesting findings (that led to scientific publications) while others are still being explored.

The second aim of my PhD was to tackle two issues that limit current implementations of Brillouin microscopy: limited speed (leading to imaging times in the excess of hours when whole organisms are imaged in 3D) and potential photodamage, especially in light-sensitive samples. I overcame this limitation by designing a line-scanning version of a Brillouin microscope, with particular attention to ensuring physiological mounting of the sample, low photodamage and high spatial resolution. The speed advantage is given by the parallel acquisition of about 100 Brillouin spectra in a single camera acquisition. This allowed us to image fast processes (gastrulation in *Drosophila*), large volumes (*Phallusia* embryos) and follow development of light-sensitive samples (mouse embryos) over two days.

Zusammenfassung

Biologische Systeme sind in erster Linie physikalische Systeme, deren Funktion (oder Fehlfunktion) auch durch ihre physikalischen Eigenschaften sowie deren Reaktion auf äußere und innere Kräfte bestimmt wird. Daher ist die Messung mechanischer Eigenschaften nicht nur für ein umfassendes Verständnis der Zellfunktion und der Entwicklung des Organismus von wesentlicher Bedeutung, sondern auch von unschätzbarem Wert für die Diagnose und Behandlung von Krankheiten. In der Mechanobiologie (einem aufkommenden Gebiet, das sich mit der Rolle mechanischer Kräfte und Eigenschaften in der Biologie befasst) stehen mehrere Techniken zur Messung mechanischer Eigenschaften zur Verfügung. Sie alle beruhen aber praktisch auf der Analyse der Reaktion der Probe auf eine äußere Belastung und haben nur begrenzte Auflösung in 3D. Stattdessen ist die Brillouin-Mikroskopie ein rein optisches Verfahren, das keinen Kontakt und keine externe mechanische Belastung der Probe erfordert und 3D-Karten der viskoelastischen Eigenschaften mit einer Auflösung im (Sub-)Mikrometerbereich liefern kann. Die erste Demonstration dieser Technik für die 3D-Darstellung biologischer Proben erfolgte 2007, und seitdem hat sie unter Biologen aufgrund ihrer Möglichkeiten immer mehr Interesse gefunden.

In diesem Zusammenhang bestand eines der Ziele meines Promotionsprojekts darin, die Nutzung der Brillouin-Mikroskopie für biologische Fragestellungen zu erleichtern. Zu diesem Zweck habe ich ein hochmodernes Brillouin-Mikroskop mit den für die Untersuchung lebender biologischer Proben erforderlichen Zusatzgeräten (konfokale Fluoreszenz und Umgebungskontrolle) ausgestattet und eine intuitive Software-Schnittstelle geschrieben, die es auch Laien ermöglicht, das Mikroskop mit minimaler Schulung zu bedienen. In Zusammenarbeit mit Biologen untersuchten wir mehrere biologische Fragen, von denen einige zu interessanten Ergebnissen und wissenschaftlichen Veröffentlichungen führten, während andere noch in Arbeit sind.

Das zweite Ziel meiner Doktorarbeit war es, zwei Probleme zu lösen, die die derzeitigen Anwendungen der Brillouin-Mikroskopie limitieren: begrenzte Geschwindigkeit (d.h. ganze Organismen benötigen mehrere Stunden um in 3D abgebildet zu werden) und potenzielle lichtinduzierte Schäden, insbesondere bei lichtempfindlichen Proben. Zu diesem Zweck habe ich eine Line-Scanning-Version eines Brillouin-Mikroskops entwickelt, wobei ich besonders darauf geachtet habe, dass die Probe physiologisch gelagert werden kann, die Lichtschädigung gering ist und die räumliche Auflösung hoch ist. Der Geschwindigkeitsvorteil ergibt sich aus der parallelen Aufnahme von etwa 100 Brillouin-Spektren in einer einzigen Kameraaufnahme. So konnten wir schnelle Prozesse (Gastrulation bei *Drosophila*) und große Volumina (*Phallusia*-Embryonen) abbilden und die Entwicklung lichtempfindlicher Proben (Mausembryonen) über zwei Tage verfolgen.

Acknowledgements

The years of my PhD at EMBL have been important not only for my scientific but also for my personal growth, thanks to the many people I have interacted with and supported me. In particular I want to thank:

Robert who has been a great mentor and has always been very supportive and available for discussion and providing feedback.

All the members of my Thesis Advisory Committee, Alba Diz-Muñoz, Thomas Greb, Vikas Trivedi, Lars Hufnagel for providing suggestions and feedback on my project.

Alejandro, Christian and Vera from the electronic workshop who have always been available to discuss and help with any need on the electronics and all the people from the mechanical workshop whose work was essential to put together the microscope, being a small adapter or a large part of the microscope.

All the collaborators whose interest in Brillouin microscopy and dedication in dealing with all the experimental challenges involved made my work in building the microscope worth.

Dima who started the Brillouin project in the lab and helped me to get started with the microscope when I joined the lab.

Giuliano and Tony who had an important role at the start of my scientific career.

All my group members and the people I got to know at EMBL who made a friendly environment and an enjoyable time at work and beside work. Especially Kuba, Ewa, Héctor and Rocío with whom I had a great time and whose company I enjoyed a lot.

My flatmates who I enjoyed the time spent together with at home and the chats over dinner.

My family and in particular my sister for always being supportive.

Finally, the people who read my thesis and provided valuable feedback.

Contents

Abstract	iii
Zusammenfassung	v
Acknowledgements	vii
1 Motivation and introduction	1
1.1 Importance of mechanical properties in biology	1
1.2 Standard tools in mechanobiology	2
1.3 Advantages of Brillouin microscopy	3
1.4 Outline of the thesis	3
2 Principle of Brillouin microscopy	5
2.1 Theory of Brillouin scattering	5
2.1.1 Classical derivation	5
2.1.2 Quantum derivation	6
2.2 Linear theory of elasticity	8
2.3 Viscoelastic behavior	10
2.4 Spatial resolution	12
2.5 Interpretation of Brillouin parameters	14
2.5.1 Shift	14
2.5.2 Linewidth	16
2.5.3 Loss tangent	17
2.5.4 Amplitude	17
2.6 Difference between "Brillouin" and Young's modulus	18
3 Current applications of Brillouin microscopy in biology	21
3.1 Cell biology	21
3.1.1 Animal cells	21
3.1.2 Plant cells	23
3.2 Developmental biology	25
3.3 Medical applications	27
3.3.1 Disease mechanism and diagnosis	27

3.3.1.1	Ophthalmology	30
3.3.2	Tumor biology	32
4	Confocal Brillouin microscope	35
4.1	Motivation	35
4.2	Setup description and characterisation	35
4.2.1	Brillouin illumination and detection	37
4.2.1.1	Spatial resolution	39
4.2.2	Brillouin spectrometer	41
4.2.2.1	Spectral precision	45
4.2.2.2	Spectral resolution	46
4.2.2.3	Extinction	47
4.2.3	Confocal fluorescence	48
4.2.4	Graphical User Interface	51
4.3	Biological projects	54
4.3.1	Imaging sub-micron extra-cellular matrix in zebrafish notochord	54
4.3.2	Mechanical mapping of mammalian follicle development	57
4.3.3	Other projects	60
4.4	Limitations	61
5	Line-scanning Brillouin microscope (LSBM)	63
5.1	Motivation	63
5.2	Design principles and challenges	65
5.2.1	Physiological mounting of the sample	66
5.2.2	Multiplexing with high spatial resolution	66
5.2.3	Reduction of the photodamage	67
5.2.4	Suppression of elastically scattered light	67
5.2.5	Spectral purity of the laser	68
5.2.6	Refractive index heterogeneity in the sample	68
5.3	Setup description and characterisation	70
5.3.1	Microscope body	70
5.3.1.1	Environment control	71
5.3.2	Brillouin illumination and detection	71
5.3.2.1	ASE filter	73
5.3.2.2	Maximizing axial resolution in O-LSBM	75
5.3.2.3	Field of view	77
5.3.3	LSBM spectrometer	78
5.3.3.1	Rb cell for background suppression	81

5.3.3.2	Spatial resolution	83
5.3.3.3	Spectral precision	84
5.3.3.4	Spectral accuracy	85
5.3.3.5	Spectral resolution	87
5.3.4	Lightsheet fluorescence modality of the LSBM	88
5.3.5	Graphical User Interface	89
5.4	Processing of raw spectra	90
5.5	Biological demonstrations	93
5.5.1	Drosophila gastrulation	94
5.5.2	Phallusia	95
5.5.3	Mouse embryo development	99
5.5.4	Conclusions and outlook	101
6	Outlook and conclusions	107
A	VIPA dispersion and spectrometer calibration	111
A.1	VIPA dispersion	111
A.2	Two-stage VIPA spectrometer calibration	112
A.3	Line-scanning spectrometer calibration	114
	Bibliography	115

List of Figures

2.1	Schematic of the momentum conservation for the photon-phonon collision.	7
2.2	Graphic representation of the definition of elastic moduli. Figure taken from https://agilescientific.com/blog/2016/4/28/all-the-elastic-moduli	10
2.3	Frequency dependence of the complex modulus $M = M' + iM''$ in the simplest case where only one relaxation is present. With reference to equation 2.10, $M_0 = \rho c_0^2$ and $M_\infty = \rho c_\infty^2$, where ρ is the density and c the speed of the acoustic wave. ω_b is the frequency at which the complex modulus is probed (Brillouin shift). Figure taken from [23]	11
2.4	Graphical representation of the relevant spatial scales in Brillouin scattering. L_1 is the acoustic wavelength, L_2 the acoustic propagation length and L_3 the scattering volume (i.e. the optical PSF). Figure taken from [26]	13
2.5	Schematic of Brillouin spectrum showing the relevant parameter. Ω is the Brillouin shift, Γ the linewidth and A the amplitude.	14
4.1	Picture of the incubator for environmental control.	36
4.2	Schematic of the optical setup for the confocal Brillouin setup. L = lens, TL = tube lens, PMT = photomultiplier, P = pinhole, EF = emission filter, DM = dichroic mirror, FC = fiber coupler/collimator, QWP = quarter waveplate, HWP = half waveplate, PBS = polarizing beam splitter, S = shutter, FR = Faraday rotator, CL = cylindrical lens.	37
4.3	Step response at the oil/glass interface perpendicularly (x) and along (z) the optical axis of the objectives. A 1.4NA and 1.0 NA objective, commonly used in the setup, are measured. Blue dots are the raw data and the red solid line is a fit with an <i>erf</i> function. The blue solid line is the derivative of the fitted <i>erf</i> (gaussian function).	40

4.4	Principle of the VIPA. Image from https://en.wikipedia.org/wiki/File:Modified_Operational_principle_of_VIPA.jpg .	41
4.5	Optical schematic of the two-stage VIPA spectrometer. FC = fiber coupler/collimator, CL = cylindrical lens, V = VIPA, Sl = slit, L = lens.	42
4.6	Raw output of the spectrometer (without Lyot stop); the signal is from a plastic cuvette filled with distilled water.	44
4.7	Precision histogram obtained by measuring the Brillouin shift of water 440 times (8.3 mW on the sample, 180 ms integration time). The data is fitted with a normal distribution ($\sigma \approx 9MHz$). 45	45
4.8	Linewidth of the laser measured by the spectrometer, which corresponds to its spectral resolution. The blue dots are the raw data while the red solid curve is a Lorentzian fit. Due to the periodicity of the VIPA pattern, multiple laser peaks are visible: in the figure, the two brightest are shown.	46
4.9	Extinction of the Brillouin spectrometer with (blue line) and without (orange line) the Lyot stop. The dotted lines represent the minimum intensity of the Brillouin signal that can be detected.	48
4.10	Excitation (dashed line) and emission (filled curve) of GFP (blue) and mCherry (orange). [Data from https://www.thermofisher.com/order/fluorescence-spectraviewer]	49
4.11	a) Orthogonal projects from a 3D stack of a fibroblast cell; membranes are labeled with CAAX-GFP b) Corresponding Brillouin image from a single plane.	49
4.12	Time diagram of the confocal fluorescence acquisition.	51
4.13	Graphical interface of the LabVIEW program that I wrote for controlling the confocal Brillouin microscope. The brightfield (or fluorescence) image of the sample can be used to select in real-time the ROI (red box), while moving the motorized stage (green arrows) and adjusting the focus (mouse wheel).	52
4.14	Sub-VI that is controlling the Brillouin acquisition. The reconstructed Brillouin image is shown in real-time (providing instantaneous feedback to the experimenter) together with the raw camera image from the spectrometer, the fitted spectrum (to assess the signal quality) and the calibration from the water cuvette (to monitor the drift of the laser).	53

- 4.15 Characterization of the zebrafish notochord at 3 days post fertilization (dpf). Panel a shows a schematic of the notochord both in a lateral (top) and cross section (bottom) view. Panels b-d show microscopy data from a transgenic fish in which sheath cells are labeled with GFP and vacuolated cells are labeled with mCherry. Panel b is a brightfield image with overlapping GFP signal (sheath cells) while panels c and d are maximum projections from fluorescence confocal images. Scale bars, 500 μm in (b), 20 μm in (c and d). The figure was prepared by Héctor Sánchez-Iranzo and published in Bevilacqua et al. [36]. 55
- 4.16 Brillouin imaging of a 3dpf zebrafish notochord. Panel a shows the fluorescence image of the sheath cells and panel b shows the Brillouin shift map in the corresponding region. Note that the different tissues can be clearly distinguished based on the Brillouin shift (m=muscle, vac=vacuole, sh=sheath cells). A line with a higher Brillouin shift can be observed next to the sheath cells. It becomes more visible when acquiring an oversampled image with a step size of 0.1 μm (c-d). (d=dorsal, v=ventral). Figure adapted from [36]. 56
- 4.17 Analysis of thin ECM layer in vivo. The spectra along the ECM are composed by a double Lorentzian peak (a). When plotting the Brillouin shift of the two peaks separately, the high-shift peak is present only in the ECM (b) while the low-shift peak is still clearly distinguishable from the surrounding tissue (c). The ratio between the amplitude of the two peaks (d-e) allows quantifying the thickness of the ECM. The scalebars in b-d are 1 μm . Figure adapted from [36]. 56

- 4.18 Schematic of the developmental cycle of follicles during mouse folliculogenesis. A follicle consists of the oocyte (pink) with its nucleus (blue), surrounded by the somatic cells (orange) and theca cells (gray). The oocyte grows in size during the transition to the secondary follicle stage, followed by the emergence of a fluid-filled lumen (blue) in the antral follicle stage. The oocyte is eventually released during ovulation, and upon fertilization undergoes embryo development. The interstitial tissues of the ovaries comprise stromal cells, extracellular matrix, and vasculature. Figure taken from [39] and made by Chii Jou Chan. 58
- 4.19 Maps of Brillouin shift and the corresponding BLT for a P7 ovarian cortex and the inner tissue (a). Both images were obtained from the same ovary. Primordial follicles (PrF) and primary follicles (PF) reside primarily in the cortex while the secondary follicles (SF) tend to be found in the inner part of the ovary, which shows a higher interstitial BLT. Maps of Brillouin shift and BLT for a P14 ovarian cortex and the inner tissue (b). Similar to P7 ovaries, higher BLT is associated with the inner tissue of the ovaries, compared to the cortex. Scale bar = 40 μ m. Figure taken from [39] and made by Chii Jou Chan. 59
- 4.20 Boxplot of BLT for the outer theca cells versus the inner somatic cell layer of follicles at various stages of development (a). Each data point corresponds to the average signal of somatic or theca cells in one follicle. Boxplot of BLT for oocytes at various stages of follicle development (b). Each data point corresponds to the average signal of one oocyte. N=35, 45, 45, 21 for E17.5 germ cells and oocytes from primordial, secondary, and antral follicle stage, respectively. ***P<0.001. Figure adapted from [39]; plots made by Chii Jou Chan. 59
- 4.21 Top row: Brillouin shift of a P14 ovary when treated with CTK, which digests collagen matrix. CTK leads to a clear increase in the interstitial space (blue) between the primordial follicles at the cortex. Bottom row: Corresponding BLT maps. Scale bar = 40 μ m. Figure taken from [39] and made by Chii Jou Chan. . . 60

- 5.1 a) Principle of lightsheet fluorescence microscopy: a whole plane in the sample is illuminated and imaged on the camera, leading to large multiplexing (a camera can typically have more than 1 million pixels). Figure adapted from [119]. b) In confocal microscopy the illuminated volume is much larger than the imaged volume, thus increasing the portion of the tissue that is potentially affected by photodamage; in contrast in line-scanning microscopy only the imaged region is illuminated. 64
- 5.2 Principle of multiplexing for Brillouin imaging. The Brillouin signal coming from a line on the sample is spectrally dispersed by a VIPA. On the camera one dimension carries the spectral information while the other retains the spatial information. . . 65
- 5.3 Schematic of the inverted SPIM configuration. Two identical water immersion objectives (0.8NA, 40x, WD=3.5mm) are used for illumination and detection respectively. The sample is mounted on a chamber that can be scanned in 3D and it is separated from the immersion liquid by a Fluorinated Ethylene Propylene (FEP) foil. 67
- 5.4 The difference in refractive index between the sample n_s and the surrounding medium n_m causes refraction of both the illumination and detected light, effectively changing the scattering angle θ 69
- 5.5 Comparison of orthogonal (O-LSBM) and epiline (E-LSBM) line-scanning Brillouin microscope modalities. In O-LSBM the illumination (k_i) and detection (k_s) directions form an angle of 90° while in E-LSBM they are parallel. Red color is used in all the subsequent figures when referring to the O-LSBM modality while blue for the E-LSBM modality. Figure adapted from [65]. 70

5.6	a) Mechanical design of the microscope body. The light is delivered to each objective by means of two mirrors that rotate the image of the line so that it is vertical with respect to the optical table. The objectives are mounted in an immersion chamber filled with water. The sample is mounted in a separate chamber (not shown in the figure) that is connected to a 3D stage for scanning the sample. A 3D printed plastic cover forms the incubation chamber for environmental control. b) zoom in on the immersion chamber, containing the heating element for temperature control. Figure adapted from [65]. . . .	71
5.7	Optical schematic of the LSBM microscope. Figure adapted from [65].	72
5.8	Characterisation and filtering of Amplified Spontaneous Emission (ASE) (a) Optical layout of the double-pass ASE filter employed. To stabilize the Fabry-Perot (FP) based filter over a long time a feedback loop is realized via a photodiode, custom-written Arduino software and piezo that adjusts the FP mirror spacing. (b) Optical setup used to measure the ASE (c,d) Plots of ASE spectrum with and without filter few nm (c) and few GHz (d) away from the laser line. The filter suppresses the total ASE (integrated over the whole measured range) by more than 40dB. Figure taken from [65].	74
5.9	Principle of the tunable lens to extend the depth of field of the illumination line to 200 μ m while retaining a thickness of 1.5 μ m. In the case of Gaussian beams, the depth of field is less than 30 μ m when the thickness is 1.5 μ m (a); conversely, when extending the depth of field to 200 μ m the thickness is more than 4 μ m (b). The tunable lens allows scanning a tightly focused Gaussian beam (c), thus effectively extending the depth of field (d).	76
5.10	Calibration curve of the ETL determined by measuring the displacement of the focus spot (visualised by imaging the fluorescence signal from a ICG die in water.) when varying the voltage applied to the controller of the ETL.	77

5.11	<p>Illumination profile along the FOV (measured as the intensity of the Stokes/anti-Stokes spectral peaks in water) for the (a) epi line and (b) orthogonal line geometries, respectively. Note that a relative intensity value of >15% is generally sufficient for reliable Brillouin peak fitting/detection. Figure adapted from [65].</p>	78
5.12	<p>Optical design of the LSBM spectrometer (a) Orthogonal views of the optical components in the LSBM spectrometer with relevant distances; top shows the plane determined by the illumination line and the optical axis of the detection objective, where the BFA of the objective is relayed and appropriately magnified by the optics to the VIPA plane; bottom shows the plane perpendicular to the illumination line, where the image plane is appropriately magnified and relayed by the optics to the VIPA plane. (b) Details of the relay shown in panel a. Figure adapted from [65].</p>	79
5.13	<p>Spatial calibration (μm to pixel) acquired by translating a bead, with steps of $10 \mu\text{m}$, along the x direction and determining its position on the camera. Figure adapted from [65].</p>	80
5.14	<p>Raw spectrum from an intralipid solution in water. a) Raw image from the camera in the spectrometer. Note that the pattern is curved and multiple interference orders can be observed. b) Line profile of the yellow line highlighted in a. The dashed line indicates the intensity envelope covering multiple interference orders.</p>	81
5.15	<p>Hyperfine structure of the D2 line of Rb, acquired with the CoSy unit of the Toptica laser (by measuring the absorption of a Rb cell while scanning the laser wavelength). Note that natural Rubidium is composed by a mixture of Rb^{85} and Rb^{87}, each of which has two absorption lines. The frequency shift between the different lines was determined by Fan Yang by measuring, with a frequency counter, the beating of two lasers, tuned to different absorption peaks.</p>	82
5.16	<p>Absorption of the laser light from a 150mm long (orange line) and 75mm long (blue line) cell filled with pure Rb^{87} as a function of temperature. Figure adapted from [65].</p>	83

- 5.17 Optical resolution quantified from the elastically scattered light from a $0.5\mu\text{m}$ bead (a); The red data points refer to the orthogonal geometry while the blue ones to the epi geometry. Orthogonal views of the same beads used to generate panel a in the O-LSBM (b) and E-LSBM (c). The convention for the axes is the same as in figure 5.5. Figure adapted from [65]. 84
- 5.18 Spectral precision. Panel a shows a histogram of multiple measurements of the Brillouin shift of water in the O-LSBM (red) or E-LSBM (blue) configuration in typical imaging conditions (100ms exposure $\approx 20\text{mW}$. The distributions are fitted to a Gaussian (dark solid line) and their standard deviations (that represent the spectral precision) is written next to them. Note that the average value is different in the two configurations due to the $\sin(\theta)$ dependence of the Brillouin shift (equation 2.3). Panel b shows the spectral precision (standard deviation of multiple measurements) under different illumination energies in the two configurations (red=O-LSBM, blue=E-LSBM). The shaded red region indicates typical imaging conditions. The data is fitted to a line in a log plot and slope ≈ 0.5 indicates a square root dependence, typical of shot noise limited conditions. Figure adapted from [65]. 85
- 5.19 (a) Acquired, raw spectra of the 4 hyperfine D2 spectral lines of Rb^{85} and Rb^{87} as measured by the spectrometer. (b) Frequency shift of the Rb lines in panel a after applying the reconstruction pipeline (see section 5.4); dotted lines represent the exact values (figure 5.15); d is the L1 distance between the measured and the exact values divided by the number of points i.e. the average discrepancy from the true frequency; the FSR is measured to be 15.15GHz by minimizing the sum of d for the 4 Rb lines. (c) left axis: Residuals (i.e. difference between the measured and the known value) of the data in panel b; right axis: position of the Rayleigh peak from the Rb^{87} F=2 line (used as the 'zero') from one order, relative to the previous pixel. Figure adapted from [65]. 86
- 5.20 Spectral resolution of the spectrometer, as measured by the FWHM of the laser line, after applying the reconstruction pipeline (section 5.4). Figure adapted from [65]. 88

- 5.21 Example image of a multicolor SPIM image of a mouse embryo where both membranes and nuclei are fluorescently labelled. 89
- 5.22 The "Fluorescence" tab in the LabVIEW program is used to see fluorescence (or brightfield) images from the sample in real time and determine to ROI. 91
- 5.23 The "Brillouin" tab in the LabVIEW program is used to see the signal from the Brillouin spectrometer in real time and determine signal strength and quality. 91
- 5.24 The "Sequential acquisition" tab in the LabVIEW program controls the assignment of different acquisition modalities (right table) to each sample (left table). Colors help to visually identifying the matching between the two. 92
- 5.25 Performance of the GPU-accelerated spectral analysis pipeline. (a) Brillouin spectrum fitting time as a function of image size (equal to the number of independent spectra), comparing standard, CPU-based fitting routines (Matlab) and our custom GPU-accelerated library. Total analysis time is generally >1000-fold improved with GPU acceleration, making the processing time smaller than the acquisition time. The shaded red region shows the typical length of the Brillouin line in pixels. Note most error bars are smaller than data points. (b) Fitting accuracy between the CPU- and GPU-based pipelines, showing comparable performance. Note that the accuracy uncertainty (1MHz) is negligible compared to the spectral fitting precision based on realistic, noisy data (10-20MHz). The plots were generated by Sebastian Hambura. Figure taken from [65]. 93

5.26 (a) Superficial view of a fixed *Drosophila* embryo undergoing ventral furrow formation (VFF, arrow). The embryo expresses the membrane marker Gap43-mCherry to visualize cell outlines. The green arrowhead indicates the direction of Brillouin illumination which here is orthogonal to the apical surface of cells. Red segmented line indicates the approximate location of physical cross-sections shown in b and c. (b) Stages of VFF progression shown in physical cross-sections of fixed embryos, stained with a Snail antibody (green) to label the nuclei of cells engaged in VFF and a Discs Large antibody (magenta) to label cell outlines. (c) left: Images from a SPIM recording of an embryo expressing Gap43-mCherry to mark cell membranes; right: median-projected Brillouin shift maps from the same embryo at the same timepoints and positions as shown above (representative embryo of $n = 3$ total). The imaged volume is $22 \times 170 \times 71 \mu\text{m}$ (z-increment of $1.5 \mu\text{m}$) with a time resolution of about 2min. The dotted line encloses the presumable mesoderm region within the Brillouin shift maps used for quantification in d. The apical side of cells faces the outer surface of the embryo. (d) Quantification of Brillouin shift averaged over 18 cells engaged in apical constriction and invagination during VFF progression, as inferred from SPIM slices (dotted line in c). Changes in Brillouin shift are shown relative to the Brillouin shift at time-point $0'$, which corresponds to the initiation of apical constriction. Data points are average Brillouin shift within the contractile domain, error bars denote S.D. over different slices. Statistical significance was evaluated using a paired-one-way ANOVA test ($F = 44.29$, $p = 0.066$), followed by a post-hoc multiple comparison test (FDR corrected, $\alpha = 0.05$, q-value = 0.1); * $p = 0.039$, ** $p = 0.0054$. Timescale is minutes. Scale bars are $50 \mu\text{m}$. Figure adapted from [65] and made by Juan Manuel Gomez.

- 5.27 (a) Posterior midgut invagination (PMG) in embryos at a similar stage as in figure 5.26. (Top) mid-sagittal section; inset: higher magnification of the posterior midgut region showing apical constriction and invagination during PMG formation; (bottom) superficial-dorsal view a *Drosophila* embryo showing the formation of the circular contractile domain of the PMG that encloses the Pole Cells (PCs, arrow). The embryo expresses the membrane marker Gap43-mCherry to visualize cell outlines. The green arrowhead indicates the direction of Brillouin illumination which here is orthogonal to the lateral surface of cells. (b) Representative SPIM images (left) and median-projected Brillouin shift maps (right) at five timepoints during invagination (out of $n = 3$ total). The imaged volume is $83 \times 141 \times 46 \mu\text{m}$ (z-increment of $2.5 \mu\text{m}$) with a time resolution of about 2min. Arrowhead indicates the displacement of the posterior end during PMG invagination. The initiation of apical constriction was set as 0' time point. Images in Gap43-mCherry and Brillouin panels are median projections of 3 slices of the re-sliced ROI. Timescale is minutes. Scale bars are $50 \mu\text{m}$. Figure adapted from [65] and made by Juan Manuel Gomez. 97
- 5.28 Schematic of the vegetal hemisphere of a late 16 cells stage *Phallusia* embryo (a), showing the bilateral symmetry. Exemplary O-LSBM image (b) and corresponding SPIM image (c) (membranes labeled with lipophilic dye FM4-64) of the same stage as shown in a (out of $n = 2$ total). The imaged volume is $165 \times 186 \times 172 \mu\text{m}$ (z-increment of $2.5 \mu\text{m}$) within a time of about 17min. Cartoon of the machinery for asymmetric division in two B5.2 germline progenitor cells (d): a thick microtubules bundle directed to the centrosome-attracting body forms on the posterior side of the nucleus. Zoom-in of the gray square in panel b (e) showing a high Brillouin shift in the vicinity of the nucleus that is indicative of a microtubule bundle. Line profile along the line shown in panel e (f). BS, Brillouin shift. Figure adapted from [65]. 98

- 5.29 Imaging of a Phallusia embryo at the tailbud stage (out 389 of $n = 3$ total) (a-d). Orthogonal views (a) and maximum intensity projection (MIP) (b) from the SPIM volume ($195\mu\text{m} \times 191\mu\text{m} \times 111\mu\text{m}$) of membranes labeled with lipophilic dye FM4-64 of a Phallusia embryo at the tailbud stage (late tailbud I). Corresponding orthogonal views (c), acquired with E-LSBM modality, of the volume in panel a. Violin plot (d) showing the Brillouin shift differences of three distinct tissue regions (Epidermis, Central Nervous System (CNS) and Endoderm/Mesoderm) manually-segmented in 3D according to SPIM data in a. The green, yellow and light-blue outlines in panels a and c show the segmented regions for Epidermis, CNS and Endoderm/Mesoderm respectively. BS, Brillouin shift. Figure adapted from [65]. 100
- 5.30 (a) Timeline of mouse embryo development from the one cell stage to late blastocyst. The dashed rectangle encloses the developmental window that was imaged. (b) Exemplary orthogonal views of Brillouin volumes (top, acquired in the O-LSBM) and SPIM volumes (bottom) of a single mouse embryo at the beginning (left) and at end of the timelapse (right, 46h45m after the first timepoint). The acquisition time for one volume in the Brillouin modality was 11-17min, the time interval between volumes is between 77 to 92 minutes. Representative result from $n=4$ embryos. Figure adapted from [65]. 102
- 5.31 (a) Top: SPIM volume (maximum intensity projection - MIP) of an embryo that underwent Brillouin time-lapse imaging, taken at the end of the timelapse. Bottom: SPIM image (MIP) of a control embryo (taken at the same time as the embryo in top panel), that was in the same imaging chamber but not imaged by Brillouin or SPIM, showing qualitatively similar morphology. (b) To further confirm embryo viability, we fixed the embryos after imaging and stained them for cell fate. MIPs through the volume where the outer trophectoderm cells are CDX2-positive (green), a marker for trophectoderm cell fate. The inner cell mass are SOX2-positive (red) and CDX2-negative, indicating proper epiblast fate in the ICM at late blastocyst stage. The number of cells in the ICM is 26, consistent with the reported values in literature [130]. Figure adapted from [65]. 103

- 5.32 a. Brightfield images of an 8-cell stage mouse embryo that eventually undergoes cell death. b. Images of Brillouin shift for the same embryo in (a), showing a loss of Brillouin signals within 6 hours, which is a clear sign of embryo death. The embryo also appears round and decompacted, a sign of abnormality. c. Another representative embryo undergoing cell death under the same imaging condition. Time is shown in hh:mm. Scale bar = 20 μm . Data collected by Chii Jou Chan. Figure taken from [65] and made by Chii Jou Chan. 104
- A.1 Schematic of the VIPA with the relevant parameters from [131] 111
- A.2 Representation of the periodic pattern created by the spectrometer on the camera. In the confocal Brillouin microscope, the shaded grey area is not accessible during the measurement because is blocked by the slits. 112

List of Tables

4.1	Spatial resolution of the confocal Brillouin microscope with two different objectives. The error is the standard deviation and the effective NA is calculated as the value that would theoretically produce the measured axial resolution.	40
-----	--	----

List of Abbreviations

AFM	A tomic F orce M icroscope
CCD	C harge- C oupled D evice
ETL	E lectrically T unable L ens
ECM	E xtra- C ellular M atrix
FWHM	F ull W idth at H alf M aximum
FSR	F ree S pectral R ange
LSBM	L ine- S canning B rillouin M icroscope
NA	N umerical A perture
PBS	P olarizing B eam S plitter
PMT	P hoto M ultiplier T ube
PSF	P oint S pread F unction
ROI	R egion O f I nterest
SNR	S ignal to N oise R atio
SPIM	S elective P lane I llumination M icroscopy
VIPA	V irtually I mages P hased A rray

Chapter 1

Motivation and introduction

Brillouin microscopy is a technique that has recently emerged as a powerful tool to investigate mechanical properties in living biological samples [1]. Before introducing this technique and my work for extending its application in biology, I should first discuss why mechanical properties are interesting in biology and what Brillouin microscopy can add to other tools already used to measure mechanical properties in biological samples.

1.1 Importance of mechanical properties in biology

Mechanobiology is an emerging field at the interface between biology, physics, and bioengineering. The fundamental idea is that biological systems are first of all physical systems, therefore mechanical forces and properties are key contributors to cell behavior and organism development. This concept is not new and was in fact explored at the dawn of developmental biology. But the lack of proper tools and biophysical approaches made the field lose its momentum [2–4]. In the last decades, new technological developments brought a renewed interest in the field and, with that, new insights into the role of mechanical properties in biological systems. In the medical field mechanical measurements can help elucidate the mechanism behind diseases [5] and facilitate their diagnosis [6]. Just as an example, cell elasticity is an indicator of the progression of cells from normal to cancerous state [7]. In cell biology, mechanical properties have been found to play a role in cell differentiation [8], migration [9] and are a key player in organism development [4].

1.2 Standard tools in mechanobiology

Several tools can be used in mechanobiology and I should first introduce them and their limitation to understand what Brillouin microscopy can be advantageous for. Virtually all of them rely on analyzing the deformation of the sample upon an external mechanical load and they differ on how this load is generated and the response is detected.

Atomic Force Microscopy (AFM) consists of a cantilever (whose displacement can be measured very precisely using an optical lever) mounted on a piezo, that allows its positioning with nanometer resolution. Mechanical properties of biological samples can be measured via indentation experiments: a tip of known geometry is mounted on the cantilever and it is used to indent the sample by a known amount (on the order of hundreds of nanometers), controlled with the piezo; the force applied to the sample is extracted from the displacement of the cantilever (that has a known spring constant) and the mechanical properties can be calculated by using an appropriate mathematical model [10].

Micropipette aspiration A glass tube having a diameter of tens of μm (micropipette) is used to apply a known suction pressure to the surface of the cell. In response, the surface is aspirated into the capillary and, by tracking the edge of the surface with a microscope, both the elastic and viscous properties of the cell can be derived from the static and dynamic deformation respectively [11].

Deformability cytometry Cells are deformed by shear stresses and pressure gradients within a constriction in a microfluidic channel. Their shape is monitored in real-time with a fast camera and from there the elasticity can be derived. More than 100 cells/s can be measured with this technique [12].

Optical tweezers Cells are stretched by using optical traps (whose generated force can be calculated) and their mechanical properties are derived from the resulting deformation [13].

Microdroplet deformation Biocompatible ferrofluid microdroplets are injected inside the tissue (thus giving access to the internal structures) and a known magnetic field is applied. The magnetic field generates a dipole force (the net force is zero, so there is no movement of the microdroplet)

that causes a deformation of the microdroplet; from that, the mechanical properties of the surrounding tissue can be derived. The spatial resolution that can be achieved is on the order of tens of μm [14].

Optical Coherence Elastography OCE An external perturbation, that could be either compressive, harmonic (i.e. a sine wave), or transient (i.e. an impulse), is applied to the sample and its response is measured by Optical Coherence Tomography (OCT). The quantification of the displacement of the tissue in different regions provides mechanical contrast, while the quantitative determination of the elastic modulus requires a mathematical model of tissue response. The spatial resolution is limited by both the resolution of OCT (several μm) and by the number of pixels required to estimate the strain, and usually is in the excess of tens of μm [15].

From this short summary, it is clear that these techniques are restricted to measuring mechanical properties of the surface or the tissue as a whole or, when they provide 3D information, they suffer from poor spatial resolution. Importantly, all rely on external loading (force application) which can perturb the native state of the cell or tissue compound.

1.3 Advantages of Brillouin microscopy

Brillouin microscopy exploits the namesake effect, Brillouin scattering, that is the interaction between laser light and spontaneous acoustic waves, present in any matter at finite temperature (see section 2.1). From the spectrum of the scattered light mechanical properties, such as stiffness and viscosity, can be derived (see section 2.5). Being a fully optical technique it is non-contact, has 3D access to the sample (only limited by the penetration of light) and submicrometer spatial resolution (see section 2.4). It is thus clear that it offers several advantages over the "standard" techniques, with some caveats to keep in mind when interpreting the data (see section 2.5 and 2.6).

1.4 Outline of the thesis

In my thesis I will first introduce the physical principle behind Brillouin microscopy (chapter 2), emphasizing the information that can be extracted from a Brillouin measurement and the spatial resolution that can be achieved. I will then summarise the main applications that the technique as found so far

in biology, briefly presenting the main findings (chapter 3). In the following chapters, I will present both a so-called confocal Brillouin microscope as well as line-scanning Brillouin microscope. I developed both of them in the lab and used, in collaboration with biologists, to address biological questions. The confocal system (chapter 4) was already in the lab when I joined and I upgraded it (both from the hardware and the software side) to make it reliable and intuitive to use for non-experts, with the specific aim of facilitating its use for biological applications by several collaborators. I will provide a technical description and characterization of the setup and present some of the biological projects that were made possible by this microscope. In chapter 5 I will present the line-scanning Brillouin microscope, which is the major technical achievement of my PhD. It was designed from scratch by me and Robert Prevedel and built by me. The aim was to solve some of the limitations of the confocal implementation and thus open the doors to studying biological processes that wouldn't be otherwise accessible. I will introduce the design challenges and how we solved them, and present the characterization of the setup and the biological processes that we could now investigate.

Chapter 2

Principle of Brillouin microscopy

2.1 Theory of Brillouin scattering

Brillouin scattering is the interaction of light with acoustic waves within a material. The effect can be understood both in classical electromagnetism and quantum mechanics. I will briefly introduce the main concepts of both interpretations in the next paragraphs.

2.1.1 Classical derivation

A concise mathematical derivation of the classical theory of Brillouin scattering, together with the relevant references, can be found in the supplementary information of Fiore, Bevilacqua, and Scarcelli [16]. Here I will only introduce an intuitive explanation of the phenomenon and the main results.

Photoelasticity is the effect that links a purely mechanical phenomenon (propagation of acoustic waves) to optical scattering. In fact, acoustic waves locally generate strain in the material (see section 2.2) and the photoelastic tensor couples the strain to a change in the dielectric constant¹ ϵ , that describes the optical response of the material. If we consider an acoustic wave with a well-defined wavevector $k_a = 2\pi/\lambda_a$, the corresponding modulation of the dielectric constant (i.e. the refractive index) is periodic, effectively creating a diffraction grating. Light can thus be diffracted² at an angle that satisfies the Bragg condition $\lambda/n = 2\lambda_a \sin \theta/2$, where λ is the wavelength of light in vacuum, n the (unperturbed) refractive index of the material and θ is the angle between the incident and scattered wavevector (i.e. the scattering angle). But, since the wave is traveling, the induced diffraction grating

¹From a molecular point of view, the strain causes a local change in density, that is linked to the dielectric constant via the Clausius-Massotti relation.

²The diffracted light is generated by the time-varying electric polarization, due to the change in dielectric constant induced by the acoustic wave in the material. In fact, the second derivative of electric polarisation with respect to time is a source term in Maxwell equations.

is moving as well at the speed of sound. It is well known that light emitted by a moving source undergoes a Doppler shift; depending on the direction of propagation of the acoustic waves, the Doppler shift can be towards lower or higher frequency. This intuitive explanation makes it clear that the light can be scattered at any angle (that matches the Bragg condition with the wavevector of the acoustic wave) and the spectrum of the scattered light is composed of two symmetric peaks (so-called Stokes and anti-Stokes). The exact expression for the Brillouin frequency shift can be derived from the classical theory, finding the same result predicted by the quantum theory (equation 2.3).

The classical theory also predicts that, independently of the origin of the fluctuations of the dielectric constant, the intensity of the scattered light is proportional to λ^{-4} , when detecting it far from the scattering volume [17]. In fact, the scattering volume can be divided into smaller volumes, each of which is radiating as a dipole, having a characteristic λ^{-4} dependence.

So far I didn't consider the polarisation (i.e. the direction of the electric field) of the incident and the scattered light. For isotropic materials, the direction of the scattered electric field is the same as the incident field, when interacting with longitudinal acoustic waves. Instead, in the interaction with transverse acoustic waves (that are present only if the shear modulus is non-zero), the polarization of the scattered light is rotated by 90° [18].

2.1.2 Quantum derivation

Similar to light, which can be described as a collection of photons (the quantum of the electromagnetic field), collective vibrations (i.e. acoustic waves) can be thought of as a collection of phonons, collective excitations that carry energy and momentum. Therefore, in the quantum picture, Brillouin scattering can be described as a collision between a photon and a phonon: the photon can either lose energy by transferring it to a newly created phonon (Stokes) or gain energy from an already existing phonon (anti-Stokes). In addition to energy conservation, the momentum must be conserved. From these two conditions, the equation for Brillouin scattering can be readily derived. Defining \vec{k}_i the wavevector of the incident light, \vec{k}_s the wavevector of the scattered light and \vec{k}_p the wavevector of the phonon, momentum conservation reads:

$$\vec{k}_s - \vec{k}_i = \pm \vec{k}_p \quad (2.1)$$

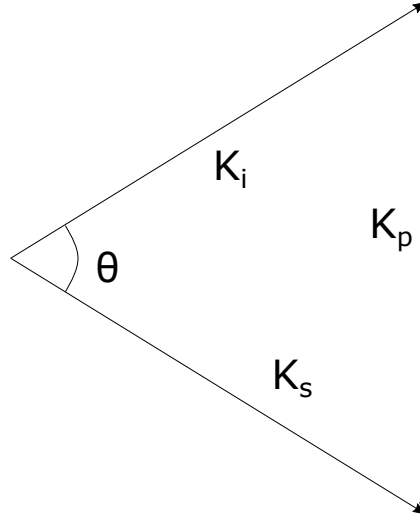


FIGURE 2.1: Schematic of the momentum conservation for the photon-phonon collision.

Since the relative change in wavelength of the scattered light is very small ($\approx 10^{-5}$), the moduli of the incident and scattered wavevectors are almost equal ($k_s \approx k_i$), thus the modulus of their difference can be written as (see figure 2.1):

$$|\vec{k}_s - \vec{k}_i| \approx 2k_i \sin \frac{\theta}{2} \quad (2.2)$$

where θ is the angle between the incident and scattered wavevector (i.e. the scattering angle). By combining equation 2.1 with equation 2.2 and noting that $k_p = 2\pi\Omega/v$ where Ω and v are respectively the frequency and the speed of the probed phonon and that $k_i = 2\pi n/\lambda$ where n is the refractive index within the interaction volume and λ the wavelength of the laser in vacuum, one can derive:

$$\Omega = \frac{2n}{\lambda} v \sin\left(\frac{\theta}{2}\right) \quad (2.3)$$

From the conservation of energy ($\hbar \cdot \Omega$) it follows that Ω is both the frequency of the probed phonon and the shift in the laser frequency induced by the scattering (hereafter named "Brillouin shift" Ω).

The previous derivation assumes that the phonon has an infinite lifetime but in viscous materials, the acoustic waves are dissipated and have a lifetime τ that in typical biological samples is on the order of few ns. Therefore, due to the uncertainty principle, the Brillouin peaks have a linewidth $\Gamma \sim 1/\tau \lesssim 1\text{GHz}$ (hereafter named "Brillouin linewidth" Γ).

In section 2.5 I will describe how both the Brillouin shift and linewidth can provide information on the mechanical properties of the sample.

2.2 Linear theory of elasticity

Equation 2.3 shows that the Brillouin shift is proportional to the speed of sound v , that is in turn related to the elastic properties of the material. To derive the relationship between these two quantities the theory of elasticity in solids needs to be introduced. A rigorous derivation of the elastic waves in crystals can be found in Fedorov [19]. Here I will only introduce the fundamental concepts and the final results. First of all, I should note that the amplitude of the spontaneous acoustic waves probed in Brillouin microscopy is small, so the linear theory of elasticity is an appropriate description of the phenomenon. Also, the wavelength of the probed acoustic waves is much longer than the intermolecular distance, thus the material can be considered a continuum. Therefore one can write a generalized Hooke's law for the most general case of non-isotropic materials; it takes a tensorial form, where the indices refer to the Cartesian coordinates ($i,k,l,m=x,y,z$). Using Einstein's convention, where a summation over repetitive indices is implicit, Hooke's law reads:

$$\sigma_{ik} = c_{iklm} \gamma_{lm} \quad (2.4)$$

where σ_{ik} is a 3x3 stress tensor³, γ_{lm} is a 3x3 strain tensor and c_{iklm} is a 4th order 3x3x3x3 stiffness tensor necessary to link the stress and strain tensors. Out of the 81 components of c_{iklm} only 21 are independent due to symmetry constraints; the 21 independent components can be rearranged in a 6x6 symmetric matrix (that has exactly 21 independent components) and the stress and strain tensor redefined accordingly. Equation 2.4 assumes then a vectorial form:

$$\sigma_i = c_{ij} \epsilon_j \quad (2.5)$$

where $i,j=1,\dots,6$.

The relationship between stress and strain allows us to write Newton's second law, which describes the motion of the infinitesimal elements forming the continuum. It takes the form of a homogeneous second-order differential equation in the displacement vector (related to the strain vector) and one can seek solutions in the form of monochromatic plane waves, defined by a wavevector \vec{k} . If we introduce the matrix

$$\Lambda_{lm} = \frac{c_{ijlm} k_j k_l}{\rho} \quad (2.6)$$

³Two indices are required to indicate both the surface which the stress is applied to and the direction of the stress.

(where ρ is the density, c_{ijlm} is the stiffness tensor, as defined in equation 2.4), the problem of solving the equation of motion turns into an eigenvalue problem (Christoffel equation):

$$\left| \Lambda - v^2 \right| = 0 \quad (2.7)$$

where v is the phase velocity of the acoustic wave. It is important to note that Λ depends on the direction of propagation k (equation 2.6): for each direction there are at most 3 eigenvalues v that fulfill the equation of motion; they correspond to the two transversal and one longitudinal wave.

For an isotropic material the number of independent components in the stiffness tensor c_{ij} is reduced to two [20]:

$$\begin{bmatrix} c_{11} & c_{12} & c_{12} & 0 & 0 & 0 \\ c_{12} & c_{11} & c_{12} & 0 & 0 & 0 \\ c_{12} & c_{12} & c_{11} & 0 & 0 & 0 \\ 0 & 0 & 0 & c_{44} = \frac{c_{11}-c_{12}}{2} & 0 & 0 \\ 0 & 0 & 0 & 0 & c_{44} = \frac{c_{11}-c_{12}}{2} & 0 \\ 0 & 0 & 0 & 0 & 0 & c_{44} = \frac{c_{11}-c_{12}}{2} \end{bmatrix} \quad (2.8)$$

The element c_{11} is the longitudinal modulus M , the quantity that is typically measured in Brillouin experiments. The second independent parameter is either the element c_{12} (Lamé's first parameter λ) or c_{44} (the shear modulus G). The shear modulus G could in principle be measured from Brillouin scattering as well [18]. The challenge here is that its measurement requires the detection of light scattered by transverse acoustic waves, that has a lower cross-section and requires a scattering angle different from 180° (typically employed in Brillouin microscopy). Once M and G are known, all the other moduli can be calculated from them: the bulk modulus $K = M - \frac{4G}{3}$; Young's modulus $E = \frac{G(3M-4G)}{M-G}$; the Lamé's first parameter $\lambda = M - 2G$ and the Poisson's ratio $\nu = \frac{M-2G}{2M-2G}$. A graphical representation of the different moduli can be found in figure 2.2.

If the material is not isotropic, the measurement of M and G must be repeated along its principal axis of symmetry and the complete stiffness tensor can be calculated from them [21].

To conclude I want to highlight that the previous derivation is valid for bulk, homogeneous materials. When the size of the object under investigation becomes smaller, discrete acoustic modes start to arise, that can be rather complex (due to boundary conditions imposed by the shape of the object).

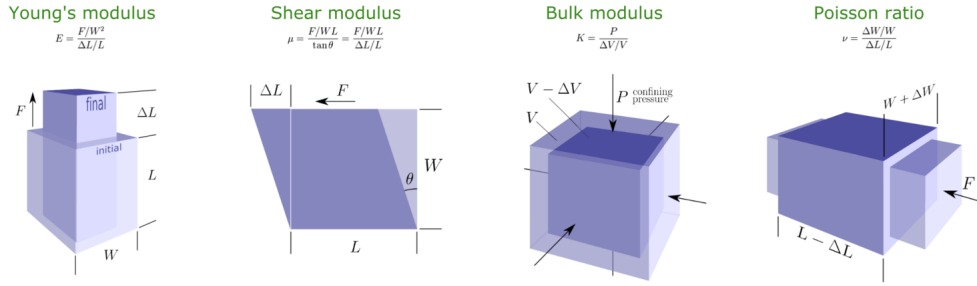


FIGURE 2.2: Graphic representation of the definition of elastic moduli. Figure taken from <https://agilescientific.com/blog/2016/4/28/all-the-elastic-moduli>

Furthermore, the presence of a surface introduces 2D surface waves as well. These effects make modeling of acoustic waves in biological samples particularly challenging, given that they have different components with different dimensions, shapes and mechanical properties.

2.3 Viscoelastic behavior

In section 2.2 I introduced the definition of elastic modulus and how it is related to the response of the material to mechanical perturbations (i.e. acoustic waves probed in Brillouin scattering). In practice, all materials exhibit, to some extent, a viscous response (due to internal dissipation of the energy). The viscous component introduces a time delay between the applied stress and the response of the material and is at the origin of the absorption of acoustic waves. The latter is conveniently described mathematically by introducing a complex modulus:

$$M = M' + iM'' \quad (2.9)$$

where the real part M' , called storage modulus, describes the elastic response and the imaginary part M'' , called loss modulus, the viscous response ($M'' = \omega\eta$ where η is the viscosity). Due to the Kramers–Kronig relations, a non-zero imaginary part implies a frequency dependence of the storage modulus M' and, from physical constraints, it follows that this dependence is an increasing function of the frequency and it is asymptotically approaching a value M_∞ [22]. The general dependence can be rather complex, but for the sake of making some observations, let's discuss the simplest case where the only source of viscous response is a single relaxation (depicted in figure 2.3). In

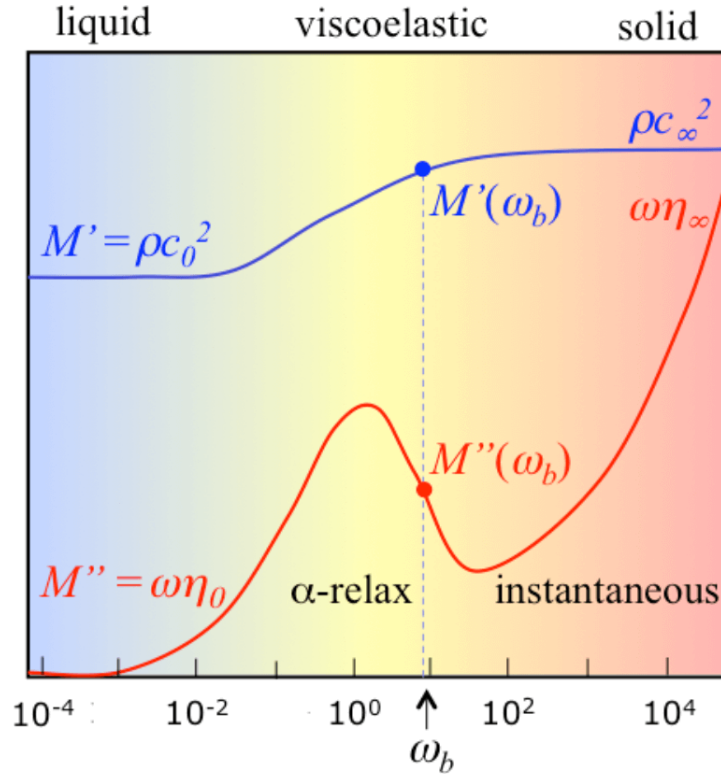


FIGURE 2.3: Frequency dependence of the complex modulus $M = M' + iM''$ in the simplest case where only one relaxation is present. With reference to equation 2.10, $M_0 = \rho c_0^2$ and $M_\infty = \rho c_\infty^2$, where ρ is the density and c the speed of the acoustic wave. ω_b is the frequency at which the complex modulus is probed (Brillouin shift). Figure taken from [23]

this case the frequency dependence can be written as [23]:

$$M(\omega) = M_\infty + \frac{M_0 - M_\infty}{(1 + i\omega\tau)^\beta} + i\omega\eta_\infty \quad (2.10)$$

where τ is the relaxation time and β the stretching parameter. For frequencies much smaller than the relaxation time ($\omega\tau \ll 1$) equation 2.10 becomes $M = M_0 + i\omega\eta_\infty$; M_0 is thus the storage modulus for quasi-static perturbations while the loss modulus increases linearly with the frequency (it vanishes at $\omega = 0$, that is to be expected since the material can respond "immediately" to infinitely slow perturbations). On the contrary, for $\omega\tau \gg 1$ equation 2.10 becomes $M = M_\infty + i\omega\eta_\infty$. Therefore for frequencies that are either much higher or much lower than the relaxation time the storage modulus M' is constant while the loss modulus M'' increases linearly with frequency. If the measurement of the storage modulus M' is performed at a frequency that lies in one of these two regions, a change in M' can be only attributed to a change in M_0 (or M_∞). In the intermediate region instead, a change in M' could also

be caused by a change in the relaxation time τ ; in this case the loss modulus M'' would change in the same or opposite direction depending on how the probe frequency ($\omega_b \sim GHz$) is positioned with respect to τ (see figure 2.3). An experimental demonstration of such behavior was provided by Bailey et al. [24]. They changed the relaxation time in hydrogels by varying their hydration. Indeed they observed the trend described in figure 2.3 (see their figure 2 and 3B). The viscoelastic response of biological samples can be more complex than the simplest case described here and Brillouin measurements are typically performed at a single ω_b (single wavelength of the laser), thus not providing information about the dependence of M with frequency. In light of this, one needs to be careful when interpreting the results of Brillouin measurements.

2.4 Spatial resolution

A very important parameter in defining an imaging technique is the spatial resolution that it can provide. Brillouin microscopy is based on visible light so one obvious limiting factor to the spatial resolution is the diffraction of light. It is well known that the diffraction-limited lateral resolution for an optical system (according to the Rayleigh criterion) is given by [25]

$$Resolution_{xy} = 0.61 \frac{\lambda}{NA} \quad (2.11)$$

while the axial resolution is

$$Resolution_z = 2n \frac{\lambda}{NA^2} \quad (2.12)$$

where NA is the numerical aperture of the objective lens and λ the wavelength of the light and n is the refractive index of the immersion medium.

But the optical resolution is only one side of the coin. As described in section 2.1, Brillouin scattering arises from the interaction of light with thermally-generated spontaneous acoustic waves, which also contribute to defining the relevant spatial scales. Specifically acoustic waves are characterised by their wavelength L_1 and propagation length L_2 , as shown in figure 2.4. From momentum conservation it follows that the wavelength of acoustic waves involved in Brillouin scattering is typically smaller than the optical wavelength⁴. If the mechanical heterogeneities in the sample are smaller than the

⁴From equations 2.1 and 2.2 it follows that $\lambda_p^{-1} \approx 2\lambda_i^{-1} \sin \theta/2$ (λ_i is the wavelength of the incident light and λ_p is the wavelength of the acoustic wave), thus $\lambda_p < \lambda_i$ when $\theta > 60^\circ$

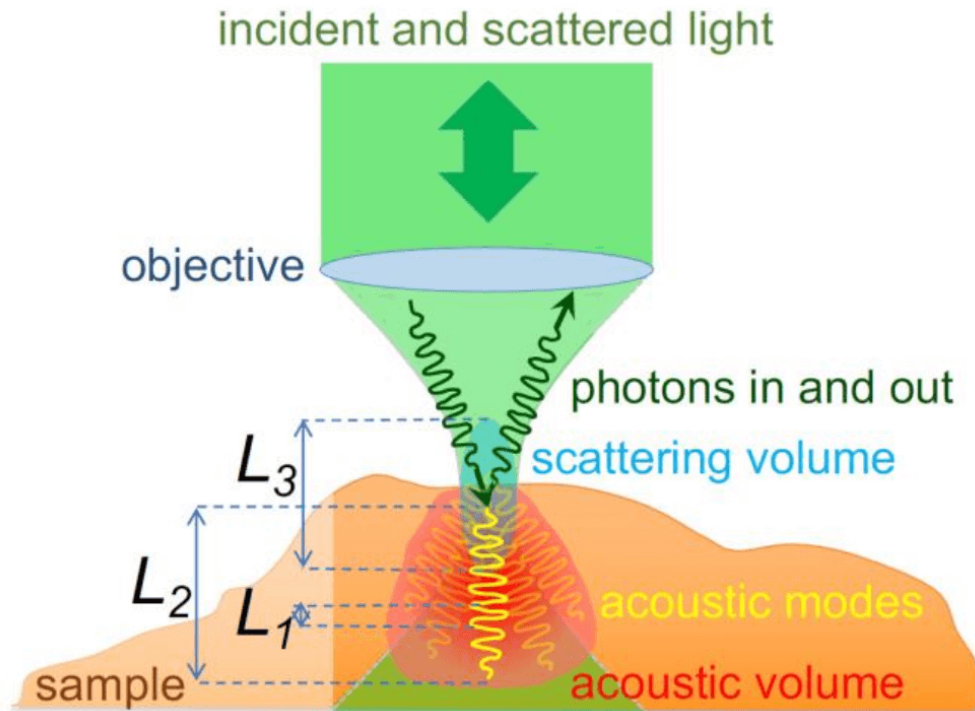


FIGURE 2.4: Graphical representation of the relevant spatial scales in Brillouin scattering. L_1 is the acoustic wavelength, L_2 the acoustic propagation length and L_3 the scattering volume (i.e. the optical PSF). Figure taken from [26]

acoustic wavelength L_1 , an average stiffness is measured because the acoustic waves "see" the material as a continuum. But heterogeneities on this length scale still play a role in the propagation of acoustic waves because they are responsible for dissipative mechanisms that reduce their propagation length L_2 . Dissipation of acoustic waves could also be caused by internal relaxation processes of the material (i.e. at a molecular level). The reduction in L_2 is manifesting in the Brillouin spectrum as an increase in the Brillouin linewidth⁵, that is can thus be used as a readout of L_2 (see section 2.5). Importantly L_2 is affecting the mechanical resolution. In fact, if there is a structure larger than L_1 but smaller than L_2 the acoustic waves generated within the structure can leak outside⁶; therefore, when measuring a region outside (but close to) that particular structure, the acoustic waves generated within the structure can still be detected, effectively "blurring" the image. It is thus

that is almost always the case, since the typically used scattering geometries are epidetection ($\theta = 180^\circ$) or orthogonal ($\theta = 90^\circ$).

⁵In this case it is called homogeneous broadening to distinguish it from the non-homogeneous broadening, that is not caused by absorption of the acoustic waves but rather by the presence of multiple Brillouin peaks in the spectrum that can't be spectrally resolved (more details are in section 2.5).

⁶That is possible only if the acoustic mismatch between the two materials is small, that is often the case in biological matter.

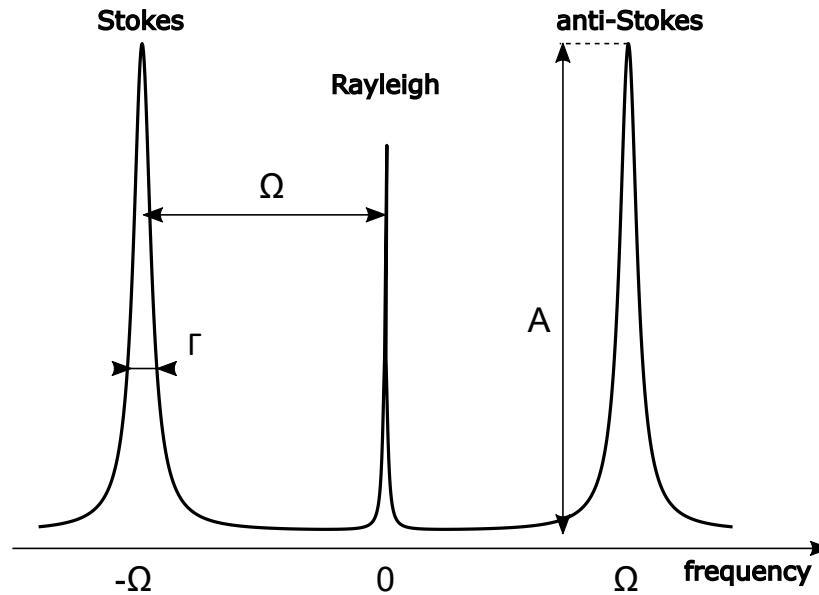


FIGURE 2.5: Schematic of Brillouin spectrum showing the relevant parameter. Ω is the Brillouin shift, Γ the linewidth and A the amplitude.

clear that L_2 set also a lower limit to the spatial resolution, which is sample dependent but could be assumed to be $\lesssim 2\mu\text{m}$ in biological samples. The contribution of L_2 to the resolution produces the counterintuitive effect that increasing the NA of the objective lens might make the spatial resolution worst [26]. This is because higher NA implies broader distribution of k vectors (angles) that can cause an enlargement of the volume probed by the acoustic waves (see "acoustic volume" in figure 2.4). Care should be taken when choosing the NA of the objective lens, ideally using some a priori information on the structure of interest (both in terms of size and acoustic mismatch with the surrounding material).

2.5 Interpretation of Brillouin parameters

In this section, I will describe which information can be derived from the Brillouin spectrum and what caveats one needs to be aware of when interpreting them. Figure 2.5 shows a schematic of a Brillouin spectrum, indicating the three parameters that can be extracted: Brillouin shift Ω , linewidth Γ and amplitude A .

2.5.1 Shift

As introduced in section 2.1, the Brillouin shift Ω is proportional to the speed of the acoustic wave; the speed of the acoustic wave is in turn related to the

stiffness, in terms of longitudinal modulus M (see section 2.2). Combining these results, one finds:

$$M = \frac{\lambda^2}{4} \frac{\rho}{n^2} \Omega^2 \quad (2.13)$$

where λ is the wavelength of the laser in vacuum, ρ and n the mass density and the refractive index within the scattering volume and Ω is the Brillouin shift in epidetection (if the signal is collected in a different geometry, Ω needs to be divided by the sine of half the scattering angle).

One obvious observation is that the conversion from Brillouin shift to longitudinal modulus requires the knowledge of the density and refractive index within the scattering volume; getting a 3D map for both of them is not a trivial task. The two quantities are not completely independent though. They are related by the Lorentz–Lorenz equation

$$\frac{n^2 - 1}{n^2 + 2} = \frac{4\pi}{3} \rho \bar{\alpha} \quad (2.14)$$

where $\bar{\alpha}$ is the average polarizability. But polarizability might differ for different molecules, thus equation 2.14 doesn't allow, in general, to calculate exactly one quantity from the other without additional information [27]. Nevertheless, biological samples are mostly a mixture of water and solid part (different biomolecules, mainly proteins, salts and DNA) and it has been shown that there is a proportionality between refractive index and concentration of biomolecules, with a coefficient that is varying in a narrow range around 0.18 ml/g [28–30]. In turn, the concentration is proportional to density (supplementary information in [30]). The knowledge of the refractive index (that can be measured with optical techniques [31]) is then sufficient to determine the ratio ρ/n^2 . In addition, the variation of refractive index in biological samples is sufficiently small that the ratio ρ/n^2 can be considered constant with an error of few percents [30, 32]. Therefore, typically, the Brillouin shift is reported as a proxy of the longitudinal modulus, without performing the conversion.

An important caveat must be added to the above discussion though: the assumptions are valid for solid components dissolved in water and it breaks for lipids; in fact, lipids have a much lower density and higher refractive index than water, thus the ratio ρ/n^2 is indeed lower than the one in water. To solve this issue, Schlüssler et al. [33] proposed an independent measurement of lipids by fluorescently labeling them and, once their location is known, the appropriate values for density and refractive index can be used.

2.5.2 Linewidth

The linewidth Γ is proportional to the longitudinal viscosity $\eta = \eta_B + 4/3\eta_S$, where η_B is the bulk viscosity and η_S the shear viscosity [1]:

$$\eta = \frac{\lambda^2}{8\pi} \frac{\rho}{n^2} \Gamma \quad (2.15)$$

Here the same considerations about the ratio ρ/n^2 , discussed in the previous paragraph, are relevant.

For the interpretation of linewidth data, it is important to mention that there are two effects that can broaden the linewidth of the Brillouin peak while not being related to viscosity: finite resolution of the spectrometer and broadening due to high NA optics. The first issue could be alleviated by acquiring the spectrum of the laser (which is typically sufficiently narrow to be considered a δ) and use it to deconvolve the Brillouin spectrum. But, if within the scattering volume there are compartments having Brillouin shifts that are distinct but too close to be resolved by the spectrometer, the deconvolution procedure is not able to recover the different components and one measures a larger linewidth. This effect is called inhomogeneous broadening (i.e. arising from different Brillouin peaks that can't be resolved), in contrast with homogeneous broadening that reflects a change in L_2 (as described in section 2.4). The broadening when using high NA can be understood when observing that equation 2.3 depends on the scattering angle: when using high NA optics to focus and collect the light from the sample, the scattering angle is no longer well defined but is rather a distribution⁷. This effect is minimal in the epidetection configuration [34] and, since the broadening can be simulated or measured experimentally, deconvolution can be performed (with the same caveats as in the case of finite resolution of the spectrometer). Importantly though, increasing the NA implies probing different directions in the sample, which might have different mechanical properties in case of anisotropic materials [35, 36]; in that case, a weighted average of the moduli along the different directions is measured.

One last important note is that, when the linewidth is an important parameter to be measured, spectrometers having high resolution should be favored (i.e. based on Fabry-Pérot rather than VIPA, see section 4.2.2) or use different implementations of Brillouin microscopy that intrinsically provide

⁷ $NA = n \sin \theta$ where θ is the semiangle of the cone of focused light, thus for $NA \approx 1$ in air the distribution of angles can span a range as large as 180° .

higher spectral resolution (e.g. stimulated Brillouin scattering microscopy [37]).

2.5.3 Loss tangent

The loss tangent, equivalent to the inverse of the quality factor, is a parameter that in damped mechanical (and electric) oscillators describes how many oscillations take place before the motion is damped. The same definition can be extended to acoustic waves in a material and it is equivalent to the ratio between the imaginary and the real part of the complex modulus (defined in section 2.3). Using equations 2.13 and 2.15

$$\tan \delta = \frac{M''}{M'} = \frac{\Omega \eta}{M} = \frac{\Gamma}{\Omega} \quad (2.16)$$

By definition, the loss tangent is independent of the density and refractive index (because the complex modulus is independent of them) and can be calculated directly from the measured Brillouin spectrum. Therefore it is a useful parameter when it is not possible to measure (or make any assumption about) the density and refractive index [35, 38]. The interpretation of the structural origin of the loss tangent is not straightforward in biological samples, due to their heterogeneity and complex structure. Following the discussion in the supplementary information of Chan, Bevilacqua, and Prevedel [39], the loss tangent can be interpreted as the mean propagation path of acoustic waves, thus it is related to the microstructural composition of the material: the smaller the loss tangent the more "ordered" the microstructure of the material, thus leading to a smaller attenuation of the acoustic waves. The damping of acoustic waves can also be associated with higher levels of bound water in the tissue [40].

On the technical side, the measurement of the loss tangent requires the measurement of the linewidth, so the caveats discussed in the previous paragraph, regarding the "artifacts" introduced by the finite resolution of the spectrometer and the broadening due to high NA optics, are relevant also here.

2.5.4 Amplitude

The amplitude of the Brillouin peaks is related to the cross-section of Brillouin scattering and could in principle provide information about the density within the scattering volume [41]. Unfortunately, in practice, it is also dependent on the absorption from the sample and the two pieces of information are

difficult to decouple. Therefore in general it is not possible to interpret the amplitude of the Brillouin peaks in terms of the physical parameters of the sample but it can still provide contrast, useful to determine the morphology of the sample.

2.6 Difference between "Brillouin" and Young's modulus

Standard tools in mechanobiology (see section 1.2) typically measure Young's modulus E , therefore a recurring question when interpreting the Brillouin data is how the two moduli are related. As I already mentioned in section 2.2, in the linear regime (valid for small perturbations of the sample), the different elastic moduli are fully determined by the stiffness tensor. In particular, when looking at an isotropic material (or a non-isotropic material along a principal axis of symmetry), the knowledge of two elastic moduli is sufficient to determine all the others. The Young's modulus E can be written in terms of the longitudinal modulus M and shear modulus G :

$$E = \frac{G(3M - 4G)}{M - G} \quad (2.17)$$

Unfortunately, the determination of the shear modulus from Brillouin spectra is challenging because it requires the measurements of shear waves, that have a low scattering cross-section and can be determined only in a non-epidetection configuration [18]. One could think that the knowledge of the typical range in which the shear modulus varies in biological samples is sufficient for an approximate conversion between the two moduli. But for liquids $G \approx 0$ and this has two implications in equation 2.17: Young's modulus is much smaller than the longitudinal modulus and small absolute variations of G reflects in large relative variations of E . Additionally, the Brillouin measurements probe the stiffness tensor at the nanosecond timescale while standard measurements are in the millisecond range. As discussed in section 2.3, a difference in timescale also results in a difference in elastic modulus.

In conclusion, the difficulty in determining the complete elastic tensor experimentally in biological samples and the different timescale probed by quasi-static measurements compared to Brillouin microscopy make a general theoretical model that links the two moduli unfeasible. Empirical correlations between the longitudinal modulus and Young's modulus have been

found [42] but they are not general (i.e. the parameters of the model depend on the tissue). Therefore a calibration curve on the tissue under investigation must be performed before attempting a quantitative conversion.

However, the current opinion in the Bio-Brillouin field is that changes in the longitudinal modulus over space and time or between different conditions are already informative because they reflect a change in Young's modulus (even though it can't be quantitatively extracted). Furthermore, the longitudinal modulus itself might actually be a relevant quantity for certain biological processes. Further investigations are needed to tackle the latter question and one of the aims of my PhD was to establish Brillouin microscopy as a tool in mechanobiology to aid in this process.

Chapter 3

Current applications of Brillouin microscopy in biology

Due to its advantages, mentioned in section 1.3, Brillouin microscopy has been applied to many fields in biology and medicine both for fundamental research and as a diagnostic tool. Several reviews [1, 43–47] have already summarised the applications that Brillouin microscopy has found in biology in the last decades but they often focus on specific topics or only briefly describe the main findings. In this chapter I will try to give a comprehensive (to the best of my knowledge) list of applications, citing the relevant literature and the most significant findings. I will focus on the applications in cell biology, developmental biology and medicine, while leaving out the studies on biological materials (e.g. collagen and muscular fibers, biofilms, bones, etc.). The latter form a consistent part of the literature but falls at the intersection between material science and biology, outside the scope of this thesis.

3.1 Cell biology

3.1.1 Animal cells

Nanobiomechanics is an emerging field that studies the mechanical properties of biomaterials at the nanometer scale. It has important implications in disease diagnosis and treatment, since changes in structural and mechanical properties of cells have been suggested to be the cause of several diseases [5]. Brillouin microscopy can measure mechanical properties in situ at a subcellular scale and it can thus provide valuable information in that context. For example, it has been hypothesized that phase transition inside the cytoplasm, due to mutated proteins, can be the mechanism behind the neurodegenerative disease amyotrophic lateral sclerosis (ALS). Indeed, when Antonacci et al. [48] looked at stress granules containing ALS mutant FUS in comparison to

"non-mutant" stress granules in HeLa cells, they found a higher Brillouin shift and width in the former, suggesting a liquid to solid transition. Such transition was already observed *in vitro* but the Brillouin data suggests that it happens also in cells.

From a more fundamental perspective, Brillouin microscopy can be employed to understand how cells regulate their mechanical properties via their cytoskeletal components. This can be done by comparing control cells with cells treated with drugs that have a known effect on the cytoskeleton or by changing the environment surrounding the cells (e.g. osmolarity, substrate stiffness). Such an approach has the added value of allowing the "validation" of Brillouin microscopy: global mechanical properties of isolated cells can be measured with standard techniques (e.g. AFM, see section 1.2), it is thus possible to establish a correlation between the longitudinal (Brillouin) modulus at high frequency and Young's modulus at low frequency. The first of such validations in cells was done by Scarcelli et al. [49] where they observed an increase of both longitudinal modulus (M) and Young's modulus (E) of cells upon the increase of sucrose concentration in the medium. They found that the two moduli can be linked via the relationship $\log(M) = a \log(E) + b$ where a and b are coefficients that depend on the material¹. To further validate the relevance of Brillouin shift as a proxy for cellular mechanics, they also reported an increase in the Brillouin shift of cells when growing them on stiffer substrates, consistently with previous studies employing AFM. Finally, they showed that Brillouin microscopy is sensitive to alterations of the cytoskeleton: when NIH 3T3 cells were treated with cytochalasin D, an inhibitor of actin polymerization, their average Brillouin shift went down; this result was complemented with the observation of an increasing Brillouin shift during actin polymerization and branching in reconstituted actin gels *in vitro*.

After validating Brillouin microscopy, one can take advantage of its high spatial resolution and look at subcellular components. Antonacci and Braakman [50] reported for the first time a high-resolution Brillouin map of porcine aortic endothelial cells and observed distinct mechanical properties of the nuclear envelope and nucleoli. The improved resolution allowed them to determine that the treatment with Latrunculin A, a drug that prevents actin polymerization, decreases the Brillouin shift of the cytoplasm but not of the

¹An example of the variability of the coefficients a and b is given by Scarcelli, Kim, and Yun [42], who found that even the same tissue (crystalline lens) from two different animals (pig and cow) has different coefficients ($a = 0.093$ and $b = 9.29$ in the porcine lens while $a = 0.034$ and $b = 9.50$ in the bovine lens).

nucleoli, showing that Brillouin microscopy is capable of detecting changes in mechanical properties at a subcellular level. Similarly, Coppola et al. [51] investigated the hypothesis that actin stress fibers are responsible for the increased Brillouin shift on stiffer substrates. Although they could not directly observe the stress fibers in the Brillouin images², they could distinguish 3 populations, based on the Brillouin shift, only one of which was significantly changing upon changing the stiffness of the substrate. They confirmed that the average Brillouin shift of this population is close to the average of pixels containing stress fibers, identified by correlative fluorescence imaging.

The possibility of looking at subcellular structures opens the doors to studying the mechanical properties of the nucleus, that is known to play an important role in mechanosensing and mechanotransduction. Zhang et al. [52] extensively characterized it, also with the aid of their previously developed microfluidic device [53], by performing perturbations that affect the mechanics of the nucleus (Lamin A/C Knockdown, chromatin decondensation by trichostatin A) or of the cytoskeleton (depolymerization of actin with cytochalasin D and microtubules with nocodazole). Interestingly in both cases they observed a significant change in the mechanical properties of the nucleus and they developed a 3D chemomechanical mathematical model, to explain how mechanical signals are transmitted from the extracellular environment to the nucleus and how the perturbations on the cytoskeleton are thus affecting the mechanical properties of the nucleus. Their model correctly predicts the experimental observations and it thus highlights the importance of measuring the nucleus in the intact cell, without detaching it from the cytoskeletal components.

In addition to fluorescently labeling a specific constituent of the cell, the combination of Brillouin with Raman spectroscopy can provide mechanical information with chemical specificity in a label-free manner [54, 55].

3.1.2 Plant cells

Mechanical properties, especially of the cell wall, have a fundamental role in providing structure and strength to the plant and, at the same time, controlling plants' growth and organ formation [56]. While the mechanical properties of cell walls in epidermal tissues have been investigated, *in vivo*, using "standard" techniques (e.g. AFM, see section 1.2), the sub-epidermal tissues are inaccessible, thus more challenging to measure. Brillouin microscopy,

²Due to their small size, actin stress fibers can not support bulk acoustic modes.

instead, gives access to deeper layers with high spatial resolution and can also inform about the mechanical anisotropy. The possibility of assessing the non-uniformity and anisotropy is very valuable since it has been shown that they are a prerequisite to driving directional growth. Elsayad et al. [57] observed that the extra-cellular matrix (ECM) along the growth axis of *Arabidopsis* hypocotyls is stiffer than the one perpendicular to it, suggesting that the higher stiffness prevents transverse swelling and promotes elongation of the hypocotyl. When looking at double-mutants phytochrome A and B, in which the growth of the hypocotyl is not arrested in response to light, they observed softer ECM. This finding seems to confirm that the stiffness of the ECM has a role in hypocotyl growth. Along the same line Altartouri et al. [58] hypothesized that heterogeneity of mechanical properties is the first step in the formation of pavement cells in *Arabidopsis*, which are lobe-shaped cells: first, the prospective neck region becomes stiffer and that drives the formation of the lobe. Indeed when acquiring Brillouin images of pavement cells they observed a significant difference between the neck and lobe region. Interestingly, they could also link the crystalline of cellulose with the stiffness of the cell wall. They imaged *amy 1* mutants, having the same amount of cellulose but lower crystallinity and showing impaired lobe expansion in the later development as a phenotype. When looking at Brillouin images, they observed an overall softer cell wall and a smaller difference in stiffness between the neck and lobe region: that could explain why the lobes are formed but fail to develop properly. Another investigation on the role of mechanical properties in root growth was reported by [56]. They observed that overexpression of expansin correlates with stiffer regions in the root tip and impairs root growth. The increase in stiffness is opposite to what one would expect since expansin is known to loosen the cell wall. Although the authors say that the underlying molecular/biophysical mechanism of this counterintuitive finding remains to be clarified, they proposed that the overexpression of expansin might alter the endogenous equilibrium of mechanical forces, thus producing an avalanche effect leading to the counterintuitive increase in cell wall stiffness. Altogether these findings show that the spatial distribution and anisotropy of mechanical properties are essential for the proper development of the plants and are thus tightly regulated. Laura et al. [59] investigated the role of the kinase *Theseus1* in regulating the stiffness of cell wall, in response to changes in turgor pressure and cell wall damage induced by drugs. Brillouin microscopy allowed them to measure the mechanical properties at the center of the root, without dissecting it, which could alter

the mechanical properties and release the turgor pressure.

Lastly, plant fibers have a high strength-to-weight ratio, are renewable and provide good thermal insulation, which makes them an interesting biomaterial. Brillouin microscopy can be used to rapidly characterize their mechanical properties in different directions [35], or even to determine the complete elastic tensor [60].

3.2 Developmental biology

Despite the physical forces and mechanical properties of tissues playing a fundamental role in the development and final shape of an organism, they are not explored as extensively as the genetic mechanisms and chemical signalling [4]. The possibility of measuring internal tissues *in vivo* over time makes Brillouin microscopy a valuable tool in developmental biology. In fact, *ex vivo* measurement of mechanical properties in multicellular organisms could lead to wrong conclusions, even when comparing different tissues within the same sample: Schlüßler et al. [30] observed that, while *in vivo* imaging of zebrafish showed no mechanical difference between muscle and spinal cord tissue, *ex vivo* sections showed a difference when probed with both AFM and Brillouin. Obviously, in addition to measuring the sample in physiological conditions, *in vivo* measurements allow to follow the development of a single organism instead of taking snapshots at different times in different organisms, thus reducing the biological variability and the number of replicates necessary to have a statistically significant trend. For example Schlüßler et al. [30] imaged the injured spinal cord of 6 zebrafish at 3 days post fertilisation (dpf) for 2 days after the injury: they observed a decrease in Brillouin shift immediately after the injury followed by a gradual increase, showing that mechanical properties are indeed involved in the regenerative process. Similarly, when looking at axolotl (which is well known for its regenerative capabilities), Riquelme-Guzmán et al. [61] found that the Brillouin shift of the cartilage in the digit is decreased 15 days post-amputation (dpa) and increased again afterward. Interestingly, at 30 dpa the arrangement of cells indicates a mature-like morphology but the Brillouin shift was not back to the value before amputation, indicating that the regeneration process was not completed despite its morphology would indicate otherwise. Additionally, the increase of Brillouin shift over time was observed also during the normal development of the digits, showing a similarity between the development and regenerative processes.

Several studies looked at the interplay between mechanical properties and morphogenetic events or the final structure of tissues in different model organisms. I will now introduce the relevant literature and main findings, grouping them by model organism.

In mouse Zhang et al. [62] looked at the process of neural tube closure and they observed stiffer neural folds in closed neural tubes compared to the open. At the end of the process, a gradient of mechanical properties along the dorsal-ventral direction was observed, that the authors hypothesized could be essential in facilitating the closure of the neural tube. Chan, Bevilacqua, and Prevedel [39] studied intact ovaries extracted from mice at different ages and found that different regions within the ovary show different mechanical properties, suggesting that they play a role in follicle development (see section 4.3.2 for more details).

In zebrafish Bevilacqua et al. [36] found that the thin layer of extracellular matrix (ECM) surrounding the notochord has distinctly high stiffness, suggesting its essential role in withstanding the high pressure exerted by the vacuoles and thus achieving the almost perfectly cylindrical shape (see section 4.3.1). Amini et al. [63] looked at the formation of the retina, specifically how horizontal cells can migrate in the highly crowded environment of the retina to reach their final position inner nuclear layer. They observed an amoeboid-like behavior, that doesn't seem to be directed by a mechanical gradient but rather to be happening in a mechanical uniform tissue that permits the migration.

In *C. elegans* Geisler et al. [64] looked at the role of intermediate filaments (IF) in the morphogenesis and function of the endotube in the intestine. Although the layer of IF surrounding the endotube is too thin to be resolved by Brillouin microscopy (~ 60 nm), its localization by fluorescence microscopy shows that it is positioned between the stiff brush border and soft cytoplasm. Since IFs are known to be very flexible, they could serve as a mechanical buffer between the two different regions and accommodate the deformations and movement of the lumen during food intake. Remer et al. [37] imaged a single plane from the whole nematode at L2, L3, and L4 stages and found that the pharynx was stiffer and more viscous than the surrounding tissue and its viscoelasticity was constant during development, suggesting that it is established early in development, due to its essential function in feeding.

Bevilacqua et al. [65] studied the process of ventral furrow formation (VFF) during gastrulation in *Drosophila*. During VVF cells on the ventral side exhibit a drastic and rapid change of shape and eventually invaginate. It is

thus believed (and indirectly tested by laser ablation and simulations) that their mechanical properties play a fundamental role in the process. Indeed they exhibit a transient increase in Brillouin shift when the invagination starts (see section 5.5 for more details).

Finally, Pukhlyakova et al. [66] looked at gastrulation in *Nematostella vectensis*, specifically at the interplay between gene expression and mechanics. They observed that Brachyury, a protein that is essential for mesoderm formation, is normally expressed in the blastopore region but its expression can be induced by physical forces via mechanotransduction. By using Brillouin microscopy, they found that the blastopore lip cells are stiffer than the surrounding tissue and this suggests that their mechanical properties are involved in the force generation that facilitates the expression of Brachyury.

3.3 Medical applications

3.3.1 Disease mechanism and diagnosis

Alteration of mechanical properties is a distinctive feature of several diseases [6]. It is therefore not surprising that Brillouin microscopy has been proposed, by several studies, for both diagnosis and understanding of the mechanism leading to the disease.

Palombo et al. [40] showed the potential of combined Brillouin, Raman microspectroscopy (and, in a later study [67], Fourier Transform IR imaging) for the chemical and mechanical characterization of tissue from patients affected by Barrett's oesophagus. This allowed them to determine the link between the chemical composition and mechanical properties of the tissue, in particular the role of bound water (as measured by Raman) in determining the mechanical properties of the extra-cellular matrix. Their study is the first demonstration of imaging diseased tissue with Brillouin microscopy, as a potential tool for diagnosis.

Steelman et al. [68] proposed the use of Brillouin microscopy for the diagnosis of bacterial meningitis. In fact the total protein content in the cerebrospinal fluid (CSF) is increased during the disease and they found that the Brillouin microscope can reliably measure the difference. In contrast to other existing diagnostic tools, Brillouin microscopy is fast (importantly, swift treatment is essential to reduce the mortality rate) and non-destructive for the CSF sample (that could be thus used for other tests).

Cardiovascular diseases are the leading cause of death in the world, accounting for about 18 million deaths each year (32% of the total) [69]. Several of them are caused by the rupture of atherosclerotic plaques, which is recognized to be caused by mechanical stress that accumulates at the interface between the stiff cap and less rigid core of the plaque. Therefore a local measurement of plaque stiffness *in vivo* would improve the risk assessment of plaque rupture. Antonacci et al. [70] performed Brillouin imaging on thin cap fibroatheromas and could distinguish the lipid-rich heterogeneous tissue of the plaque from the healthy, collagen-rich tissue. They speculate that future *in vivo* measurements of both vessel geometry and stiffness could provide the framework to predict the risk of plaque rupture. Jannasch et al. [71] demonstrated that Brillouin microscopy can be used to study the aortic valve, whose mechanical properties are important for its function. Villalba-Orero et al. [72] looked at myocardium and detected different mechanical properties between the left and right ventricles in mice. Additionally, they could measure differences in Brillouin shift, following infarction and aortic stenosis, compared to control hearts. Interestingly, although they found a correlation between Brillouin modulus and ventricular wall motion and deformation (as measured by speckle tracking echocardiography), the correlation was lost in diseased heart, suggesting an important role of the mechanical properties for the proper contraction of the myocardium.

Obesity, that is becoming a global epidemic, consists of an increased ratio of lipid tissue to the total body mass and, consequently, a remodeling of adipose tissue. Despite the mechanical properties of the adipose tissue being important for its function both for the protection against mechanical stress and storage of lipids, their characterization is limited. Troyanova-Wood et al. [73] used Brillouin microscopy to study both white and brown adipose tissue in control and diet-induced obese mice. They found that the stiffness of both adipose tissues in obese mice is increased. Furthermore, with the aid of Raman spectroscopy, they showed that the growth of adipose tissue in high-fat diet mice is mainly driven by an increase in lipids and less in proteins.

Mattana et al. [74] looked at amyloid plaques in *ex vivo tissue* from mouse brain. Amyloid plaques are considered to be the main cause in the pathogenesis of Alzheimer's disease, the most common form of dementia. They found that plaques are formed by a rigid core surrounded by a softer lipid-rich ring. A later analysis [75] showed that a non-negative matrix factorization of the Brillouin spectra can distinguish 4 regions (i.e. the plaque core, the region around the core, the lipid ring and the normal ECM) in a non-supervised

way. Altogether these results can have implications for both the diagnosis of Alzheimer's disease and the screening of novel drugs.

Lainović et al. [76] studied the dentin and found that healthy dentin can be very clearly distinguished from the diseased dentin by looking at their Brillouin shift. Furthermore, when looking at the interface between the sound dentin and the tooth-filling resin, Brillouin microscopy revealed the presence of a hybrid layer where both the dentin and resin are present. This information could be used in clinical settings to guide the procedure of caries removal and tooth filling.

At the onset of osteoarthritis, there is a depletion of proteoglycan in the cartilage, that in turns leads to increased tissue hydration and permeability. Wu et al. [77] explored whether Brillouin microscopy is sensitive to these changes and could thus be used for the early diagnosis and monitoring of osteoarthritis. To model the degradation of the cartilage during osteoarthritis they exposed porcine articular cartilage to enzymatic digestion and measured the Brillouin shift of the samples before and after the treatment. They found a reduced Brillouin shift after treatment that they interpreted as a change in the hydration of the extra-cellular matrix.

One of the key advancements that are needed to translate many of these findings into clinical settings is the possibility of measuring the tissues in situ via an endoscope. Here the main challenge is that, when using a glass optical fiber to deliver the light, the Brillouin signal generated by the fiber itself is much more intense than the one collected from the sample, thus creating a large background that interferes with the measurement. Kabakova et al. [78] proposed the use of two separate fibers for illumination and detection, showing virtually no background but low efficiency due to the poor overlap between the spatial mode of illumination and detection. A few years later the same group proposed the use of hollow core fibers for Brillouin endoscopy [79]. Due to their peculiar structure, hollow core fibers can guide the light without needing a glass core, thus generating almost no background signal. They imaged a tissue-mimicking phantom, demonstrating the imaging capabilities of the endoscope.

Finally, Brillouin microscopy has been proposed as a method to perform label-free histology, without the need of tissue preparation and staining, that is a time-consuming step necessary in conventional histologic analysis [80]. Ryu et al. [80] showed that the different tissues within cartilage, skin and brain could be clearly resolved and they speculated that the contrast mechanism is due to both differences in water content and mechanical properties

of the tissue. They reported a maximum penetration depth on the tissue of about 100 μm that could be in principle increased by optically clearing the tissue. In fact, Riobóo, Desco, and Gómez-Gavero [81] showed that the clearing procedure doesn't affect the Brillouin shift, while significantly improving the reliability of the measurements.

3.3.1.1 Ophthalmology

Ophthalmology deserves a separate section due to the vast literature that investigated the eye using Brillouin microscopy, both for a fundamental understanding of its structure and for disease diagnosis and treatment, leading to successful ongoing clinical trials. Regarding the first point, already in 1980 Vaughan and Randall [82] recognized the potential of Brillouin spectroscopy to study the biophysics of the eye at a molecular scale. They measured, for the first time, the longitudinal modulus and density of dissected corneas, capsules and lenses of the eye from 4 classes of vertebrates (Mammalia, Aves, Pisces and Amphibia); the acquisition speed was limited by the use of a triple-pass Fabry-Perot, limiting the 3D capabilities. It was only with the introduction of VIPA-based spectrometers in 2007 that 3D imaging of the intact eye *post mortem* was made possible [83] and 5 years later the first *in vivo* imaging on the human eye was reported [84]. Several studies have looked at the Brillouin spatial map from mouse, bovine, pig and human eyes [32, 42, 84–86], showing a different mechanical signature for the different regions of the eye (cornea, aqueous humor and crystalline lens) and also a gradient along the depth of cornea and lens. All the studies mentioned so far have focused on the spatial heterogeneity in mechanical properties and not on their anisotropy. But the cornea is known to be formed by a network of fibers, that provides mechanical strength, and is aligned in a plane parallel to the corneal surface, thus an asymmetry of the mechanical properties can be expected. Indeed, recent studies found that the measured Brillouin shift depends on the angle of the optical axis with respect to the cornea surface and individual fibers can be clearly discerned by having the optical axis parallel to the surface of the cornea. [87, 88]

For ocular disease diagnosis and treatment, Brillouin microscopy has found several applications in the last decade [89]. Stiffening of the cornea was hypothesized to be one of the causes of the decline of accommodation with age that leads to presbyopia. Scarcelli, Kim, and Yun [42] found in mice, *in vivo*, that there is a substantial stiffening with age. On the contrary, human studies

ex vivo [85] and *in vivo* [90] found no significant change of mechanical properties with age, suggesting that stiffening of the lens is not the main cause of presbyopia.

Keratoconus is a disease that causes vision problems due to the change in the shape of the cornea. Scarcelli et al. [91] measured discarded human corneal tissue after surgery and observed a lower Brillouin shift in the region affected by keratoconus. This observation was later confirmed *in vivo* [92, 93] and strong spatial variations between healthy and keratoconus tissue were observed as well. They also found a significant stiffening of the healthy corneal tissue with age. Shao et al. [94] tested the use of Brillouin microscopy as a diagnostic tool for keratoconus showing better performances than standard techniques for mild cases.

Corneal collagen crosslinking (CXL) is a procedure used to prevent corneal ectasia. Scarcelli, Pineda, and Yun [32] showed that Brillouin microscopy is sensitive to the changes in mechanical properties induced by CXL. Later studies investigated the outcome of CXL when changing the experimental parameters [95], using two photons (that gives better control on the crosslinked area) [96], reducing the exposure time to UV radiation by keeping the same energy [97] or using different crosslinking protocols [98, 99]. Altogether these studies highlight how Brillouin microscopy can be used to improve the CXL protocols or monitor their results.

One important consideration, when interpreting the Brillouin maps, is that the hydration of the cornea will affect the measured Brillouin shift [100]. Shao et al. [101] developed a theoretical model to study this effect and they validated it on *ex vivo* porcine corneas and *in vivo* healthy human volunteers, looking at diurnal changes of hydration; they concluded that corneas from patients should be imaged at least 2 hours after waking up, to mitigate the effect of hydration. The increase in hydration was also hypothesized to be the cause of the transient decrease of Brillouin shift after LASIK surgery [102].

From a more fundamental perspective, the possibility of extracting tissue from the cornea or the lens made it possible to look at the correlation between longitudinal modulus measured by Brillouin and Young's modulus measured by other techniques [32, 42, 103]: while the absolute values of the two moduli are very different (due to their different definition and timescales, see section 2.6) they show a very strong correlation.

3.3.2 Tumor biology

Tumor growth and metastasis is intrinsically a 3D process, thus Brillouin microscopy is a powerful tool to measure the mechanical properties of both tumor tissue and its surrounding environment, in a spatially resolved fashion, and how they correlate with tumor aggressiveness, migration or response to drugs.

Margueritat et al. [38] measured, for the first time, a spatially resolved map of mechanical properties from deep tumoral tissue, showing heterogeneity of mechanical properties in tumor spheroid from colorectal carcinoma cells. Moreover, they observed a change in both stiffness and viscosity, with different spatial and temporal dynamics, upon treatment with 5-fluorouracil, a drug commonly used for treating colorectal cancer. Their results showed the applicability of Brillouin microscopy to study the response of tumors to drug treatment in a spatially resolved fashion. Similarly, Conrad et al. [104] observed a decrease in stiffness of ovarian cancer nodules upon treatment with carboplatin, a drug commonly used in the treatment of ovarian cancer. They also measured the nodules using Brillouin microscopy, AFM and MicroSquisher and observed a similar trend of the respective elastic moduli under different osmolarity conditions for all of them, validating Brillouin microscopy against other established mechanical measurements. Mahajan et al. [105] observed that MCF-7 tumor spheroids adapt their growth and their mechanical properties to the stiffness and degradability of the embedding hydrogel. They hypothesized that the difference in mechanical properties of the spheroids is due to their response to compressive stress. Moreover, they embedded invasive cancer cell lines in degradable hydrogels observing that invasiveness correlates with lower Brillouin shift of the cells. Nikolić, Scarcelli, and Tanner [106] also investigated the influence of the substrate on the mechanical properties of tumor cells. They observed no difference in the mechanical properties of cells in 2D vs. 3D but a dependence on the stiffness of the substrate, suggesting that a robust use of mechanical properties as a proxy for cell state needs to take into account the surrounding environment and be integrated with additional information (e.g. morphology). They also observed a lower variance of the Brillouin shift of tumor spheroids compared to single cells, suggesting a cooperative behavior of the cells during the formation of the spheroid. Roberts et al. [107] focused on the role of stiffness in tumor invasiveness; they used metastatic tumor cells to study transendothelial migration (TEM) through an artificial blood vessel, mimicked by human umbilical vein endothelial cells seeded on collagen.

Their focus was on the mechanical properties of the nucleus, which needs to deform during TEM, since the tumor cells are squeezing through pores smaller than the initial size of the nucleus and it is thus thought to be a limiting factor in extravasation. They found that during the extravasation process the tumor cells, and prominently their nuclei, soften and maintain these mechanical properties for at least 24h. Their observations suggest that tumor metastasis is facilitated by the softening of the cancer cells.

Brillouin microscopy was also applied to differentiate healthy tissue from normal and regressing melanoma in histological samples collected from Sinclair miniature swine. Troyanova-Wood, Meng, and Yakovlev [108] reported that normal melanoma has a higher Brillouin shift than regressing melanoma, with the healthy tissue being the softest.

Chapter 4

Confocal Brillouin microscope

4.1 Motivation

As described in chapter 1, Brillouin microscopy is a powerful tool to study the role of mechanical properties in biological systems. Therefore one of the aims of my PhD was to improve a confocal Brillouin microscope, whose spectrometer was built by Dmitry Richter during his master thesis, to allow biologists to use a state-of-the-art Brillouin microscope on their own with minimal training.

To achieve this goal I worked both on the software and on the hardware side. Regarding the software, I wrote a LabVIEW program that makes the acquisition and data processing more intuitive and automated (see section 4.2.4). On the hardware side, I exchanged the microscope body previously in use with a motorized version, essential to automatize the acquisition and I re-designed and re-built the optical path for illumination and detection. I also designed and built a concurrent confocal fluorescence excitation and detection (see section 4.2.3); the possibility of co-registering a fluorescence image to the Brillouin image allows for the correlation of the mechanical properties with a cell constituent of interest.

The big goal was to establish Brillouin microscopy by applying it to many different samples (see section 4.3) and exploring its potential in biology. I did this by discussing the potential use of Brillouin microscopy with collaborators, helping them with acquiring Brillouin microscopy data, and interpreting the results.

4.2 Setup description and characterisation

Conceptually a confocal Brillouin microscope is the same as a confocal fluorescence microscope where a high resolution spectrometer is used instead of

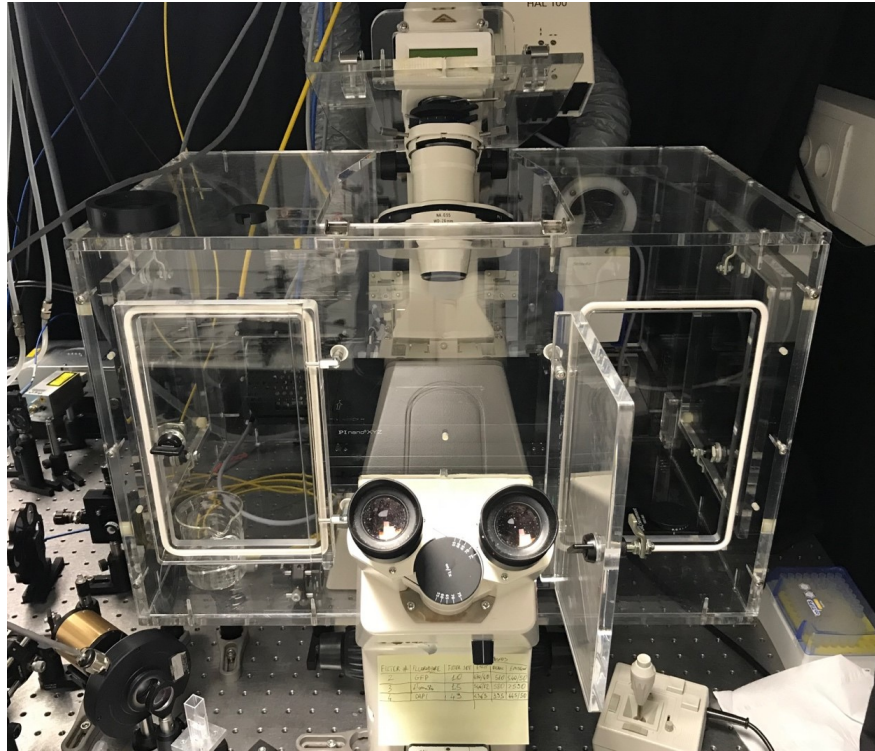


FIGURE 4.1: Picture of the incubator for environmental control.

a photomultiplier tube (PMT) to resolve the Brillouin spectrum. An objective lens focuses the light on a point in the sample and the point is scanned to reconstruct the image.

The main building blocks are the microscope body, the optical components that deliver and collect the light and the Brillouin spectrometer (see dashed boxes in figure 4.2). Additionally, a confocal fluorescence microscope is implemented (more details on the implementation in section 4.2.3) that, as mentioned in section 4.1, is important when looking at how specific cell components are related to mechanical properties.

As microscope body I used a Zeiss Axiovert 200M, that is motorized and can be controlled from the computer via serial commands; that makes it possible to select the optical path inside the microscope in an automated fashion, via a self-written LabVIEW software. The microscope was also equipped, by the EMBL mechanical and electronic workshops, with an incubator (fig. 4.1) that can control the temperature, the CO_2 and O_2 , essential for life imaging of some biological samples. A motorized translational stage is used to position the sample in the FOV; a 3D piezo stage (P-545.3R8H, Physik Instrumente), having a maximum travel range of $200\mu\text{m}$ and a resolution of up to 1nm , is mounted on top of the motorized stage and it is used for precise movements of the sample during image acquisition. Contrary to fluorescence

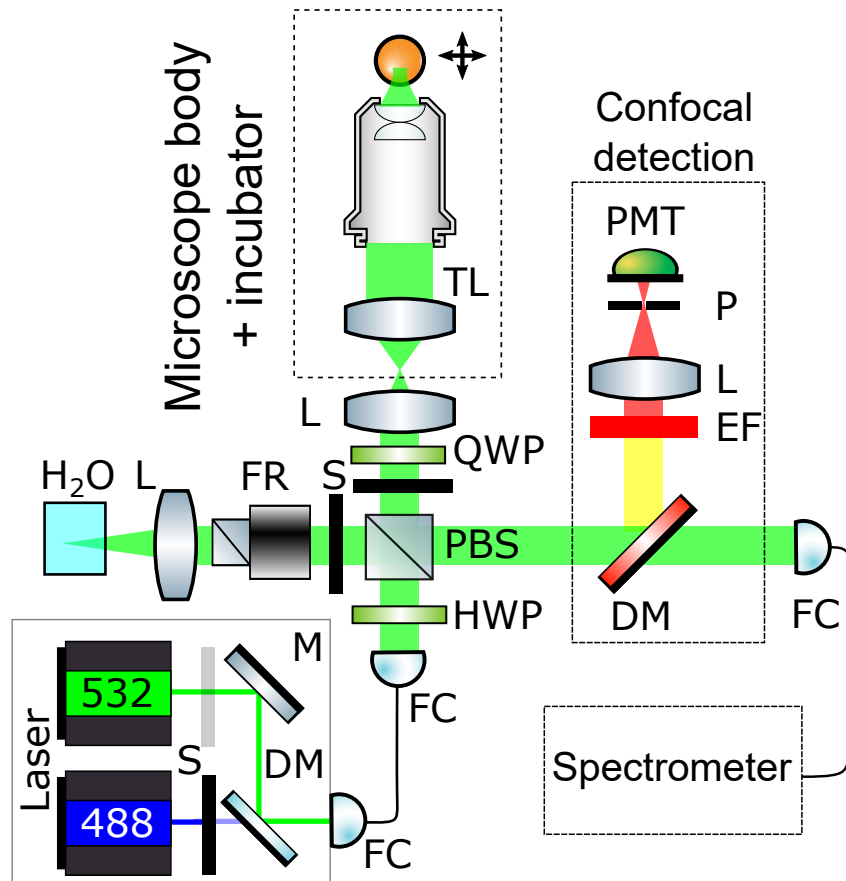


FIGURE 4.2: Schematic of the optical setup for the confocal Brillouin setup. L = lens, TL = tube lens, PMT = photomultiplier, P = pinhole, EF = emission filter, DM = dichroic mirror, FC = fiber coupler/collimator, QWP = quarter waveplate, HWP = half waveplate, PBS = polarizing beam splitter, S = shutter, FR = Faraday rotator, CL = cylindrical lens.

microscopy where the standard approach is to scan the focus spot (with galvanometric mirrors) while leaving the sample still, we keep the focus spot fixed and move the sample in 3D to reconstruct the image. The approach of scanning the beam has the advantage of being faster and avoiding possible drifts of the sample (due to acceleration during movement) but requires higher complexity in the optical design; in Brillouin microscopy, the acquisition speed is limited by the weak signal (see section 4.4), therefore there is no speed advantage in using a beam scanning approach, thus sample scanning is commonly used.

4.2.1 Brillouin illumination and detection

The optics in figure 4.2 that are not enclosed in a dashed box have the aim of delivering the laser light to the sample and redirecting the Brillouin signal to the spectrometer. Before describing how this is achieved, there are

some important requirements for the laser to be discussed. The wavelength of the laser can be anywhere in the visible or near IR range; shorter wavelengths will have a higher Brillouin signal (as the cross-section is proportional to λ^{-4}) but are more prone to inducing photodamage in the sample [109]. The linewidth has to be narrow ($\ll 0.5\text{GHz}$ that is the typical resolution of a VIPA based spectrometer) with high spectral purity ($>60\text{dB}$) to avoid the shoulders in the spectrum to be stronger than the Brillouin signal; the wavelength needs to be stable ($\lesssim 1\text{GHz}$ drift) during the duration of imaging. These requirements limit the commercially available choices and, at the time the setup was built, one of the few lasers that met the requirements was the Torus 532 from Laser quantum.

Going back to the design of the optical path (figure 4.2), I coupled the laser in a single mode polarisation-maintaining (PM) optical fiber. The use of a single mode fiber allows to spatial-filter the laser, producing a very clean Gaussian profile at the output, and to have the 488nm laser, used for fluorescence excitation (see section 4.2.3), co-aligned with the 532nm laser after the fiber. An achromatic fiber collimator (LPC-04-405/640-3/125-P-1.8-12AC-40, OZ Optics) produces a linearly polarised beam with a diameter of 1.8mm ($1/e^2$). A half waveplate, mounted on a rotational mount, allows selecting the polarisation direction, that in turn determines the ratio of light transmitted and reflected by the polarizing beam splitter (PBS). The reflected light is focused on a cuvette filled with distilled water, used as a calibration material (details in section 4.2.2): the Brillouin shift for water at 532nm excitation at room temperature (7.46GHz) is taken from Scarcelli and Yun [83]. The Brillouin signal generated by the water has the same polarisation as the incident light, when probing longitudinal acoustic waves (see section 2.1). Therefore a Faraday rotator can be used to fully redirect the signal to a single "port" of the PBS, similarly to an optical circulator: a Faraday rotator rotates the polarisation by 45° in a non-reciprocal fashion, meaning that, when the Brillouin signal travels in the opposite direction through the rotator, the polarisation is further rotated by 45° in the same direction, adding up to an overall rotation of 90° . Since the polarisation is now orthogonal to the one originally reflected by the PBS, the signal will be fully transmitted by the PBS and will reach the fiber coupler. Similarly, on the optical path that goes to the sample, a quarter waveplate achieves the same effect: the axis of the waveplate is oriented at 45° with respect to the incident linear polarisation, effectively behaving as a half waveplate on double pass, that rotates the polarisation by

90°. The only difference is that the polarisation on the sample will be circular. The use of a quarter waveplate instead of a Faraday rotator is motivated by the need of having a broadband transmission over the visible range to detect fluorescence signal. After the quarter waveplate, an achromatic lens ($f=30\text{mm}$, AC254-030-A-ML, Thorlabs) forms a 4-f system with the tube lens inside the microscope ($f=165\text{mm}$), that magnifies the beam by a factor of 5.5, to fill the back aperture of the objective. Two shutters after the PBS allow for selecting either the reference or the sample path: during acquisition, the spectrum from the water in the calibration arm is acquired every 50 points in the sample to correct for drifts in the laser.

4.2.1.1 Spatial resolution

As described in section 2.4 the spatial resolution of Brillouin microscopy depends both on the optical PSF and on the attenuation length of the phonon, that is sample dependent. Therefore one needs to be careful when reporting the spatial resolution of a Brillouin microscope. One possible way of quantifying it is to look at the intensity of the Brillouin signal while transitioning between two materials that have a very high mismatch of the acoustic impedance [26]; in that case, the Brillouin resolution tends to match the optical resolution. I used the transition between immersion oil and a glass coverslip to quantify the step response: from an optical standpoint the coverslip has an optical-quality surface so the transition is very sharp and the oil is index-matched with the glass, reducing the reflection and refraction at the interface; from a mechanical standpoint the acoustic speed in glass is about 4-folds higher than the one in oil. By scanning the sample both perpendicularly (x) and along (z) the optical axis of the objective and calculating the amplitude of the Brillouin signal from the oil, I obtained the plots in figure 4.3. I measured a 1.4 and 1.0 oil immersion objective, commonly used in the setup. I fitted the raw data with an *erf* function, that is the integral of a Gaussian, and calculated the FWHM from the fit. By repeating the same measurement multiple times I obtained the following table 4.1. Note that the lower value of the effective NA compared to the nominal one could be both due to underfilling of the objective and contribution of the acoustical resolution to the measurement.

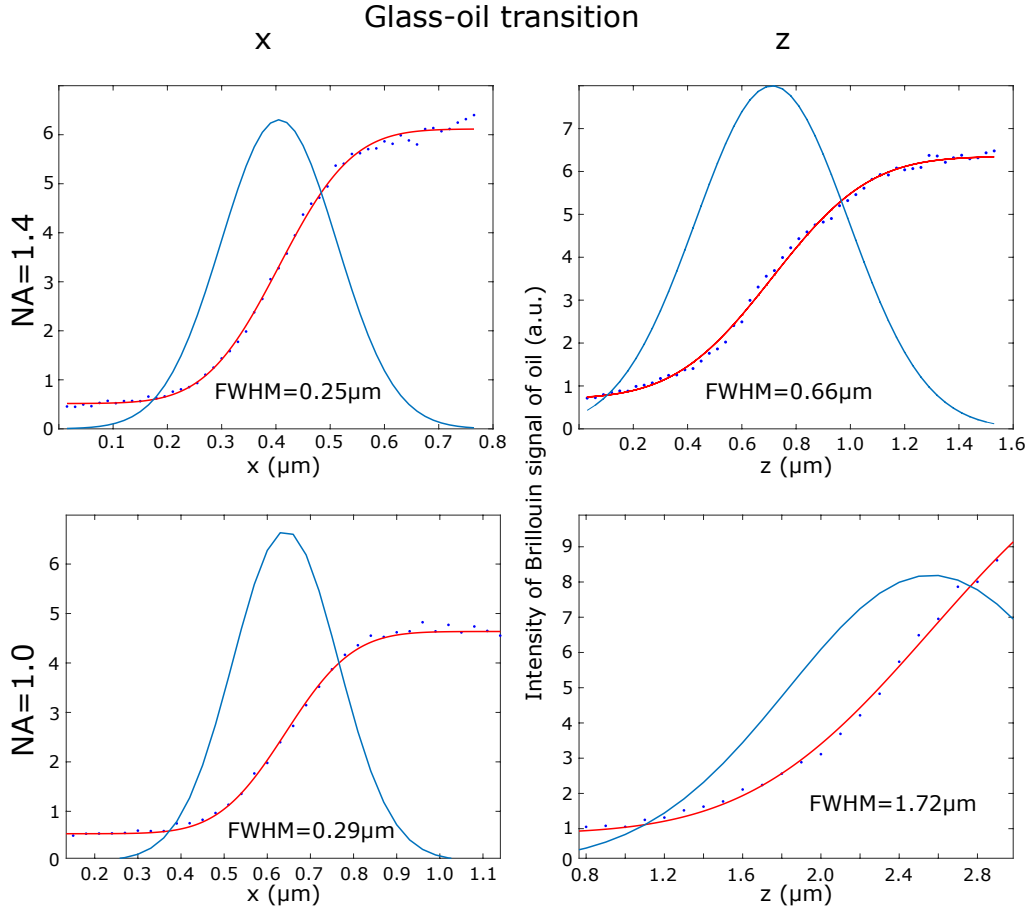


FIGURE 4.3: Step response at the oil/glass interface perpendicularly (x) and along (z) the optical axis of the objectives. A 1.4NA and 1.0 NA objective, commonly used in the setup, are measured. Blue dots are the raw data and the red solid line is a fit with an *erf* function. The blue solid line is the derivative of the fitted *erf* (gaussian function).

nominal NA	x	z	effective NA
1.0	$0.298 \pm 0.009 \mu\text{m}$	$1.758 \pm 0.011 \mu\text{m}$	0.85
1.4	$0.210 \pm 0.011 \mu\text{m}$	$0.661 \pm 0.009 \mu\text{m}$	1.28

TABLE 4.1: Spatial resolution of the confocal Brillouin microscope with two different objectives. The error is the standard deviation and the effective NA is calculated as the value that would theoretically produce the measured axial resolution.

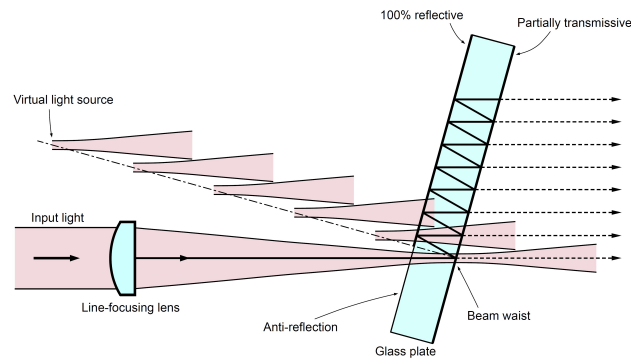


FIGURE 4.4: Principle of the VIPA. Image from https://en.wikipedia.org/wiki/File:Modified_Operational_principle_of_VIPA.jpg

4.2.2 Brillouin spectrometer

The spectrometer was designed and built by Dmitry Richter and it is based on a two-stage VIPA¹ configuration reported by Scarcelli and Yun [110].

The measurement of the Brillouin spectrum from biological samples is challenging because the Brillouin scattering is much weaker than elastic scattering ($\gtrsim 6$ order of magnitude weaker) and the Brillouin frequency shift is very small $\lesssim 10\text{GHz}$ ($\sim pm$). Therefore the spectrometer needs to have high resolution and high extinction. The high resolution is achieved by using a VIPA as a dispersive device and two VIPAs in a cross-axis configuration provide sufficient extinction. The VIPA is conceptually similar to a Fabry-Pérot interferometer. They are both based on two parallel (partially) reflecting surfaces. When the light is launched inside the device, multiple beams are created by the reflection on the two surfaces and they interfere at the exit. Depending on the optical path between the surfaces, some specific wavelengths are constructively interfering while others are destructively interfering, creating thus a narrowband filter. The distance between two subsequent wavelengths that are transmitted is named free spectral range (FSR) and represents the maximum extension of the spectrum that can be measured unambiguously. In a Fabry-Pérot the two surfaces have the same reflectivity and the direction of light propagation is perpendicular to the surfaces. Assuming perfect surface quality, this configuration allows having an arbitrarily large number of reflections, i.e. arbitrary high spectral resolution. The wavelength scanning is achieved by changing the distance of the reflecting surfaces (typically with a piezo). In a VIPA, instead, the back surface is 100% reflective

¹VIPA stands for Virtually-Imaged Phase Array

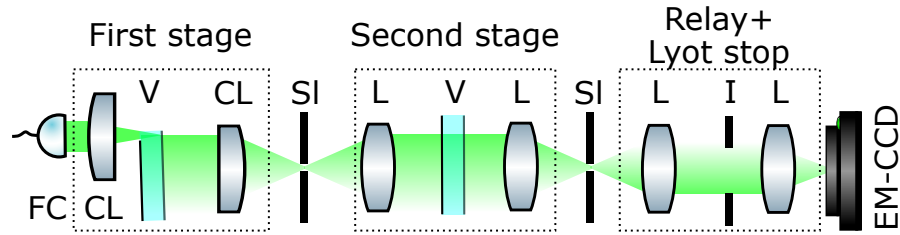


FIGURE 4.5: Optical schematic of the two-stage VIPA spectrometer. FC = fiber coupler/collimator, CL = cylindrical lens, V = VIPA, SI = slit, L = lens.

(figure 4.4) with a small AR-coated region, that serves as an entrance window for the light. The light is focused, through the AR-coated region, on the front surface (that is partially transmissive) at a small angle, so that the reflected light hits the 100% reflective part of the back surface, is entirely reflected and reaches the back surface again. As shown in figure 4.4, the multiple reflections behave like virtual sources having an exponentially decaying intensity and a constant phase delay, due to their spatial displacement (hence the name "Virtually-Imaged Phase Array"). The different configuration of the VIPA compared to the Fabry-Pérot entails two important advantages for the VIPA: it has higher throughput and it disperses the light angularly [111]. The first advantage comes from the fact that the light is fully transmitted, while in a Fabry-Pérot only one wavelength² is transmitted and the others are reflected. The second advantage is due to the fact that the light is focused, thus it has a certain angular distribution: light at different angles travels a different optical path; at the output, each different angle corresponds to constructive interference for a different wavelength. The main disadvantage is a lower spectral resolution since the number of reflections is limited by the walk-off of the beam.

The optical schematic of the spectrometer is shown in figure 4.5. The Brillouin signal is delivered to the spectrometer via a single mode optical fiber and the output is collimated by a collimator (F220FC-532, Thorlabs) providing a Gaussian beam with a diameter of 2.1mm ($1/e^2$). A cylindrical lens ($f=200\text{mm}$) focuses the light on the entrance of the VIPA (OP-6721-3371-2, Light Machinery) and a second cylindrical lens ($f=200\text{mm}$) generates, in its

²The transmitted bandwidth around the wavelength of constructive interference represents the spectral resolution. Therefore the higher the spectral resolution the lower the throughput.

focal plane, the interference pattern that corresponds to the spectrum. A single VIPA can only provide about 30dB extinction [110]. To increase the extinction, an adjustable slit blocks the strong peaks corresponding to the elastically scattered (Rayleigh) light (that are spatially separated from the Brillouin peaks) but their tails might be still more intense than the Brillouin signal. The second stage disperses the light (composed by the Brillouin signal and the residual Rayleigh) in the orthogonal direction, further increasing the extinction by 30dB. It is composed by two plano-convex lenses ($f=200\text{mm}$) in a 4-f configuration: in one direction they just relay the interference pattern from the first stage to the second slit, while in the orthogonal direction they act the same way as the cylindrical lenses in the first stage. The second slit blocks the peaks corresponding to the Rayleigh light: that does not increase the extinction of the spectrometer but avoids possible saturation of the camera (iXon DU897, Andor Technology). A 1:3.33 achromatic matched pair ($f_1 = 30\text{mm}$, $f_2 = 100\text{mm}$) magnifies the pattern for proper sampling on the camera and introduces a Lyot stop: that is an adjustable iris, positioned in the Fourier plane, that acts as a low pass spatial filter. The Lyot stop can further increase the extinction of the spectrometer by up to 20 dB [112]. In fact the elastically scattered light forms four spots ('laser' spots in figure 4.6), two of which are relatively close to the Brillouin peaks for water. Their intensity distribution is a convolution of the spectral pattern of the VIPA with an Airy function (due to the finite aperture of the lenses) and it thus shows high frequency components far from the peak. For highly scattering samples, the high frequency components can be stronger than the Brillouin signal but they can be effectively suppressed with the Lyot stop.

Once the spectrum is acquired, it needs to be converted from camera pixel to GHz. The dispersion of the VIPA is known to be non-linear (Appendix A.1) but the typical Brillouin shift of biological samples is close to the one of water. Therefore, if a linear relationship is assumed close to the Brillouin shift of water, the systematic error is small ($<0.1\%$, see appendix A.2). Naming d_{meas} the distance of the Stokes and anti-Stokes of water, in pixels, and $\Omega_{H_2O} = 7.46\text{GHz}$ the Brillouin shift of water, the calibration factor c can be calculated as

$$c = \frac{FSR - 2\Omega_{H_2O}}{d_{meas}} \quad (4.1)$$

where $FSR = 30\text{GHz}$ (from the specs of the VIPA used).

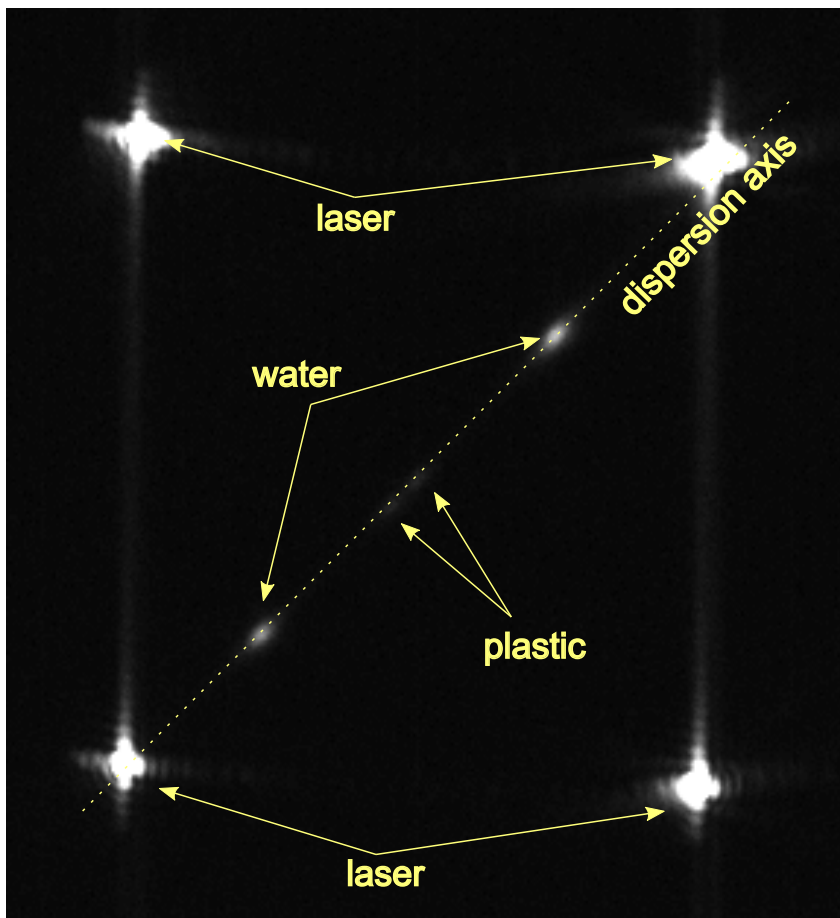


FIGURE 4.6: Raw output of the spectrometer (without Lyot stop); the signal is from a plastic cuvette filled with distilled water.

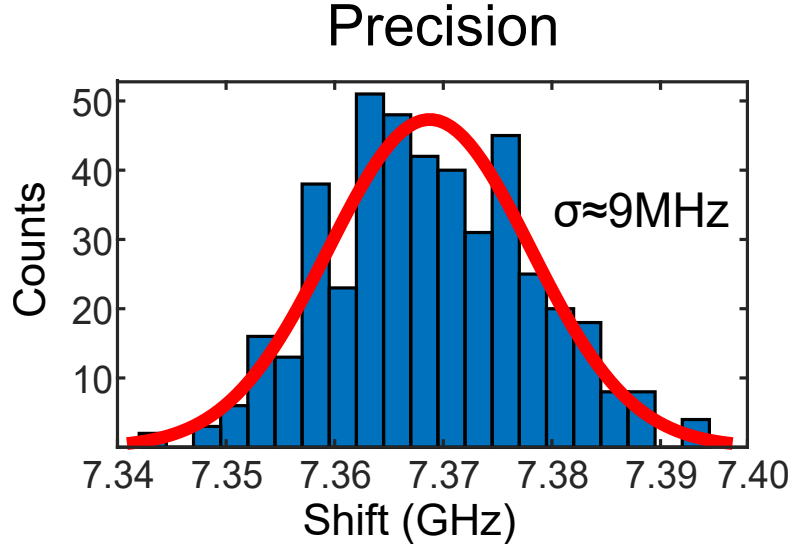


FIGURE 4.7: Precision histogram obtained by measuring the Brillouin shift of water 440 times (8.3 mW on the sample, 180 ms integration time). The data is fitted with a normal distribution ($\sigma \approx 9\text{MHz}$).

When acquiring an unknown spectrum, the Brillouin frequency shift Ω can be calculated as:

$$\Omega = \frac{FSR - c \cdot d_{meas}}{2} \quad (4.2)$$

The calibration spectrum from a water cuvette is acquired every 50 spectra from the sample and the calibration factor for each spectrum is calculated as the linear interpolation of the c from the preceding and following calibration spectrum.

4.2.2.1 Spectral precision

The minimum detectable difference in mechanical properties is determined by the precision in measuring the Brillouin shift. In the assumption that the Brillouin signal consists only of a single (Stokes and anti-Stokes) peak, the precision can be determined by measuring multiple times the Brillouin shift of a water sample (figure 4.7) and calculating the standard deviation of the measurements. I found a precision of about **9MHz** with 8.3mW on the sample and 180 ms integration time. The values for the optical power on the sample and integration time are comparable to other VIPA-based confocal microscopes at 532nm (Table 1 in [46]). Note that the precision is dependent on the SNR [111], that in turn depends on the total illumination energy³. It is

³The SNR is proportional to the square root of the total illumination energy (i.e. the number of photons) in shot noise limited conditions

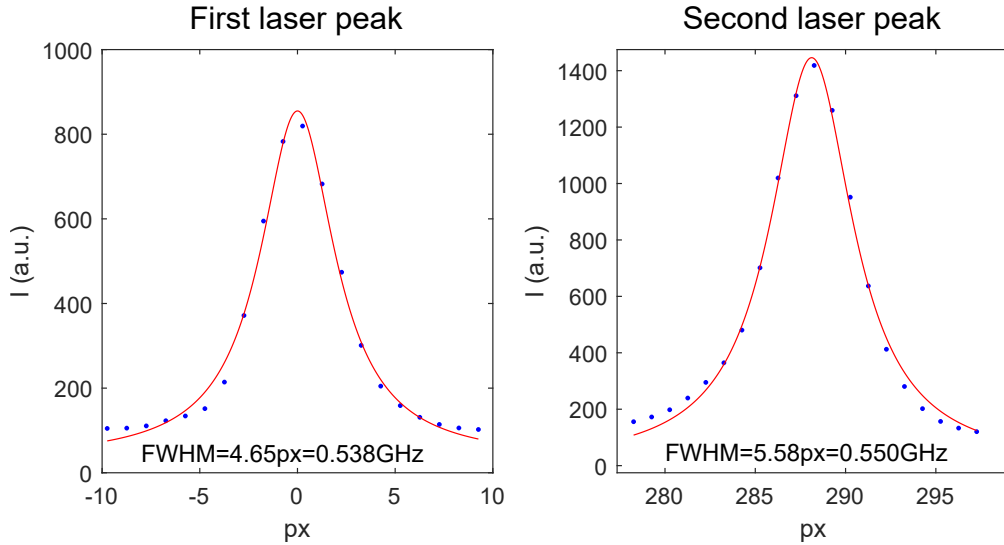


FIGURE 4.8: Linewidth of the laser measured by the spectrometer, which corresponds to its spectral resolution. The blue dots are the raw data while the red solid curve is a Lorentzian fit. Due to the periodicity of the VIPA pattern, multiple laser peaks are visible: in the figure, the two brightest are shown.

thus necessary to always mention the total illumination energy when reporting the precision.

4.2.2.2 Spectral resolution

The spectral resolution of the spectrometer can be measured by looking at the linewidth of the laser. In fact, the intrinsic linewidth of the laser is 1MHz that is much smaller than the expected resolution of the spectrometer (hundreds of MHz) and it can thus be considered a δ function.

Figure 4.8 shows the laser peaks fitted with a Lorentzian curve. Multiple laser peaks are present due to the periodicity of the VIPA pattern but their intensity is decaying with a gaussian envelope. Therefore I only used the two brightest peaks for the analysis. Note that the FWHM in pixels is different for the two peaks (20% difference) due to the nonlinearity of the VIPA (see section A.1). By using the relationship and the coefficients calculated in section A.2, it is possible to convert the FWHM in GHz and correct for the nonlinearity. After conversion the two peaks have a FWHM of 538MHz and 550MHz respectively, corresponding to a difference of only 2%. The average is **544MHz**. The ratio between the FSR and the resolution (FWHM) is called finesse. The maximum achievable finesse is limited by the dimension of the VIPA and its surface quality. For the VIPA we are using the manufacturer reported a target finesse of around 64 and I measured a finesse is 55, that is quite close to the expected value.

4.2.2.3 Extinction

The extinction (or spectral contrast) is a measure of the weakest intensity that can be reliably measured close to a bright spectral feature. It is a very important parameter in Brillouin imaging since the signal of interest (Brillouin peaks) is close in frequency and several orders of magnitude weaker than the elastically scattered light.

The expected extinction of the spectrometer, including the Lyot stop, is 80dB [112], that is much larger than the dynamic range of the camera. In order to measure it, one needs to acquire different portions of the spectrum with different optical power and/or camera exposure time and then stitch them together. I first sent some laser light to the spectrometer, by placing a mirror in the sample holder of the microscope. The optical power at the input of the spectrometer (measured with a powermeter) was 12 μ W. While having the slits blocking the intense laser light, I acquired one spectrum with the Lyot filter (100ms exposure time, no EM gain) and one without the Lyot filter (20ms exposure time, no EM gain). I then opened the slits, attenuated the laser with a ND filter, so that the input optical power at the spectrometer was 32nW, and acquired a spectrum with 0.2ms exposure time (no EM gain). I measured the offset intensity of the camera (around 100 counts) from a region without light and subtracted it from all the acquired images. I reconstructed the spectra by taking the same line profile for all the images in FIJI [113] and normalized them by dividing by the product of the optical power times the exposure time. In order to have a value that is relative to the laser, I divided all the spectra by the maximum value in the laser spectrum and took 10 times the log₁₀ of the intensity to convert the intensity in dB. I cropped the two regions with the laser peaks from the spectrum acquired with the slits opened and plotted them in the same graph with the central region of the two spectra acquired with the slits closed in order to generate the plot in figure 4.9. I didn't plot the points in between the two sections because they don't merge smoothly (due to additional peaks created by the light diffracted from the slits) and they do not affect the Brillouin measurement. The measured extinction ratio is in good agreement with the literature [110, 112] where a two-stage VIPA spectrometer was shown to provide about **55dB** of extinction and the Lyot stop additional **20dB**.

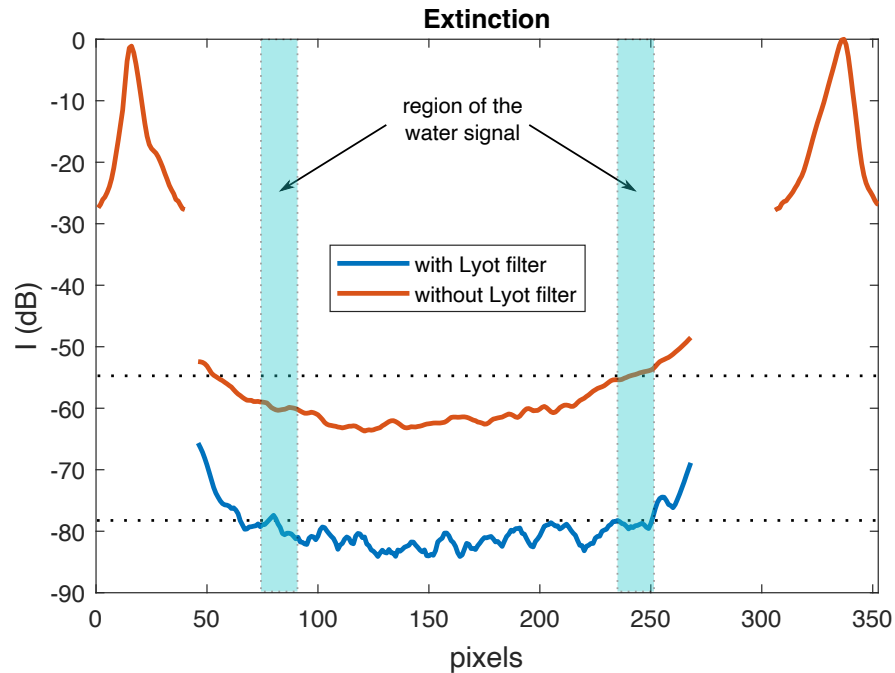


FIGURE 4.9: Extinction of the Brillouin spectrometer with (blue line) and without (orange line) the Lyot stop. The dotted lines represent the minimum intensity of the Brillouin signal that can be detected.

4.2.3 Confocal fluorescence

As mentioned in section 4.1, having a fluorescence confocal microscope co-aligned with the Brillouin microscope is essential in order to measure tissue-specific mechanical properties or correlate them to underlying molecular constituents. In fact, fluorescent microscopy is a powerful and very well established technique to label and image specific tissues or molecules with high specificity.

An additional 488nm diode laser is coupled into the same fiber as the Brillouin laser and it can be used as excitation for GFP-like fluorophores (figure 4.11 shows an example image of a fibroblast cell labeled with GFP) while the Brillouin laser at 532nm can be used for the excitation of mCherry-like fluorophores (see figure 4.10 for the excitation and emission spectra of GFP and mCherry). Although 2 colors imaging is possible, it is better to avoid the use of mCherry-like fluorophores: the high intensity of the Brillouin laser will largely bleach the fluorophore, thus making it not possible to perform fluorescence imaging after Brillouin imaging and potentially increasing the photodamage.

A narrowband bandpass filter (LL01-532, Semrock) is used to separate the emitted fluorescence from the Brillouin signal: when mounting the filter almost perpendicular to the direction of light propagation, the light at

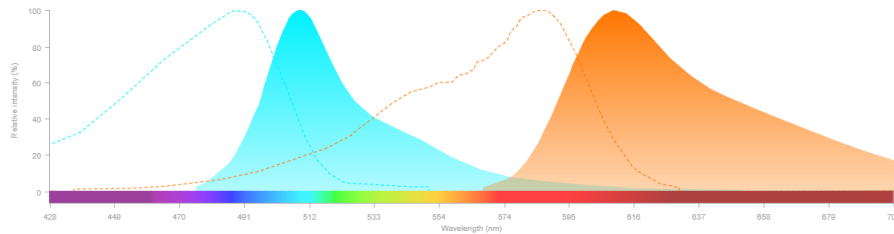


FIGURE 4.10: Excitation (dashed line) and emission (filled curve) of GFP (blue) and mCherry (orange). [Data from <https://www.thermofisher.com/order/fluorescence-spectraviewer>]

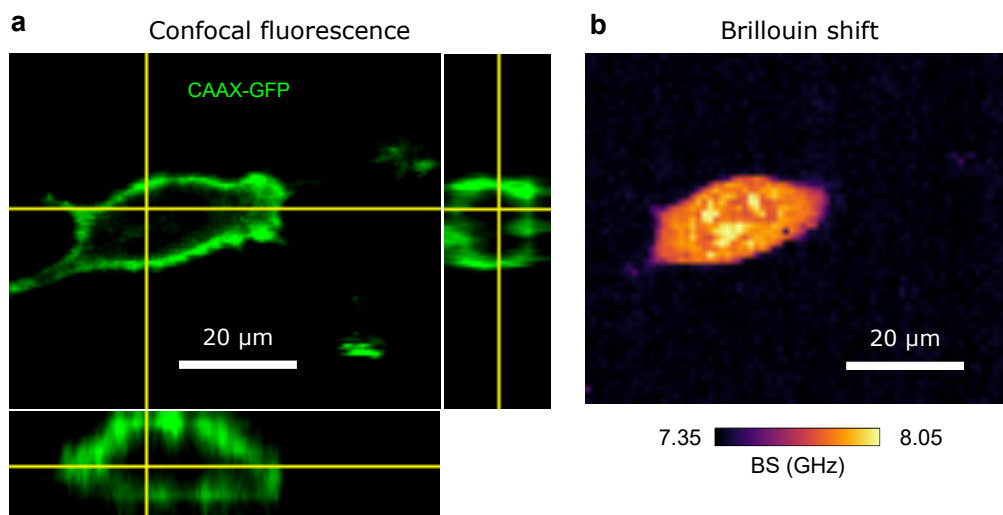


FIGURE 4.11: a) Orthogonal projects from a 3D stack of a fibroblast cell; membranes are labeled with CAAX-GFP b) Corresponding Brillouin image from a single plane.

$532 \pm 4\text{nm}$ (that includes the excitation laser and Brillouin signal) is transmitted while everything else is reflected and can be sent to the photomultiplier tube (PMT). Note that the filter can not be placed in the optical path between the laser and the microscope otherwise it would block the 488 excitation laser. The solution to this issue was to place the filter after the PBS, right before the fiber coupler that delivers the light to the Brillouin spectrometer (refer to figure 4.2). Under the assumption that the fluorescence light is completely unpolarised⁴, only half of it will be reflected by the PBS and be detected. After the filter, a plano-convex lens ($f = 75\text{ mm}$) focuses the fluorescence light on a pinhole and the transmitted light is detected by the PMT (PMT1001, Thorlabs). The pinhole size is determined by the diameter of the Airy disk, given by $2.44f\frac{\lambda}{d}$ where λ is the wavelength, f the focal lens of the lens focusing the light on the pinhole and d is the beam diameter before the lens. Assuming a beam diameter of 1.8mm (the actual beam diameter depends on the objective) and a wavelength of 510nm (peak emission of GFP) the diameter of the Airy disk is $52\mu\text{m}$. The pinhole size was chosen to be $40\mu\text{m}$, corresponding to ~ 0.8 Airy units.

In a commercial fluorescence confocal microscope, typically a pair of galvanometric mirrors are used to scan the focal spot in the sample in a step-wise manner; in this configuration, the fluorescence signal from a single point is collected over a certain (settable) time before moving to the next point. The same strategy could be used when scanning the sample but that would substantially increase the dead time between pixels, during the acceleration and deceleration phase: galvanometric scanners are designed to have a very small mechanical inertia while that is not the case for the stage and sample. Furthermore, each acceleration/deceleration phase can cause some drift of the sample, when it is not strongly attached to the dish. A possible solution is to move the stage continuously when acquiring a line; in that way, the acceleration (deceleration) is only at the beginning (end) of the scan and it can be made smaller without significantly increasing the dead time. When acquiring a 3D volume the axis along the longest dimension of the volume is set as the one moving continuously (termed "fast axis") and the other two (termed "slow axis") are moving in a step-wise fashion (see figure 4.12). The controller of the piezo stage is programmed to output the current position of the fast axis in one channel and the "on target" signal on another. The "on target" signal is a digital signal that is high when the stage is being held at the set position and low when the stage is moving. Thus its falling edge

⁴That is true if the fluorophore is in a random orientation in the sample.

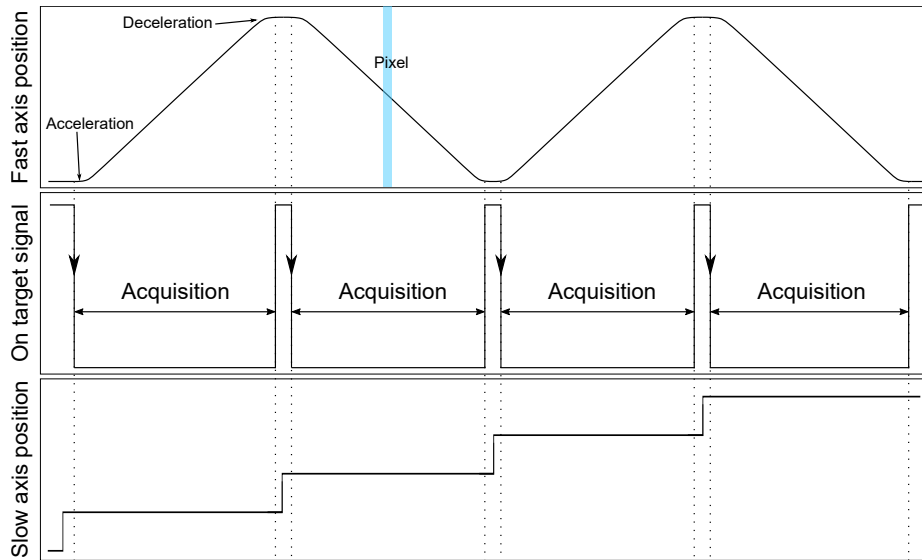


FIGURE 4.12: Time diagram of the confocal fluorescence acquisition.

signals the start of the movement and can be used to trigger the acquisition from the PMT. The synchronization of the slow axis with the fast axis and the image reconstruction is done via the self-written LabVIEW software. A DAQ card (PCIe-6323, National Instruments) is used to sample the signal from the PMT and the position of the fast axis. Data is acquired at the maximum sampling rate allowed by the DAQ (125kS/s, that is one sample each $\Delta t = 8\mu\text{s}$). The speed of the fast axis is chosen so that N points ($N = 25$, typically) are averaged to get the signal from a single pixel; e.g. with a pixel size of $\Delta L = 0.25\mu\text{m}$ and $N = 25$ averages per pixel the speed of the stage is $\frac{\Delta L}{N\Delta t} = 1.25\text{ mm s}^{-1}$. The position of the fast axis is sampled in parallel with the PMT signal and it is used to assign the fluorescence signal to the corresponding spatial position during the image reconstruction and to correct for non-linearity of the stage position vs. time (especially in the acceleration and deceleration phase).

4.2.4 Graphical User Interface

The Graphical User Interface (GUI) of the LabVIEW software that controls the microscope plays an essential role in facilitating the use of the microscope. Indeed, in light of the goal of establishing the technique mentioned in section 4.1, an accessible software interface reduces the time necessary to learn how to use the microscope independently, thus making it possible for more people to use it and explore different biological questions and samples.

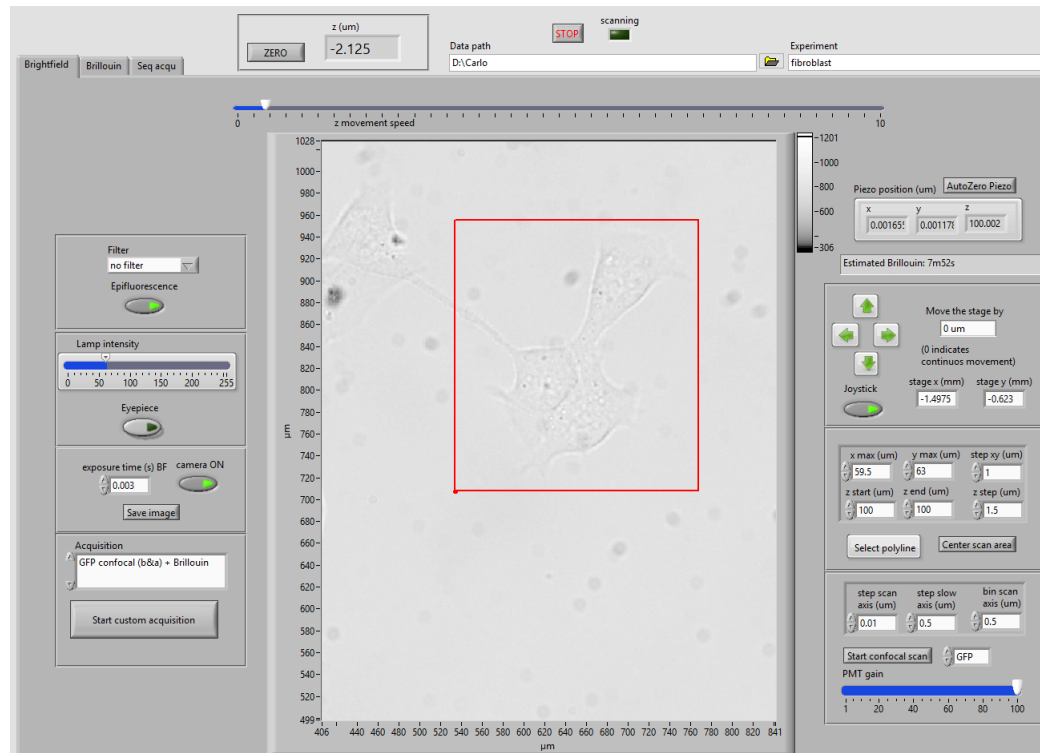


FIGURE 4.13: Graphical interface of the LabVIEW program that I wrote for controlling the confocal Brillouin microscope. The brightfield (or fluorescence) image of the sample can be used to select in real-time the ROI (red box), while moving the motorized stage (green arrows) and adjusting the focus (mouse wheel).

Specifically, the following features make the acquisition more intuitive and less time consuming for the user:

- The area to be imaged can be visualized and selected from the brightfield or epifluorescence image of the sample (see figure 4.13). Arbitrary polygonal areas are possible in addition to rectangular areas.
- Image reconstruction (fitting of the Brillouin peaks and assignment of the pixels) is done in real-time (see figure 4.14) and provides instantaneous feedback to the user (especially useful for long acquisitions).
- Automatic acquisition of multiple ROIs with a customizable schedule and using multiple modalities (Brillouin, brightfield, epifluorescence, confocal fluorescence); designed by me and Tim Dullweber and written mainly by Tim.

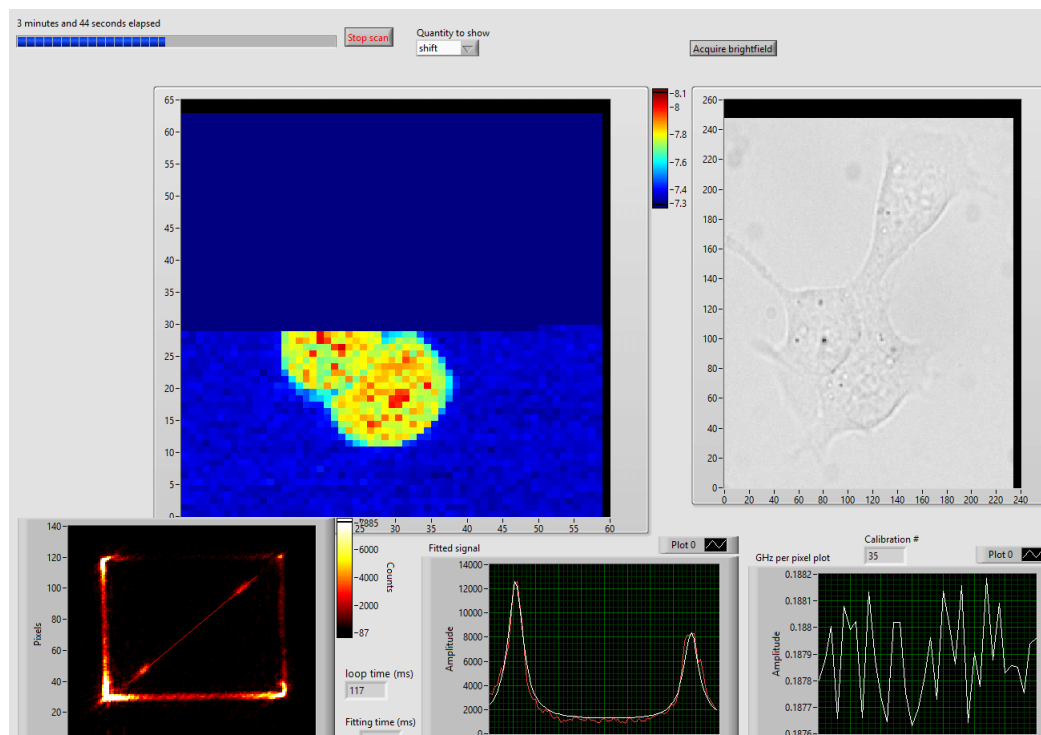


FIGURE 4.14: Sub-VI that is controlling the Brillouin acquisition. The reconstructed Brillouin image is shown in real-time (providing instantaneous feedback to the experimenter) together with the raw camera image from the spectrometer, the fitted spectrum (to assess the signal quality) and the calibration from the water cuvette (to monitor the drift of the laser).

4.3 Biological projects

As already mentioned in section 4.1, the main goal of this part of my PhD project was to apply Brillouin microscopy to address biological questions. In the next sections, I will present two main biological projects in which I was involved and which led to a scientific publication. I will also briefly present other projects that took advantage of the confocal Brillouin microscope and in which I was involved, though to a lesser extent. Some of these are still ongoing.

4.3.1 Imaging sub-micron extra-cellular matrix in zebrafish notochord

In this section I will briefly present the work done by me and Héctor Sánchez-Iranzo on the analysis of the extra-cellular matrix (ECM) surrounding the notochord in zebrafish using Brillouin microscopy. Sample preparation and acquisition was done by Héctor Sánchez-Iranzo. Both me and Héctor worked on analyzing the data. The findings I am presenting here are published in *Biomedical Optics Express* [36].

The extra-cellular matrix (ECM), together with the cytoskeleton, is one of the main components that determines the mechanical properties of biological tissues. As mentioned in section 1.1, mechanical properties play an important role in certain developmental processes; this is likely the case for zebrafish notochord. The notochord is one of the anatomical features that define animals in the phylum Chordata and provides structural support to the developing zebrafish embryo [114]. Figure 4.15 shows a schematic of the zebrafish notochord at 3 days post fertilization (dpf). It has the shape of an almost perfect cylinder (figure 4.15c) and it is composed of two cell types: sheath cells and vacuolated cells. Most of the volume of the vacuolated cells is occupied by a vacuole, which contains fluid under high hydrostatic pressure, while the sheath cells are epithelial cells that surround the vacuolated cells and form the "wall" of the cylinder. They secrete the ECM from their basal surface. The ECM is likely to play a crucial role in withstanding the high pressure generated by the vacuoles and to provide structural integrity to the notochord. In fact, inhibition of collagen crosslinking shows a distorted notochord as a phenotype [115]. However, the direct measurement of the mechanical properties of the ECM in-vivo is not possible with the standard techniques (see section 1.2) because it is a thin layer embedded in a

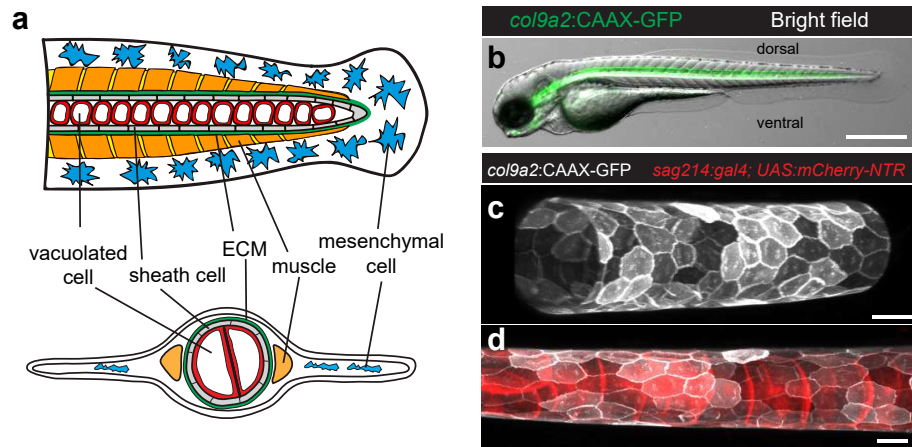


FIGURE 4.15: Characterization of the zebrafish notochord at 3 days post fertilization (dpf). Panel a shows a schematic of the notochord both in a lateral (top) and cross section (bottom) view. Panels b-d show microscopy data from a transgenic fish in which sheath cells are labeled with GFP and vacuolated cells are labeled with mCherry. Panel b is a brightfield image with overlapping GFP signal (sheath cells) while panels c and d are maximum projections from fluorescence confocal images. Scale bars, 500 μm in (b), 20 μm in (c and d). The figure was prepared by Héctor Sánchez-Iranzo and published in Bevilacqua et al. [36].

different tissue. When we imaged a zebrafish at 3dpf (figure 4.16) we observed a line of high Brillouin shift running along the notochord that could potentially be originated from the ECM. The confocal fluorescent imaging confirmed that the high Brillouin shift is next to the sheath cells (figure 4.16a) that secrete the ECM. A closer look at the Brillouin spectra collected along the ECM layer (figure 4.17a) showed that they can be decomposed into the sum of two Lorentzian peaks (blue and orange curves). The peak having a high Brillouin shift is only present in a thin region (less than $1\mu\text{m}$) (figure 4.17b), it can thus be assigned to the ECM. But the other peak also shows a different Brillouin shift in the ECM region (figure 4.17c). Therefore, we interpreted the two peaks as being generated by two acoustic modes (bulk and parallel-to-surface) within the ECM as was shown in isolated collagen fibers [116]. Additionally, by plotting the ratio between the area of the high-shift peak and the total area under the Brillouin spectrum (figure 4.17d-e) we could determine the thickness of the ECM layer: after deconvolving the curves in figure 4.17e (using an independent measurement of the PSF, see table 4.1) we found a thickness of $488 \pm 72\text{nm}$, in very good agreement with EM measurements ($390 \pm 58\text{nm}$) [36].

In conclusion, with a careful spectral analysis, we could determine both the mechanical properties and the thickness of a thin (less than 500nm) ECM

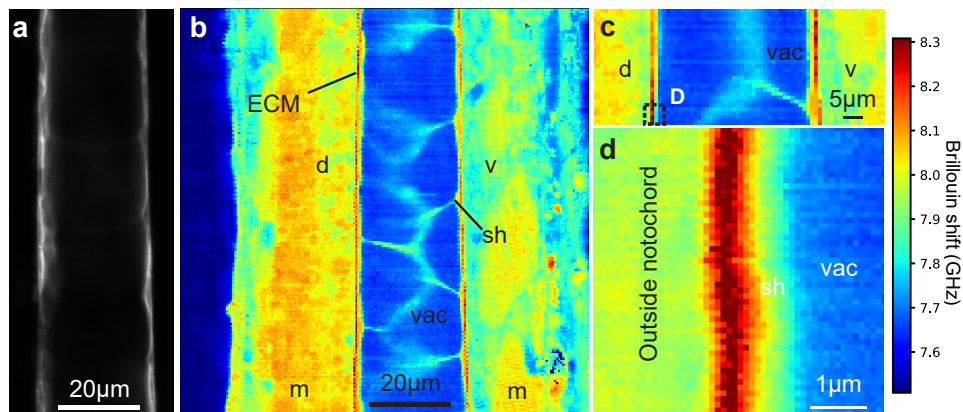


FIGURE 4.16: Brillouin imaging of a 3dpf zebrafish notochord. Panel a shows the fluorescence image of the sheath cells and panel b shows the Brillouin shift map in the corresponding region. Note that the different tissues can be clearly distinguished based on the Brillouin shift (m=muscle, vac=vacuole, sh=sheath cells). A line with a higher Brillouin shift can be observed next to the sheath cells. It becomes more visible when acquiring an oversampled image with a step size of $0.1\mu\text{m}$ (c-d). (d=dorsal, v=ventral). Figure adapted from [36].

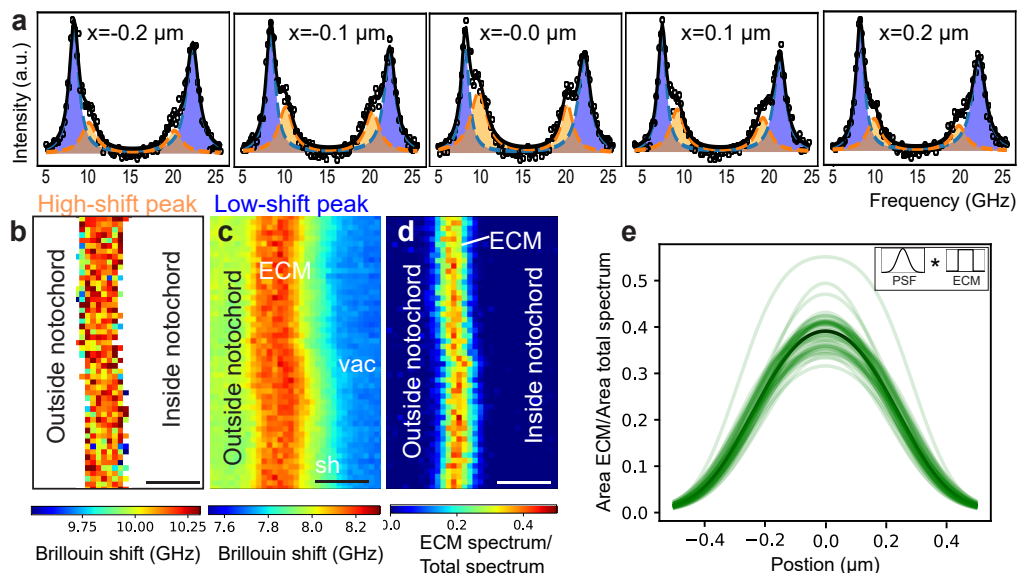


FIGURE 4.17: Analysis of thin ECM layer in vivo. The spectra along the ECM are composed by a double Lorentzian peak (a). When plotting the Brillouin shift of the two peaks separately, the high-shift peak is present only in the ECM (b) while the low-shift peak is still clearly distinguishable from the surrounding tissue (c). The ratio between the amplitude of the two peaks (d-e) allows quantifying the thickness of the ECM. The scalebars in b-d are $1\mu\text{m}$. Figure adapted from [36].

layer in the notochord of a living zebrafish. Having access to this information, *in vivo*, could potentially help in studying the process of notochord formation and what role the ECM plays. Specifically, measuring the mechanical properties of the ECM over time and space and performing perturbation experiments on sheath and vacuolar activity can help inform how the perfect cylindrical shape is achieved. From there a more general understanding of tube morphogenesis and the role that mechanical anisotropies have in this process could be gained.

4.3.2 Mechanical mapping of mammalian follicle development

In this section I will present the work on the mechanical mapping of follicle development in mice, that was published in *Communications biology* [39]. The sample preparation, data acquisition were done by Chii Jou (Joe) Chan and we worked together on the data analysis and interpretation.

The proper development of follicles is essential for the production of mature oocytes, thus having important implications in fertility. A schematic of the process is shown in figure 4.18: initially, the follicles are in the primordial state and, after activation, they transition to the primary state, characterized by a change in the shape and proliferation of somatic cells; then to the secondary state, where the somatic cells rearrange into several layers and an additional outer layer of cells (theca) is formed; the antral stage follows, where some fluid pockets start to emerge until the follicle is mature and the oocyte can be released (ovulation). Recently it has been shown that mechanical stress plays a role in maintaining oocytes dormant in the primordial state [117], suggesting that mechanical properties have a role in the follicle development. Another study reported mechanical differences within the ovary [118], but they had to bisect the ovaries, which might alter their mechanical properties. Brillouin microscopy can instead provide a mechanical map of the follicles within the intact ovary.

In the manuscript, we reported both the Brillouin shift and the Brillouin loss tangent (BLT), that can be interpreted as a measure of the micro-viscosity (see section 2.5). The BLT has the advantage of being independent of the local optical properties (refractive index) and density of the sample, that might be the driving factor in the observed changes of the Brillouin shift in a complex tissue such as the ovary. Previous studies [35, 38] have reported the BLT with the aim of decoupling the material properties (refractive index and density)

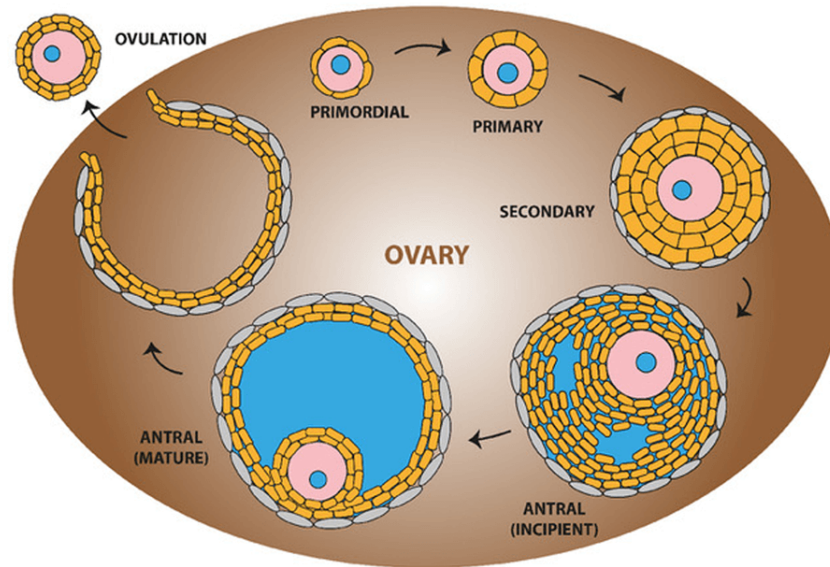


FIGURE 4.18: Schematic of the developmental cycle of follicles during mouse folliculogenesis. A follicle consists of the oocyte (pink) with its nucleus (blue), surrounded by the somatic cells (orange) and theca cells (gray). The oocyte grows in size during the transition to the secondary follicle stage, followed by the emergence of a fluid-filled lumen (blue) in the antral follicle stage. The oocyte is eventually released during ovulation, and upon fertilization undergoes embryo development. The interstitial tissues of the ovaries comprise stromal cells, extracellular matrix, and vasculature. Figure taken from [39] and made by Chii Jou Chan.

from the mechanical properties or determining the contribution of bound water to the measured mechanical properties [40].

Here I will summarise our main findings, following the same structure as in [39]:

The ovary exhibits regional differences in tissue mechanical properties When comparing the cortex, where the primordial follicles reside, with the interior part of the tissue in P7 and P14 ovaries (figure 4.19), we observed a higher BLT in the latter. This might suggest that the mechanical properties play a role in the positioning of the follicle within the ovary.

Mechanical compartments emerge during follicle maturation When looking at follicles from the preantral to the mature antral stage we found that an outer shell (consistent with the layer of theca cells) with increasingly higher BLT (figure 4.20a) starts to emerge. We then looked at the average BLT of oocytes from the primordial to antral stage (figure 4.20b) and observed a significantly higher BLT of the oocytes in primordial follicles compared to secondary and antral.

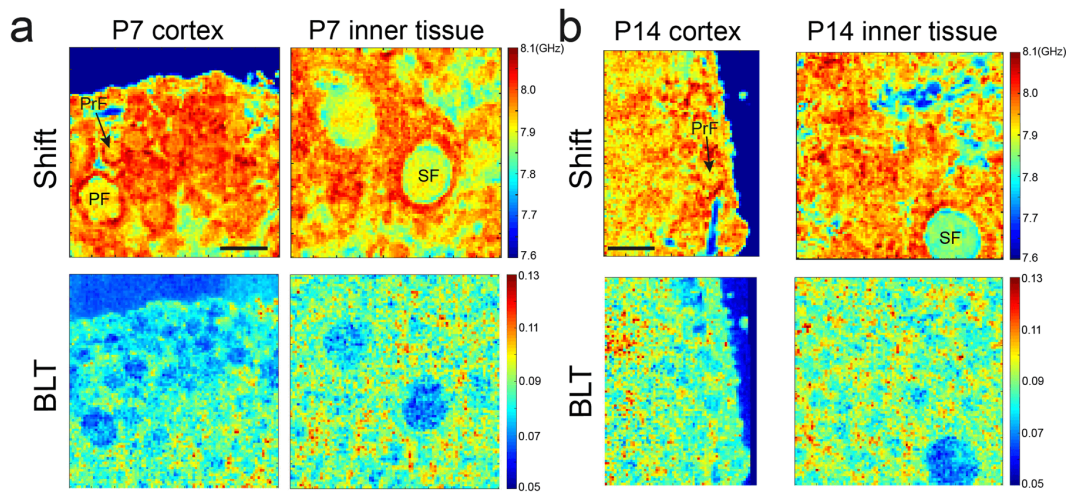


FIGURE 4.19: Maps of Brillouin shift and the corresponding BLT for a P7 ovarian cortex and the inner tissue (a). Both images were obtained from the same ovary. Primordial follicles (PrF) and primary follicles (PF) reside primarily in the cortex while the secondary follicles (SF) tend to be found in the inner part of the ovary, which shows a higher interstitial BLT. Maps of Brillouin shift and BLT for a P14 ovarian cortex and the inner tissue (b). Similar to P7 ovaries, higher BLT is associated with the inner tissue of the ovaries, compared to the cortex. Scale bar = 40 μ m. Figure taken from [39] and made by Chii Jou Chan.

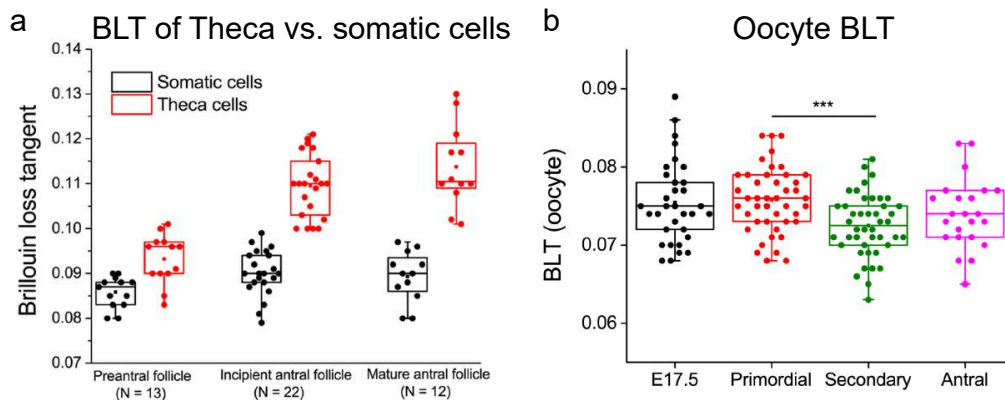


FIGURE 4.20: Boxplot of BLT for the outer theca cells versus the inner somatic cell layer of follicles at various stages of development (a). Each data point corresponds to the average signal of somatic or theca cells in one follicle. Boxplot of BLT for oocytes at various stages of follicle development (b). Each data point corresponds to the average signal of one oocyte. $N=35, 45, 45, 21$ for E17.5 germ cells and oocytes from primordial, secondary, and antral follicle stage, respectively. $***P<0.001$. Figure adapted from [39]; plots made by Chii Jou Chan.

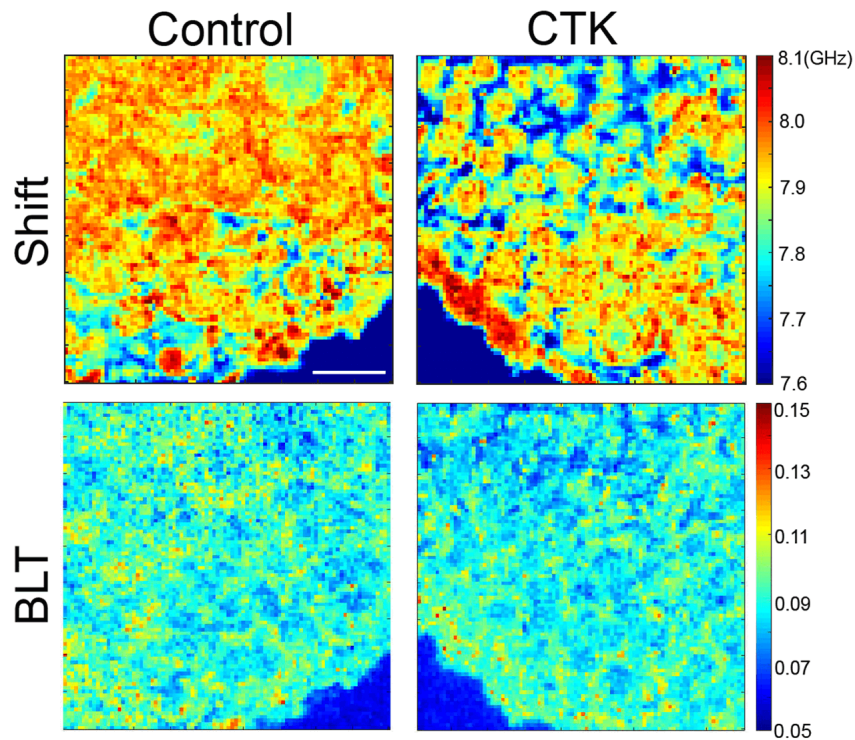


FIGURE 4.21: Top row: Brillouin shift of a P14 ovary when treated with CTK, which digests collagen matrix. CTK leads to a clear increase in the interstitial space (blue) between the primordial follicles at the cortex. Bottom row: Corresponding BLT maps. Scale bar = $40\mu\text{m}$. Figure taken from [39] and made by Chii Jou Chan.

Higher BLT correlates with interstitial ECM deposition Second harmonic generation (SHG) showed the presence of interstitial collagen in the P14 and P21 ovaries; to check whether the collagen is contributing to the BLT signal, Joe treated P14 ovaries with CTK, a drug that digests the ECM. Following the treatment, a decrease in the interstitial BLT signal can be observed (figure 4.21).

In conclusion, our work showed, for the first time, a mechanical map of mammalian ovaries with subcellular resolution, over time. This study is a starting point to further investigate the role of mechanical properties during follicle development.

4.3.3 Other projects

As I already mentioned in section 4.1, I developed the confocal Brillouin microscope with the aim of making it more readily available to biologists; indeed the microscope was used by several collaborators. My main contribution was to provide technical support with the microscope, discuss the best

choice of objective lens and sample mounting strategies and implement new features in the LabVIEW software that might be beneficial for the specific project. I will briefly present the projects that lead to some interesting findings or are still ongoing.

Geisler et al. [64] employed the confocal Brillouin microscope to complement their study on the role of intermediate filaments in endotube morphogenesis and function in the intestine of *c. elegans*. They found that intermediate filaments are positioned between the stiff brush border and soft cytoplasm and could thus serve as a mechanical buffer between the two different regions and accommodate the deformations and movement of the lumen during food intake.

Júlia Garcia Baucells and Marketa Schmidt Cernohorska from the Dammermann lab at the University of Vienna are looking at the mechanical properties of centrosomes in human cell lines and *c. elegans* embryos. Theresa Schlamp from the Greb lab at the university of Heidelberg is studying the difference in mechanical properties of shoot apical meristem in *arabidopsis* upon drug treatments or in mutants that have an effect on the cell wall.

Grégoire Lemahieu from the Cavalcanti-Adam lab at the Max Planck institute for medical research in Heidelberg is characterizing the mechanical properties of self-made alginate spheres to determine their homogeneity and the mechanical properties of cells growing inside them.

Muzamil Majid Khan from the Pepperkok team at EMBL in Heidelberg is studying the effect of fibrosis on the mechanical properties of *ex vivo* mouse lung tissue.

4.4 Limitations

Despite the great potential and advantages of a confocal Brillouin microscope highlighted in this chapter, some biological samples or processes cannot be imaged with it. In fact, the acquisition time for a single point is on the order of 100ms, limited by the very weak Brillouin signal. As an example, imaging a volume of $100\mu\text{m}\times 100\mu\text{m}\times 100\mu\text{m}$ (e.g. a mouse embryo) with such an acquisition time and a step size of $2\mu\text{m}$ takes around 200 minutes. During such a long time the sample can develop or move. One could increase the optical power of the incident laser to reduce the acquisition time, but this will increase the photodamage to the sample and, in any case the lowest acquisition time is limited by the readout time of the camera. Thus, to improve the

speed and reduce photodamage a different approach must be taken. In the next chapter, I will present our work in that direction.

Chapter 5

Line-scanning Brillouin microscope (LSBM)

In this chapter, I will describe the work presented in Bevilacqua et al. [65], currently under review. The microscope was designed by me and Robert Prevedel and built and characterized by me. The contribution of the other authors is acknowledged in the corresponding sections.

5.1 Motivation

As mentioned in section 4.4, confocal Brillouin microscopy is affected by relatively slow acquisition time and potential photodamage. When looking at living biological samples, these limitations might preclude the investigation of certain processes. For example, gastrulation in *Drosophila* is a developmental process in which mechanical properties are believed to play a fundamental role, but their measurement is quite challenging because the cells involved are changing their shape and moving fast (i.e. in about 20 minutes they invaginate and form a furrow). Regarding the possible photodamage, mouse embryos are an established model to study mammalian development and it would thus be insightful to study their mechanical properties during development (i.e. following the same embryo over time) without impairing their viability but they are notoriously light sensitivity.

Confocal fluorescence microscopy is also affected, to a certain extent, by long acquisition time and potential photodamage of the sample. Lightsheet fluorescence microscopy improves both aspects [120]: millions of points¹ are acquired in parallel leading to very large multiplexing (figure 5.1a), thus a tremendous increase in the acquisition speed and the sample is only illuminated in the volume that is being imaged - hence the name "Selective Plane

¹A camera can typically have 1000x1000 pixels forming its sensor.

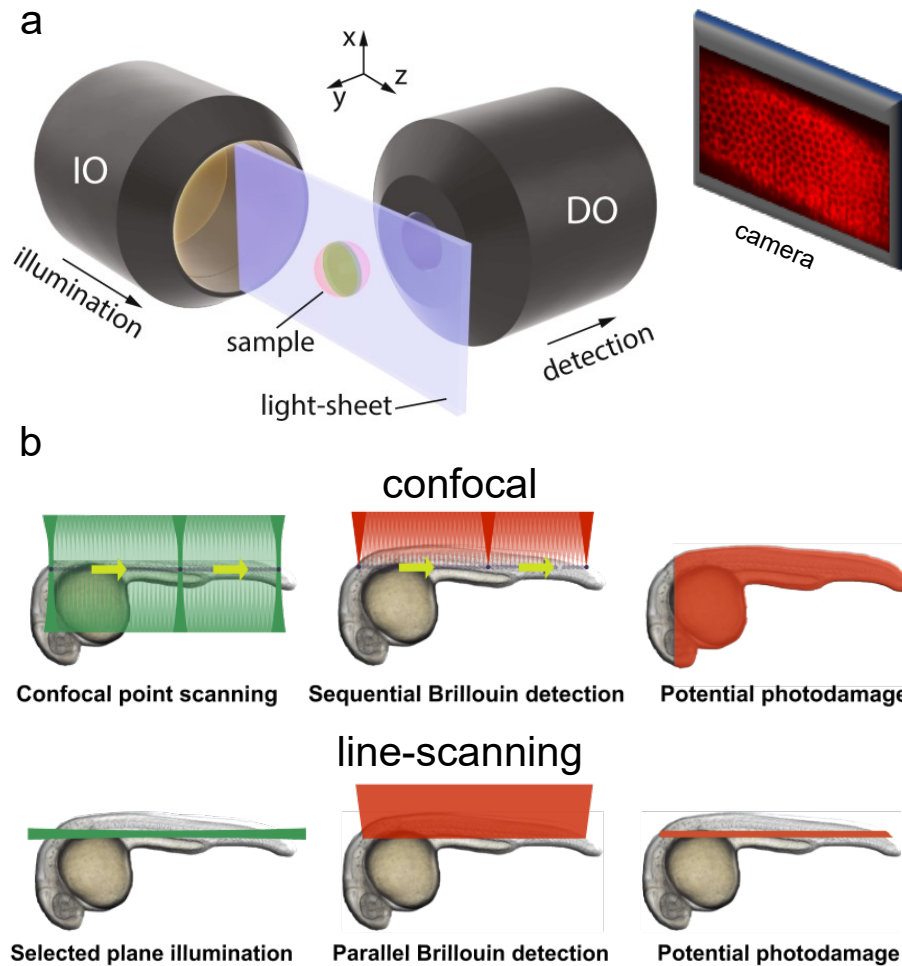


FIGURE 5.1: a) Principle of lightsheet fluorescence microscopy: a whole plane in the sample is illuminated and imaged on the camera, leading to large multiplexing (a camera can typically have more than 1 million pixels). Figure adapted from [119]. b) In confocal microscopy the illuminated volume is much larger than the imaged volume, thus increasing the portion of the tissue that is potentially affected by photodamage; in contrast in line-scanning microscopy only the imaged region is illuminated.

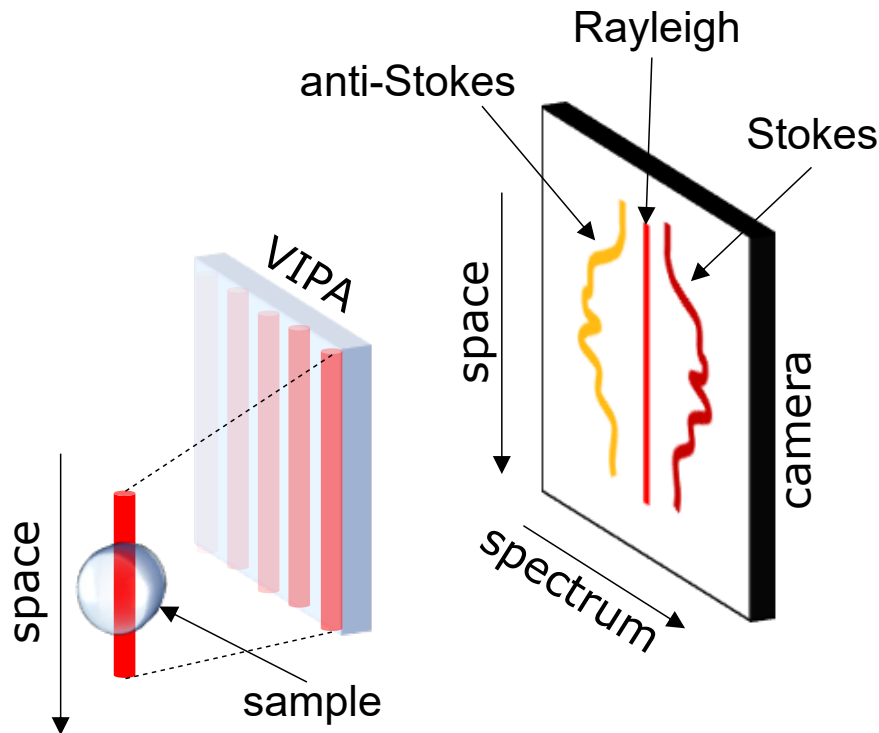


FIGURE 5.2: Principle of multiplexing for Brillouin imaging. The Brillouin signal coming from a line on the sample is spectrally dispersed by a VIPA. On the camera one dimension carries the spectral information while the other retains the spatial information.

illumination microscopy" (SPIM) - thus restricting the potential photodamage (figure 5.1b).

The question is whether we can use a similar strategy in Brillouin microscopy. In the next section, I will answer that question and present the related challenges.

5.2 Design principles and challenges

In Brillouin microscopy, one needs to collect a spectrum from each point in the sample. When using a 2D sensor (camera), one dimension needs to be used for the spectral information and only one spatial dimension is left (figure 5.2). Therefore only one line can be acquired in a single camera frame (instead of a whole plane in the case of lightsheet fluorescence microscopy) but that can still lead to large multiplexing (>100 folds). In 2016, Zhang et al. [121] demonstrated that it is indeed possible to use a single VIPA to disperse the light spectrally in one direction while still retaining the spatial information in the other. However, their work was a proof of principle in non-biological

samples with low resolution and no sufficient suppression of elastically scattered light. To apply this approach for imaging living biological samples at a subcellular level, there are several issues to be addressed:

- The sample must be mounted in physiological conditions to keep it alive and enable to study of its development.
- The axial spatial resolution should be around $2\mu\text{m}$, i.e. the maximum achievable spatial resolution for the mechanical properties (see section 2.4). The FOV should be around $200\mu\text{m}$ to target developing embryos (see section 5.5).
- The wavelength needs to be chosen to reduce potential photodamage.
- The suppression of elastically scattered light needs to be better than 60dB.

To overcome all these challenges and enable to visualize mechanics in 3D and over time in sensitive, developing organisms, we engineered a new microscope (LSBM) which addresses these points, as described in the following sub-sections.

5.2.1 Physiological mounting of the sample

Regarding the physiological mounting of the sample, we employed an inverted SPIM configuration [122]. In our design two identical water immersion objectives (MRD07420, Nikon, 40x, 0.8NA) are mounted at 90° (figure 5.3) in a chamber containing the immersion liquid (figure 5.6a). The objectives have a working distance of 3.5mm, leaving sufficient space for mounting the sample. The sample is mounted on a chamber that can be scanned in 3D and it is separated from the immersion liquid by a Fluorinated Ethylene Propylene (FEP) foil (figure 5.3). FEP has a refractive index similar to water, thus reducing optical aberrations. The temperature and CO_2 in the environment close to the sample can be controlled (see section 5.3.1.1 for more details) to ensure physiological conditions.

5.2.2 Multiplexing with high spatial resolution

The objectives were chosen so that they can mechanically fit in the 90° configuration while still providing sufficient space for the sample and high resolution. Indeed their NA (0.8) provides a (theoretical) lateral resolution of

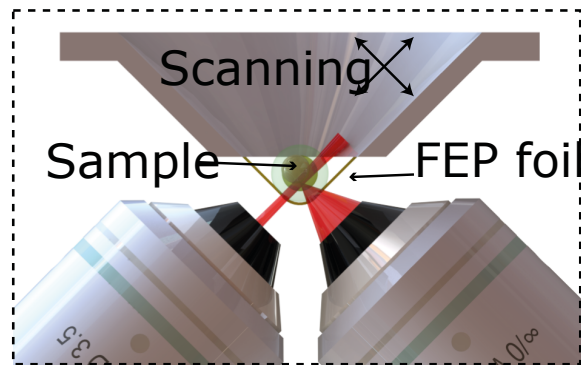


FIGURE 5.3: Schematic of the inverted SPIM configuration. Two identical water immersion objectives (0.8NA, 40x, WD=3.5mm) are used for illumination and detection respectively. The sample is mounted on a chamber that can be scanned in 3D and it is separated from the immersion liquid by a Fluorinated Ethylene Propylene (FEP) foil.

about $0.5\ \mu\text{m}$ (FWHM) and axial resolution of about $2.6\ \mu\text{m}$ (FWHM), that is consistent with the target resolution of $\lesssim 2\ \mu\text{m}$. The high NA poses additional challenges in the design of the spectrometer for multiplexing, that will be covered in section 5.3.3.

5.2.3 Reduction of the photodamage

The potential photodamage can further be reduced by moving the Brillouin laser towards longer wavelengths (IR); this comes at the cost of a lower signal (Brillouin cross-section is proportional to λ^{-4} , see section 2.1) but, at these wavelengths, the illumination energy can be increased while still retaining the photodamage advantage. In fact, Nikolić and Scarcelli [109] showed that cells are about 80 times less susceptible to laser light at 660 nm compared to 532 nm, while the Brillouin signal is only about 2.4 times lower, giving a speed advantage of 34x; at 780 nm we expect even lower photodamage because it is more towards the IR and the absorption coefficient of water is still $< 10\ \text{m}^{-1}$. The use of IR light has the additional advantage of not overlapping with excitation spectra of fluorophores commonly used in biology, thus leaving more freedom in the choice of the fluorescent labels and preventing photobleaching during Brillouin imaging.

5.2.4 Suppression of elastically scattered light

Biological samples have an heterogeneous distribution of refractive index that causes elastic scattering of the light. Even in transparent samples it can be much stronger than the Brillouin signal. Therefore, for the typical samples

we are interested in, a suppression of at least 60dB of the elastically scattered light is necessary. To that aim a good candidate for the laser wavelength is 780nm because it corresponds to one absorption line of atomic Rubidium (Rb). A glass cell containing Rb vapor can be used as a highly selective notch filter that absorbs the elastically scattered light while not affecting the Brillouin signal [30]. Such a filter can provide up to almost 80dB suppression of the elastically scattered light (see section 5.3.3.1 for more details). In order for the filter to work, the laser wavelength needs to match the peak absorption of Rb, within 0.1pm. That is achievable by using a tunable laser that is locked to the peak of absorption via a feedback loop.

5.2.5 Spectral purity of the laser

There are commercially available solutions that already implement the stabilization to an external gas cell but they are based on laser diodes that have high Amplified Spontaneous Emission (ASE). The ASE compromises the spectral purity of the laser and needs to be filtered not to overwhelm the weak Brillouin signal. That requires an additional custom build filter (detailed in section 5.3.2.1) which I designed and built.

5.2.6 Refractive index heterogeneity in the sample

Typically a (transparent) biological sample has a refractive index that is different from the surrounding medium and heterogeneous within the sample. Light is refracted every time it encounters an interface between different refractive indices and, in lightsheet fluorescence microscopy, this causes deterioration of the optical resolution due to displacement of the illumination sheet out of the focal plane of the detection objective [123]. In Brillouin microscopy, refraction affects also the measured Brillouin shift Ω . In fact, Ω depends on the angle between the illumination and detection direction – i.e. the scattering angle θ – (equation 2.3) and its value is different at each point of the sample due to refraction of both the illumination light and the detected signal (figure 5.4). Thus, the measured Ω contains information on both the speed of sound and the scattering angle θ , that can not be easily decoupled. A possible solution is to determine θ by simulating refraction on the measured 3D refractive index map of the sample. The refractive index in thin transparent samples can be measured using holographic techniques [124], while in thicker samples it can be inferred from multiple intensity images at the expense of a larger computational time [125]. These techniques need to

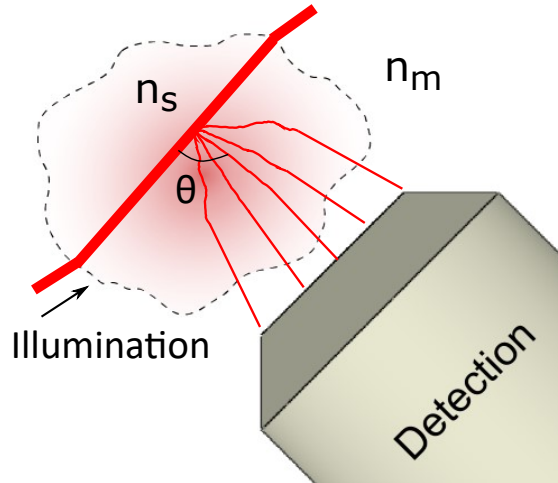


FIGURE 5.4: The difference in refractive index between the sample n_s and the surrounding medium n_m causes refraction of both the illumination and detected light, effectively changing the scattering angle θ .

be implemented on the same microscope used for Brillouin imaging because the alignment of the volumes measured in the two modalities is crucial for the correction to work. Therefore, this strategy would require major changes in the optical setup and data processing. We thus decided to leave this strategy for a future upgraded version of the microscope and we used a different strategy in the current version of the microscope that, despite some disadvantages, proved to be very effective. The strategy comes from the consideration that refraction does not produce a change in the scattering angle in the epidetection configuration. In fact, the detected signal follows the same optical path as the illumination light and, even if refraction may change its direction with respect to the optical axis, the angle between the two is always 180° . By placing a cylindrical lens before the objective, light can be focused on a line (lying in the focal plane of the objective, along the x direction in figure 5.5). We named this modality Epidetection Line-scanning Brillouin microscope (**E-LSBM**) in contrast with the Orthogonal Line-scanning Brillouin microscope (**O-LSBM**) (figure 5.5). E-LSBM has some disadvantages compared to O-LSBM, namely poorer z resolution (see section 5.3.3.2) and loss of the photodamage advantage due to the missing optical sectioning on the illumination but retains the speed improvement. The severity of refraction depends on the refractive index of the sample and its geometry: for some sample the O-LSBM modality can still provide reliable information without the need of correcting for refraction. Therefore, we designed the microscope so that the two modalities can easily be exchanged, depending on the sample.

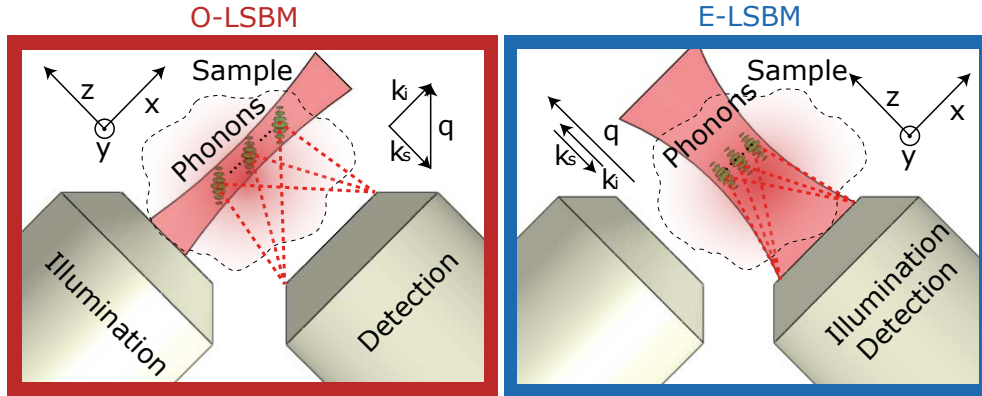


FIGURE 5.5: Comparison of orthogonal (O-LSBM) and epiline (E-LSBM) line-scanning Brillouin microscope modalities. In O-LSBM the illumination (k_i) and detection (k_s) directions form an angle of 90° while in E-LSBM they are parallel. Red color is used in all the subsequent figures when referring to the O-LSBM modality while blue for the E-LSBM modality. Figure adapted from [65].

5.3 Setup description and characterisation

5.3.1 Microscope body

Figure 5.6 shows a rendering of the microscope body that was designed by Ling Wang using SolidWorks and the mechanical parts were produced by the EMBL mechanical workshop. The whole microscope body is built on a single vertical metal plate to increase mechanical stability. Each objective is fixed in the immersion chamber by means of a conical ring at the bottom of the chamber. By design, the optical axis of one objective lies on the focal plane of the other to within $100\mu\text{m}$ and the fine adjustment of the focus is done optically (see section 5.3.2). The light is delivered/collected through two holes at the back of the plate. Two mirrors redirect light so that a horizontal beam perpendicular to the plate is aligned with the optical axis of the objectives after reflection. A single mirror could be used instead but in that case the image of the line formed after the objective would not be parallel or perpendicular to the optical table, making the alignment of the spectrometer more challenging.

The sample is mounted in a separate chamber, fixed to 3 one-axis translational stages (SLC-2430, SmarAct) that can move it over 16mm in all directions with a resolution of 50nm. The movement axes of the translational stages are aligned to the x , y and z axes in figure 5.5 to provide intuitive scanning of the sample with respect to the optical axis of the detection objective.

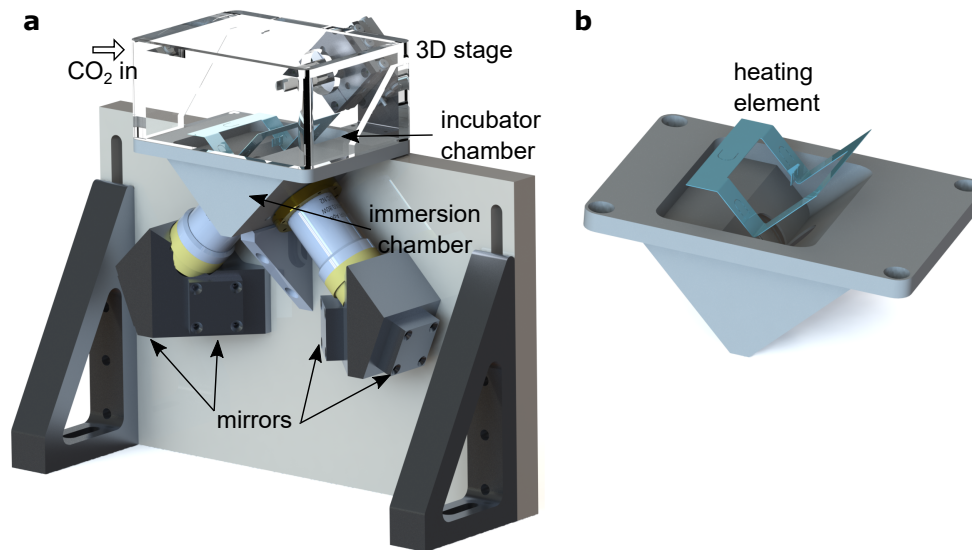


FIGURE 5.6: a) Mechanical design of the microscope body. The light is delivered to each objective by means of two mirrors that rotate the image of the line so that it is vertical with respect to the optical table. The objectives are mounted in an immersion chamber filled with water. The sample is mounted in a separate chamber (not shown in the figure) that is connected to a 3D stage for scanning the sample. A 3D printed plastic cover forms the incubation chamber for environmental control. b) zoom in on the immersion chamber, containing the heating element for temperature control. Figure adapted from [65].

5.3.1.1 Environment control

Inside the immersion chamber, there is a metal foil on which a temperature sensor and some resistors are mounted. They are connected to a temperature controller that can keep the temperature to a specific value via a feedback loop. The immersion chamber is covered with a 3D-printed plastic housing. A hole on the side of the chamber allows a premixed gas to be injected inside. The gas is prepared by a custom-built mixer that can mix compressed air with CO₂ from the pipes system at EMBL in a settable ratio. The temperature control and gas mixer were built by Christian Kieser from the EMBL electronic workshop. I calibrated the gas mixer by temporarily inserting a CO₂ sensor in the chamber and adjusting the ratio so that the CO₂ concentration inside the chamber is 5%.

5.3.2 Brillouin illumination and detection

The following text is adapted from the method section of Bevilacqua et al. [65] and it was written by myself. Figure 5.7 shows an optical schematic of

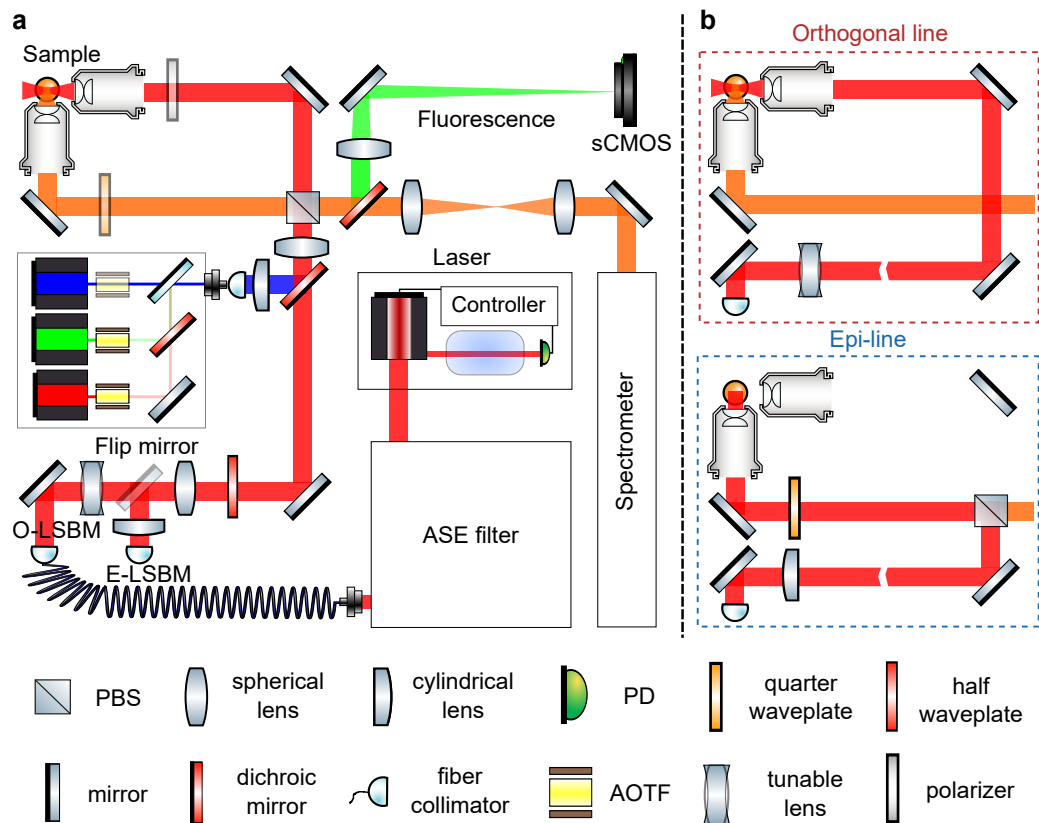


FIGURE 5.7: Optical schematic of the LSBM microscope. Figure adapted from [65].

the microscope. The laser is an amplified tunable diode laser (TA pro, Topica) locked to the D₂, F=2 absorption line of Rb^{87} (780.24nm). This allows a Rb cell to be used as an ultra-narrowband notch filter (section 5.3.3.1). To further clean up the laser's spectrum from ASE noise, we designed a custom-built narrowband double-pass optical filter (see section 5.3.2.1). After the filter, the light is coupled into a polarization-maintaining (PM) fiber and delivered to the main microscope. Here, a collimator (LPC-OT-780-5/125-P-3-16AC-40-3A, OZ Optics) produces a collimated beam with a diameter of 2.77mm ($1/e^2$, theoretical), that corresponds to a focused beam of $1.79\mu\text{m}$ ($1/e^2$, theoretical) after the objective. The beam then passes through an electrically tunable lens (ETL) (EL-10-30, Optotune) coupled with a negative offset lens (LC1258-B, Thorlabs). This allows axial scanning of the focus position after the objective (see section 5.3.2.2). After the tunable lens, a flip mirror allows to switch between the epi-line and orthogonal-line illumination: the separate optical path for the epi-line illumination consists of a $f=40\text{mm}$ lens (LA1422-B, Thorlabs), that collimates the light out of a PM fiber (P3-780PM-FC-2, Thorlabs), providing a beam of diameter 8.7mm ($1/e^2$, theoretical) (filling the back focal aperture of the objective, which is 8mm); a $f=200\text{mm}$ cylindrical lens (LJ1653RM-B, Thorlabs) generates the focused line in the focal

plane of the objective with an extension of about $185\mu\text{m}$ ($1/e^2$) (see section 5.3.2.3). A half waveplate (WPH05M-780, Thorlabs) is used to rotate the linear polarization of the illumination light to match the required direction for the two geometries. Two mirrors, conjugated to the back and the front focal plane of the objective (by means of two 200m lenses: #33-362 and #49-364, Edmund), respectively, allow for fine position and angle adjustment of the beam inside the sample in order to aid in the alignment between the illumination and detection objectives. For the epi-line Brillouin geometry (E-LSBM), a polarizing beam splitter (PBS) (BPB-12.7SF2-R400-800, Lambda), mounted on a magnetic base for switching between the two modalities, followed by quarter waveplate (WPRM-25.4-12.7CQ-M-4-780, Lambda) reflects the light towards one of the two objectives; the Brillouin signal is collected by the same objective and transmitted by the PBS towards the spectrometer (the polarization is rotated by 90° due to double pass at the quarter waveplate). A polariser is added before the other objective (used for SPIM excitation, details in section 5.3.4) which is required to block the backward-scattered un-polarised fluorescence light that would otherwise be reflected by the PBS and generate a bright line at the center on the FOV of the SPIM camera.

5.3.2.1 ASE filter

The detection of Brillouin signal from biological samples poses very strict requirements on the spectral purity of the laser. In fact, one needs to detect a signal that can be 6 orders of magnitude (60dB) weaker than the scattered laser light and very close in wavelength (about 10pm). As already mentioned in section 5.2, the laser's spectrum shows a floor (that is about 50dB below the laser intensity) due to Amplified Spontaneous Emission (ASE). It might seem that 50dB is not far from the required purity of 60dB but one needs to consider that the ASE extends over several nm, while the FSR of the spectrometer is around 30pm. Therefore the total ASE is effectively integrated, leading to a much larger background within the measurement range. To reduce the background to a level that would allow imaging of biological samples, I built a filter, whose optical schematic is shown in figure 5.8a. The filter contains a holographic diffraction grating (NoiseBlock, Coherent) that is specifically designed to filter ASE in Raman spectroscopy. Unfortunately, its bandwidth is around 0.5nm, still much larger than the separation between the Brillouin signal and the laser (0.01nm). An additional piezo-tunable Fabry-Perot (FP) (FSR 15GHz, Finesse ~ 60 , LightMachinery) further suppresses the ASE within a bandwidth of about 0.5pm. The FSR of the FP is matching

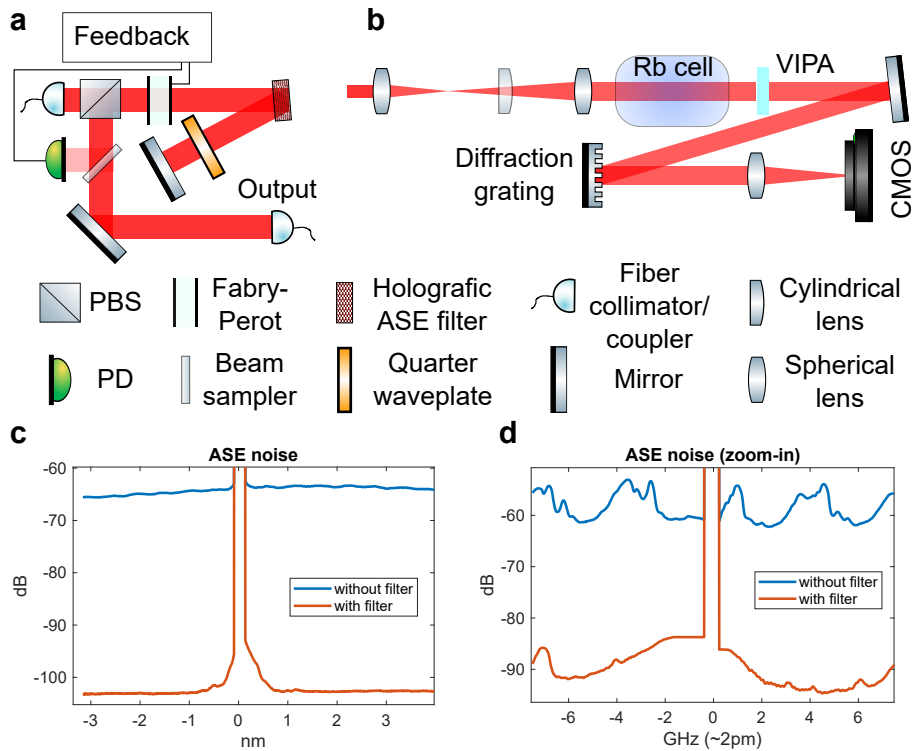


FIGURE 5.8: Characterisation and filtering of Amplified Spontaneous Emission (ASE) (a) Optical layout of the double-pass ASE filter employed. To stabilize the Fabry-Perot (FP) based filter over a long time a feedback loop is realized via a photodiode, custom-written Arduino software and piezo that adjusts the FP mirror spacing. (b) Optical setup used to measure the ASE (c,d) Plots of ASE spectrum with and without filter few nm (c) and few GHz (d) away from the laser line. The filter suppresses the total ASE (integrated over the whole measured range) by more than 40dB. Figure taken from [65].

the FSR of the spectrometer: in this way the residual ASE, transmitted by higher orders of the FP, will be mapped in the same position as the laser by the spectrometer, not overlapping with the Brillouin signal. To further improve its suppression, the filter is designed in a double pass configuration: the polarisation of the input light is adjusted to be transmitted by a Polarising Beam Splitter (PBS), it then goes through the FP and is diffracted by the holographic grating. The diffracted light goes through a quarter waveplate and it is back-reflected by a mirror. After the quarter waveplate, the polarisation is orthogonal with respect to the original one, thus the light is reflected by the PBS, after traveling the inverse optical path through the holographic grating and the FP. The orthogonal polarisation also ensures that there is no interaction between the light propagating in opposite directions inside the FP. After the PBS a beam sampler reflects 5% of the light to a photodiode. The signal of the photodiode is fed into an Arduino board. The Arduino board can output a voltage to control the FP mirror spacing through a piezo. A self-written code maximizes the intensity detected by the photodiode to correct for long term drift of the FP cavity with respect to the laser wavelength.

5.8b shows the setup that I built to measure the suppression of the ASE: the combination of a VIPA and diffraction grating allows to measure the spectrum over several nm (figure 5.8c), while still having a sub-GHz resolution (figure 5.8d). A Rb cell absorbs the intense laser light (see section 5.3.3.1 for more details) and makes it possible to achieve the required dynamic range. The measurement shows a suppression of the ASE in spectral region relevant for Brillouin imaging (-6GHz to 6 GHz) down to about **-90dB** with respect to the laser line.

5.3.2.2 Maximizing axial resolution in O-LSBM

It is well known that in optics there is a trade-off between the spot size and depth of field: one needs to increase the NA to reduce the spot size (proportional to NA^{-1}) but increasing the NA largely decreases the depth of field (proportional to NA^{-2}). In the O-LSBM configuration, the illumination line needs to have an extension of about 200 μ m and a thickness of about 1.5 μ m but this is not possible to achieve with a static beam (figure 5.9a-b). This limitation can be overcome by scanning a tightly focused Gaussian beam (figure 5.9c-d). A tunable lens achieves this by generating a diverging (converging) beam before the objective that causes the focus spot to move far from (towards) the objective. The tunable lens should be placed in a plane conjugated to the back focal aperture (BFA) of the objective to minimize clipping

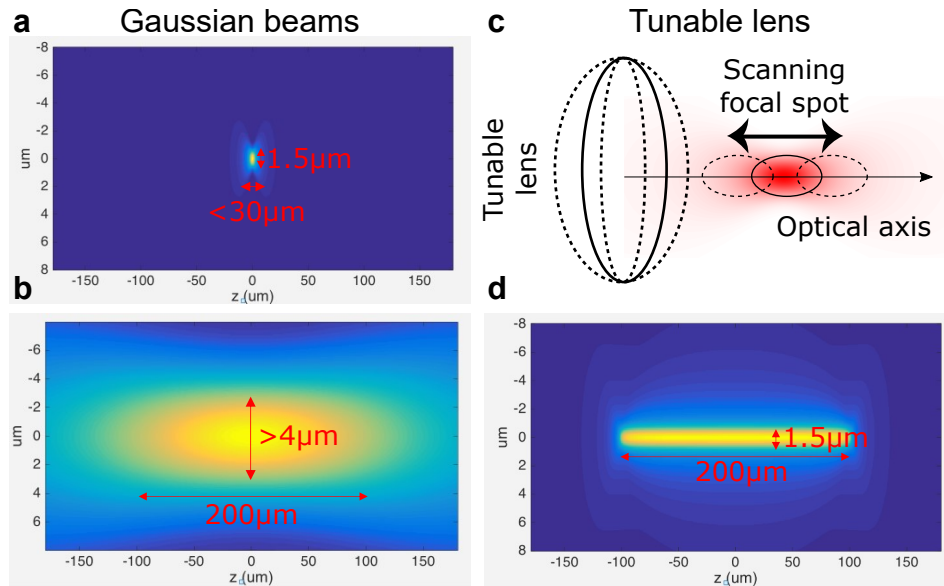


FIGURE 5.9: Principle of the tunable lens to extend the depth of field of the illumination line to $200\mu\text{m}$ while retaining a thickness of $1.5\mu\text{m}$. In the case of Gaussian beams, the depth of field is less than $30\mu\text{m}$ when the thickness is $1.5\mu\text{m}$ (a); conversely, when extending the depth of field to $200\mu\text{m}$ the thickness is more than $4\mu\text{m}$ (b). The tunable lens allows scanning a tightly focused Gaussian beam (c), thus effectively extending the depth of field (d).

of the beam when it diverges. In our case, the actual conjugated plane is not accessible because it is occupied by the mirror used for alignment (see section 5.3.2). Thus, I placed the tunable lens as close as possible to the mirror (which I estimated to be about 20mm apart due to the 45° angle of the mirror). The focal length of the electrically tunable lens (ETL) (EL-10-30 from Optotune) can vary from 45mm to 120mm . Contrary to TAG lenses, ETLs always have a positive focal length (converging lens) and a negative offset lens needs to be added to create an alternatively diverging and converging beam. I used Zemax to estimate the ideal focal length for the negative offset lens in order to obtain the desired scanning range of $\pm 100\mu\text{m}$. I found that, between the commercially available negative lenses, a focal length of -75mm (LC1258-B, Thorlabs) was the optimal.

The ETL is controlled by current (up to 200mA) that can not be directly provided by a DAQ. Therefore, Alejandro Gil Ortiz from the EMBL electronic workshop built a voltage-to-current converter. I calibrated the ETL by measuring the displacement of the focus spot (visualized by imaging the fluorescence signal from an ICG die in water.) when varying the voltage applied to the controller of the ETL (figure 5.10). I measured the zero displacement by determining the voltage that would produce a collimated beam (2V) with the help of a shearing interferometer.

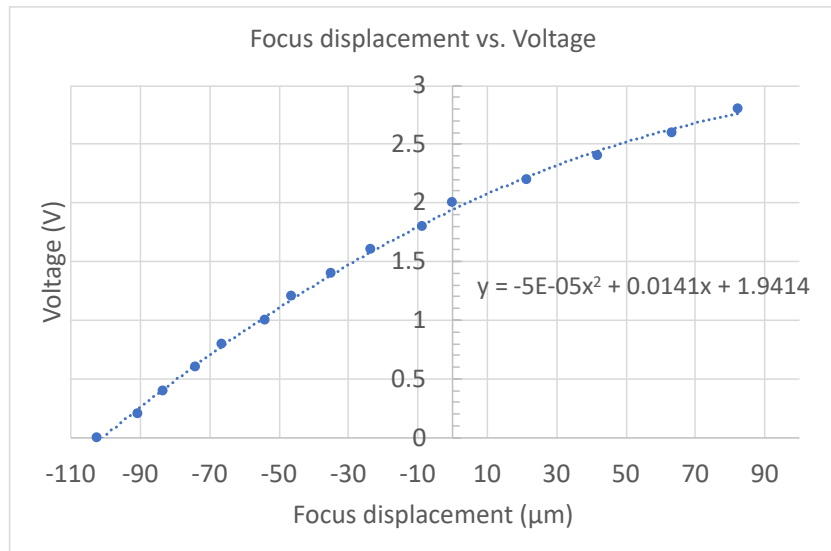


FIGURE 5.10: Calibration curve of the ETL determined by measuring the displacement of the focus spot (visualised by imaging the fluorescence signal from a ICG die in water.) when varying the voltage applied to the controller of the ETL.

Since the ETL is relative slow (the step response from 10% to 90% requires 2.5ms) it is not possible to scan the focal spot much faster than the camera exposure time (100ms), so that the camera always "sees" an average of the intensity along the whole scanning range, independently of the phase of the scan. Instead, the ETL needs to be synchronized so that one full scan of the focus is done in a single camera acquisition. To that aim, I used the fire output of the camera (high when the camera is exposing) to trigger a DAQ (PCI-6221, National Instruments). In response to the trigger, the DAQ outputs a waveform of the same duration as the camera exposure and with the shape given in figure 5.10; the extension of the scan, in μm , can be changed depending on the sample.

5.3.2.3 Field of view

As mentioned in section 5.2 our target FOV is $200\mu\text{m}$, that covers the extension of the model organisms we are interested in studying. The FOV is determined both by the detection optics (that in our case is the Brillouin spectrometer, detailed in section 5.3.3) and by the illumination. In the O-LSBM configuration the extension of the illumination is determined by the scanning range of the focus spot; figure 5.11a shows the longest illumination profile used in the acquisition of a biological sample. In the E-LSBM the extension of the illumination profile is determined by the focal length of the cylindrical lens before the objective (see section 5.3.2) and it is quantified in figure

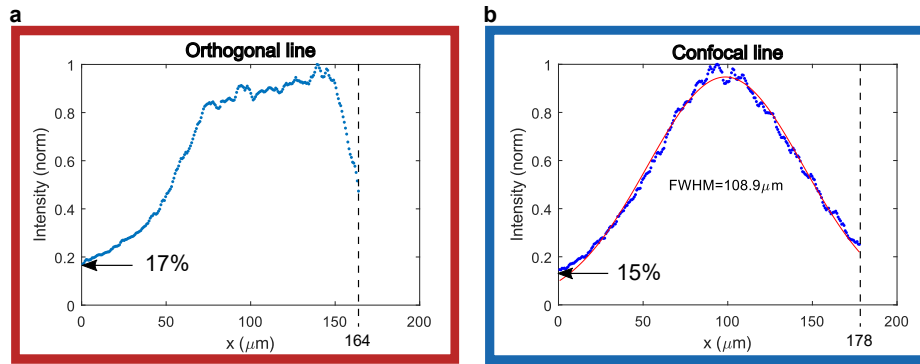


FIGURE 5.11: Illumination profile along the FOV (measured as the intensity of the Stokes/anti-Stokes spectral peaks in water) for the (a) epi line and (b) orthogonal line geometries, respectively. Note that a relative intensity value of $>15\%$ is generally sufficient for reliable Brillouin peak fitting/detection. Figure adapted from [65].

5.11b. Both illumination profiles are determined by measuring the intensity of the Brillouin peaks in water². Note that 15% of the maximum intensity is still sufficient for reliable Brillouin peak fitting/detection. In fact, differently from lightsheet fluorescence microscopy where a gradient in the illumination intensity causes a gradient in the measured signal, in Brillouin microscopy a reduced illumination intensity causes only a decrease in the fitting precision (more noisy images); in shot noise limited conditions (that is the case for our spectrometer, as shown in section 5.3.3.3) a relative intensity of 0.15 causes a precision that is $1/\sqrt{0.15} \approx 2.6$ times worst.

5.3.3 LSBM spectrometer

The spectrometer is the key optical part of the LSBM determining both the spectral and the spatial performance of the microscope. As demonstrated by Zhang et al. [121], multiplexing can be achieved by having the VIPA conjugated to the back focal aperture (BFA) of the objective in the direction parallel to the illumination line (x -axis in figure 5.12): light originating from different points along the line impinges on the VIPA under different angles; a lens after the VIPA remaps these different angles to their corresponding spatial positions. Two drawbacks arise from the need of entering the VIPA at an angle: the optical path inside the VIPA is different for each angle (generating a curved interference pattern, see figure 5.14a) and the beam undergoes a lateral walk-off at each reflection and might be clipped after some reflections

²This measurement is affected by potential spatial-dependent losses of the spectrometer, so it is not an accurate measurement of the illumination profile. But the overall signal at the output of the spectrometer is the quantity of interest for our purposes.

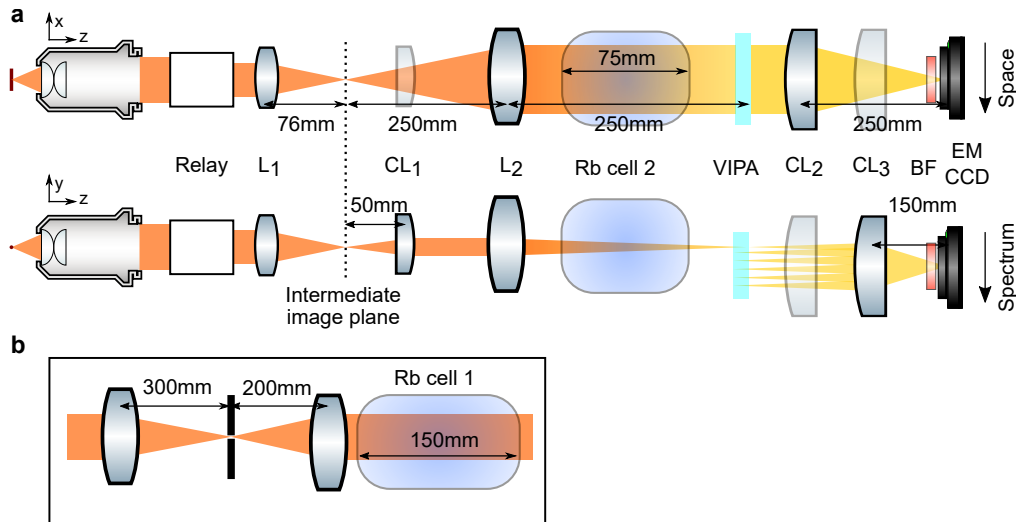


FIGURE 5.12: Optical design of the LSBM spectrometer (a) Orthogonal views of the optical components in the LSBM spectrometer with relevant distances; top shows the plane determined by the illumination line and the optical axis of the detection objective, where the BFA of the objective is relayed and appropriately magnified by the optics to the VIPA plane; bottom shows the plane perpendicular to the illumination line, where the image plane is appropriately magnified and relayed by the optics to the VIPA plane. (b) Details of the relay shown in panel a. Figure adapted from [65].

(higher losses and lower finesse for the points at the edge of the FOV). To mitigate these effects, the angles need to be kept small and this makes the optical design more challenging when having high magnification (40x) and a large FOV (200 μm). Furthermore, there are also constraints on the focusing angle on the VIPA (along the y-axis in figure 5.12) because that determines the distribution of the light among the different interference orders (intensity envelope in figure 5.14b). Ideally, if only a single order is used for determining the Brillouin shift, the intensity envelope should extend over a single order to achieve the best efficiency. We took a different approach, and average the light from different orders to recover the SNR (see section 5.4 for details).

Figure 5.12 shows the optical schematic of the LSBM spectrometer. The role of the optics before the VIPA is to relay and expand the BFA of the objective in the x direction while focusing the light on the VIPA in the y direction. At the BFA the beam is 8mm and the angles corresponding to a FOV of 200 μm are $\pm 0.02\text{rad}$. First, due to the mechanical and optical components before the spectrometer, the first position where a lens can be placed is about 300mm from the BFA. Therefore, I used a 300mm plano-convex lens (LA1256-B, Thorlabs) followed by a 200mm plano-convex lens (LA1979-B-ML, Thorlabs) to relay the BFA. An adjustable slit (VA100/M, Thorlabs) in the focal

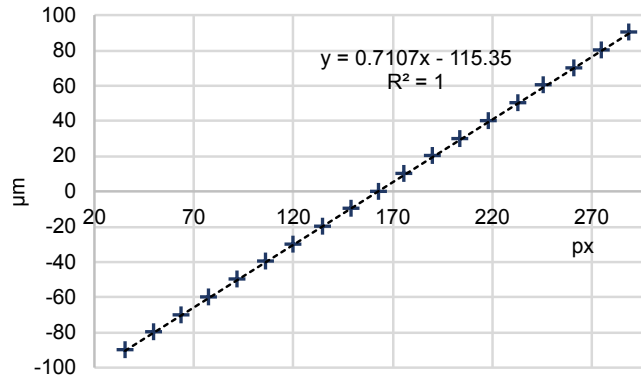


FIGURE 5.13: Spatial calibration (μm to pixel) acquired by translating a bead, with steps of $10\ \mu\text{m}$, along the x direction and determining its position on the camera. Figure adapted from [65].

plane of the first lens ensures confocality in the direction perpendicular to the illumination line. After the relay, the beam has a diameter of 5.3mm and the angles are $\pm 0.03\text{rad}$. I will now describe separately the role of the optics along the spatial direction (x) and the ones along the spectral direction (y). In the spatial direction (x) an achromatic lens L_1 ($f=76.2\text{mm}$, #49-794, Edmund) and a plano-convex lens L_2 ($f=250\text{mm}$, #69-513, Edmund) relay the BFA to the plane where the VIPA (OP-6721-6743-9, LightMachinery) is: there the beam has a diameter of 17.5mm (matching the clear aperture of the VIPA of 18mm) and the angles are $\pm 0.009\text{rad}$ (corresponding to a maximum walk-off of $\approx 80\ \mu\text{m}$ at each reflection). After the VIPA a cylindrical lens CL_2 ($f=250\text{mm}$, LJ1267L1-B, Thorlabs) focuses light on an EM-CCD camera (iXon DU-897U-CS0-BV, Andor), providing a sampling of about $0.7\ \mu\text{m}/\text{px}$ (figure 5.13). In the spectral (y) direction L_1 and the cylindrical lens CL_1 ($f=50\text{mm}$, #36-231, Edmund) reduce the beam to a diameter of 3.5mm ; L_2 focuses it on the entrance slit of the VIPA with a semi-angle of 0.007rad . After the VIPA the cylindrical lens CL_3 ($f=150\text{mm}$, LJ1629L2-B, Thorlabs) focuses the light on the camera with a spectral sampling of ≈ 0.25 to $\approx 0.5\ \text{GHz}/\text{px}$. A bandpass filter centered at 780nm (FBH780-10, Thorlabs) blocks the ambient light.

Figure 5.14 shows the spectrum of a mixture of water with intralipid (to make the Rayleigh peak visible). The multiple interference orders are clearly visible and the intensity envelope is marked with a dotted line in the line profile in panel b.

To facilitate the alignment, I built the spectrometer on an optical rail. I adjusted the height and the z position of the optics with the aid of a beam at the

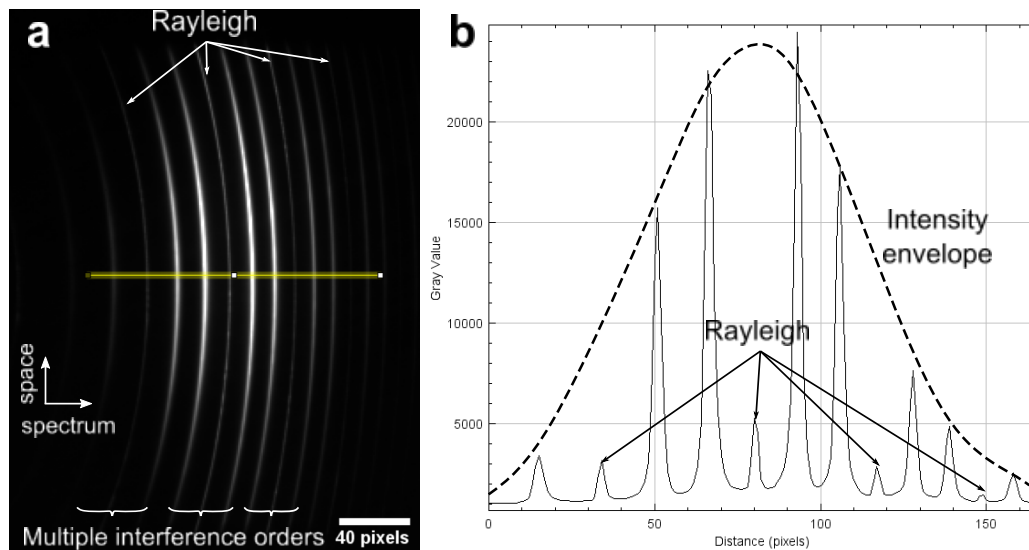


FIGURE 5.14: Raw spectrum from an intralipid solution in water. a) Raw image from the camera in the spectrometer. Note that the pattern is curved and multiple interference orders can be observed. b) Line profile of the yellow line highlighted in a. The dashed line indicates the intensity envelope covering multiple interference orders.

same height as the beam after the objectives (100mm). The collimated beam was produced by a fiber collimator mounted on a rail carrier. I aligned the relays by checking the collimation after them with a shearing interferometer. I mounted the cylindrical lenses on rotational mounts because their alignment to the entrance window of the VIPA is critical.

5.3.3.1 Rb cell for background suppression

As mentioned in section 5.3.2, a glass cell filled with Rubidium can be used as an ultra-narrowband filter to suppress the elastically scattered light, while leaving the Brillouin signal almost unaffected. Indeed, the vapor inside the cell is mainly composed of atomic Rb, whose absorption linewidth is very narrow, approximately 500MHz, limited only by Doppler broadening³. When looking closer at the Doppler-broadened D2 line of natural Rubidium, centered at 780.24nm, one can see that it is formed by 4 lines (figure 5.15). These are two doublets, each of which from the two isotopes (Rb^{85} and Rb^{87}) that constitute natural Rubidium in a ratio 2.6:1; the doublet is due to the hyperfine splitting of the atomic line. The laser can be locked to any of the lines but one needs to choose carefully in order to avoid that other lines overlap with

³The linewidth is proportional to \sqrt{T} , where T is the temperature in K. The difference in linewidth between room temperature and 80C (the maximum temperature we heat the Rb cell up to) is less than 10%.

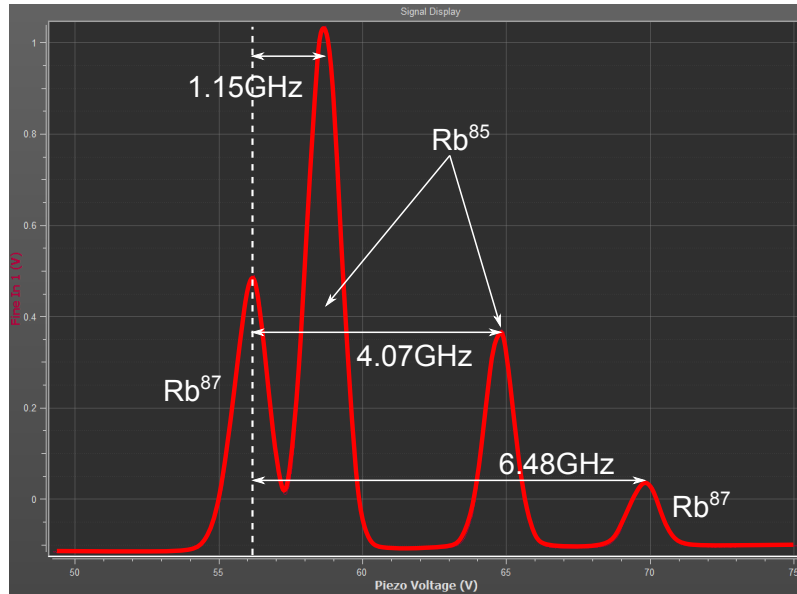


FIGURE 5.15: Hyperfine structure of the D2 line of Rb, acquired with the CoSy unit of the Toptica laser (by measuring the absorption of a Rb cell while scanning the laser wavelength). Note that natural Rubidium is composed by a mixture of Rb^{85} and Rb^{87} , each of which has two absorption lines. The frequency shift between the different lines was determined by Fan Yang by measuring, with a frequency counter, the beating of two lasers, tuned to different absorption peaks.

the Brillouin signal. Glass cells filled with pure Rb^{85} or Rb^{87} are commercially available; the spectrum of such a cell would have only two absorption lines. Rb^{85} has a distance between the lines of 2.92GHz which, especially in the O-LSBM configuration, could overlap with the Brillouin signal, thus partially absorbing it. In Rb^{87} , the distance is 6.48GHz, which is larger than any expected Brillouin signal from biological samples and therefore the best choice for our application was Rb^{87} . Nevertheless, in case of overlap, only the Stokes (or anti-Stokes) peak is affected, thus it would still be possible to determine the Brillouin shift by looking at a single peak.

The absorption of the cell depends exponentially on its length. Therefore, in order to increase the suppression of the elastically scattered light, we used two gas cells: a 150mm-long (SC-RB87-(25x150-474 Q)-AR, Photonics Technologies) and a 75mm-long Rb^{87} cell (SC-RB87-480 (25x75-Q)-AR, Photonics Technologies). We could not use a single, longer cell, since cells longer than 150mm are not commercially available, due to regulations on dangerous goods. Additionally, using two shorter cells is also advantageous since it is easier to fit them in-between the optics in the spectrometer (figure 5.12). The absorption of each cell also depends on the density of the Rb vapor, which can be tuned with temperature. In fact its internal pressure corresponds to

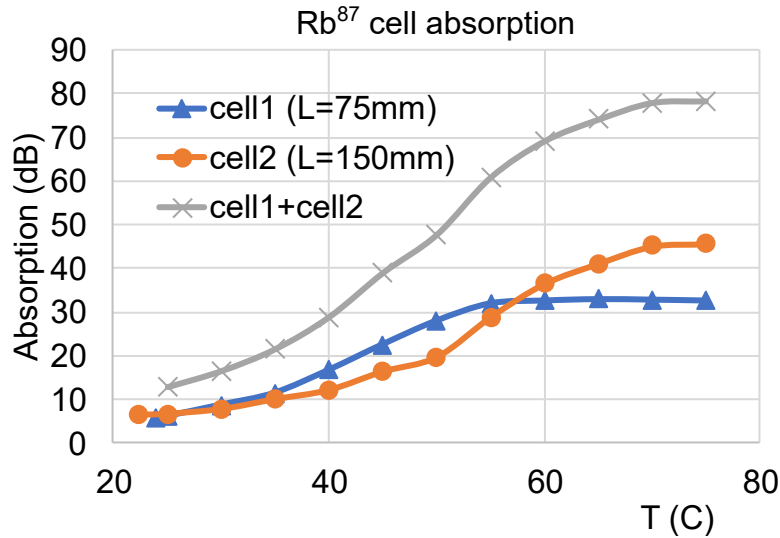


FIGURE 5.16: Absorption of the laser light from a 150mm long (orange line) and 75mm long (blue line) cell filled with pure Rb^{87} as a function of temperature. Figure adapted from [65].

the vapor pressure of Rb at a given temperature. Higher temperatures correspond to higher vapor pressures (assuming there is enough solid Rb in the cell to vaporize), thus higher densities. Figure 5.16 shows the measured absorption of the two cells as a function of temperature. To heat up the cells I used several heating foils (2 for the 75mm-long cell and 3 for the 150mm-long cell) with an integrated thermistor (HT10K, Thorlabs). I designed, together with Christian Kieser, a custom board (fitting on an Arduino Mega) to power and read the temperature from the heating foils. I wrote the Arduino code that maintains the cell at a settable temperature via PID. To prevent condensation of the Rb on the optical windows when the cells cool down, I placed the heating foils close to the windows and set the temperature of the heating foil in the middle (for the 150mm-long cell) 5C lower than the ones close to the window. In this way, the colder spot, where condensation happens, is always in the middle of the cell.

5.3.3.2 Spatial resolution

In the confocal Brillouin microscope, I quantified the spatial resolution by imaging a sharp transition between two materials that have a high acoustic mismatch, that is an approximation of the optical resolution (see section 4.2.1.1). In the line-scanning Brillouin microscope the Rayleigh light can be detected, thus it can be used to measure the true optical resolution. To quantify it, I embedded $0.5\mu\text{m}$ beads (Tetraspeck, Thermo Fischer) in 0.5% agarose and mounted them in the sample chamber of the LSBM. I located a bead in

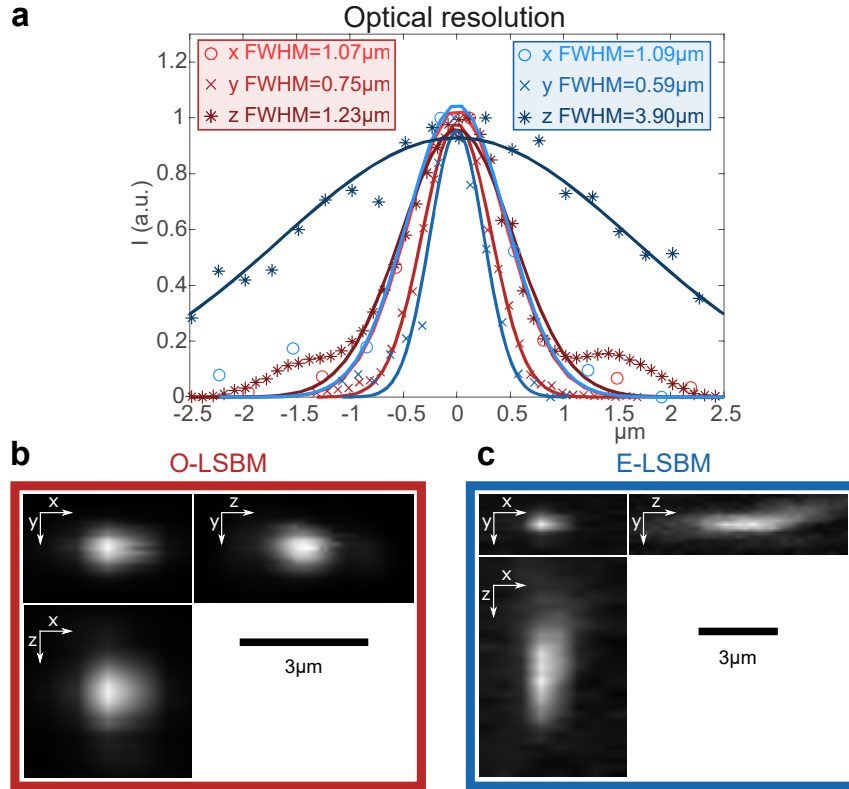


FIGURE 5.17: Optical resolution quantified from the elastically scattered light from a 0.5 μm bead (a); The red data points refer to the orthogonal geometry while the blue ones to the epi geometry. Orthogonal views of the same beads used to generate panel a in the O-LSBM (b) and E-LSBM (c). The convention for the axes is the same as in figure 5.5. Figure adapted from [65].

the fluorescence channel⁴ (section 5.3.4) and adjusted the laser intensity and exposure time of the camera so that the light elastically scattered from the bead is clearly visible in the Brillouin spectrum. I scanned the sample in the y and z direction (with reference to the axes in figure 5.5), while, in the x direction, I used the calibrated pixel size (0.7 μm , figure 5.13). To reconstruct the image of the beads, I looked at the intensity of the Rayleigh light and generated the data in figure 5.17. Note that, while the x and y resolutions are similar in the two geometries, the z resolution is significantly worse in the E-LSBM due to the missing optical sectioning on the illumination.

5.3.3.3 Spectral precision

To determine the spectral precision, I used the same method as the one in section 4.2.2.1, consisting on measuring multiple times the Brillouin spectrum of water and calculating the standard deviation. As it can be seen in figure 5.18a

⁴I used the bead also to align the Brillouin and fluorescence modalities.

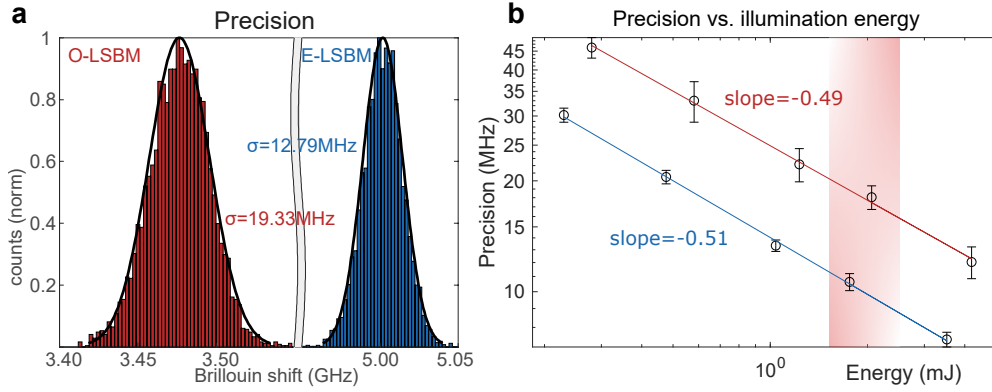


FIGURE 5.18: Spectral precision. Panel a shows a histogram of multiple measurements of the Brillouin shift of water in the O-LSBM (red) or E-LSBM (blue) configuration in typical imaging conditions (100ms exposure ≈ 20 mW. The distributions are fitted to a Gaussian (dark solid line) and their standard deviations (that represent the spectral precision) is written next to them. Note that the average value is different in the two configurations due to the $\sin(\theta)$ dependence of the Brillouin shift (equation 2.3). Panel b shows the spectral precision (standard deviation of multiple measurements) under different illumination energies in the two configurations (red=O-LSBM, blue=E-LSBM). The shaded red region indicates typical imaging conditions. The data is fitted to a line in a log plot and slope ≈ 0.5 indicates a square root dependence, typical of shot noise limited conditions. Figure adapted from [65].

the distribution is Gaussian and its standard deviation is 19.33 MHz for O-LSBM and 12.79 MHz for E-LSBM. The lower precision in the O-LSBM is due to the larger linewidth [34] and reduced geometrical efficiency [121] in the 90° scattering geometry. Panel b shows the spectral precision under different illumination energies in the O-LSBM and E-LSBM configurations. The slope ≈ 0.5 in a logarithmic plot indicates a square root dependence, as expected in shot noise limited conditions.

5.3.3.4 Spectral accuracy

The Rb cell provides also a method to calibrate the spectrometer. In fact the relative position of the absorption peaks is known (figure 5.15) and the laser can be locked to each of the peaks (figure 5.19a). The reconstruction pipeline (detailed in section 5.4) allows to determine the absolute value of the frequency from the raw spectra, once the FSR is known (figure 5.19b). I determined the FSR to be 15.15GHz (15GHz in the specs of the VIPA) by minimizing the sum of the distances between the measured and the known frequency of the Rb absorption lines. The distance is measured as the average absolute discrepancy along all the spatial points in a spectrum (L1 norm).

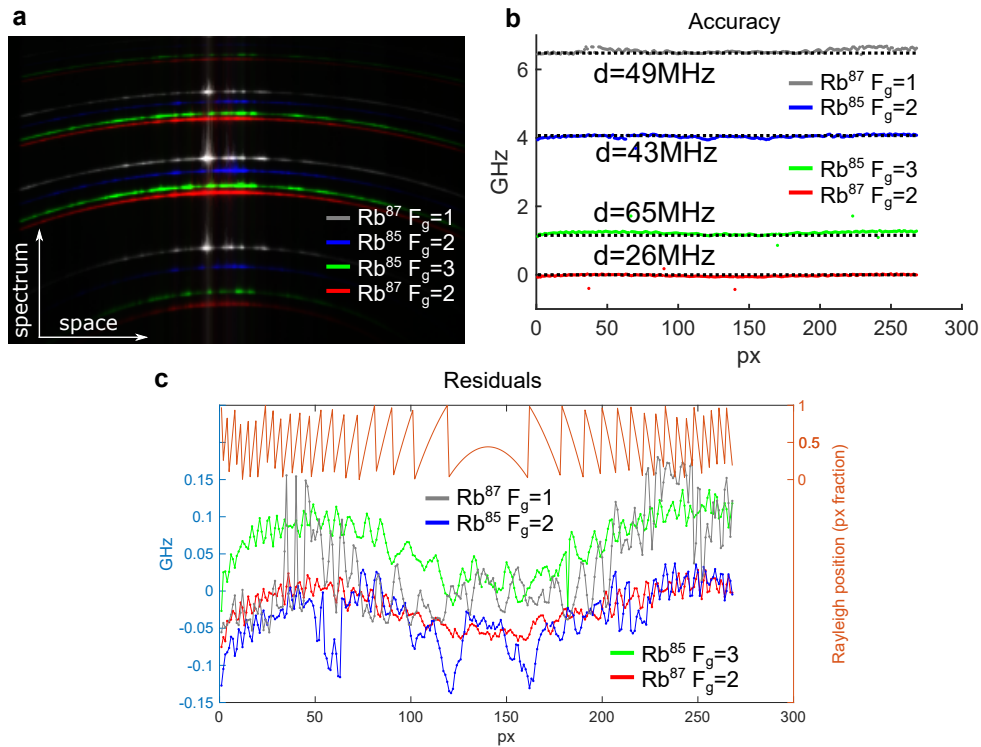


FIGURE 5.19: (a) Acquired, raw spectra of the 4 hyperfine D2 spectral lines of Rb^{85} and Rb^{87} as measured by the spectrometer. (b) Frequency shift of the Rb lines in panel a after applying the reconstruction pipeline (see section 5.4); dotted lines represent the exact values (figure 5.15); d is the L1 distance between the measured and the exact values divided by the number of points i.e. the average discrepancy from the true frequency; the FSR is measured to be 15.15GHz by minimizing the sum of d for the 4 Rb lines. (c) left axis: Residuals (i.e. difference between the measured and the known value) of the data in panel b; right axis: position of the Rayleigh peak from the $\text{Rb}^{87} F=2$ line (used as the 'zero') from one order, relative to the previous pixel. Figure adapted from [65].

Note that the distance is on the orders of tens of MHz, larger than the spectral precision (section 5.3.3.3), thus noticeable in an image. We attribute this effect to re-sampling artifacts introduced in the reconstruction pipeline when remapping the spectrum from a non-linear sampling (due to the VIPA dispersion, see appendix A.1) to an equispaced sampling (more details in section 5.4). In fact, due to the curvature of the interference pattern (figure 5.14), the spectrum of each spatial point is shifted on the camera plane and it is thus sampled differently. This effect could explain the pattern observed in the residuals (figure 5.19c): the period of the "oscillations" would correspond to a shift of exactly one pixel, thus the period would be larger close to the center (where the interference pattern is better aligned to a column of pixels on the camera). Indeed the same change in period is observed when plotting the position of the Rayleigh peak from the Rb⁸⁷ F=2 line (used as the 'zero') from one order, relative to the previous pixel (shown in figure 5.19c, on a different y axis). Note that its pattern is not expected to correspond perfectly to the data converted to GHz, because the reconstruction takes into account Rayleigh peaks from at least 3 orders and the re-sampling artifacts should depend also on the position of the Stokes (and anti-Stokes) peaks relative to a pixel, nevertheless its similarity is an indication of the validity of our interpretation. This issue could potentially be mitigated by increasing the spectral sampling (i.e. changing the lens CL_3 in figure 5.12 to a longer focal length), with the drawback of getting poorer spectral precision. We did not follow that path because accuracy (i.e. getting the exact value in GHz of the Brillouin shift) is less important than precision (i.e. the 'noise' on the Brillouin images) when looking at relative changes in time, or space, in biological samples.

5.3.3.5 Spectral resolution

Similarly to the confocal Brillouin microscope (section 4.2.2.2), I measured the spectral resolution by looking at the laser spectrum through the LSBM spectrometer. I applied the reconstruction pipeline (detailed in section 5.4) and generated the plot shown in figure 5.20. By fitting a Lorentzian curve, I determined the FWHM to be **0.51GHz**, corresponding to a finesse of approximately 30 (FSR=15GHz). This is lower than the nominal value specified by the manufacturer (70) and the discrepancy could be attributed to aberrations of the optics before the VIPA. In fact, typically, a single lens is used to focus the light on the VIPA after a single mode fiber, which produces a clean Gaussian beam profile. In our setup instead, there is a combination of several

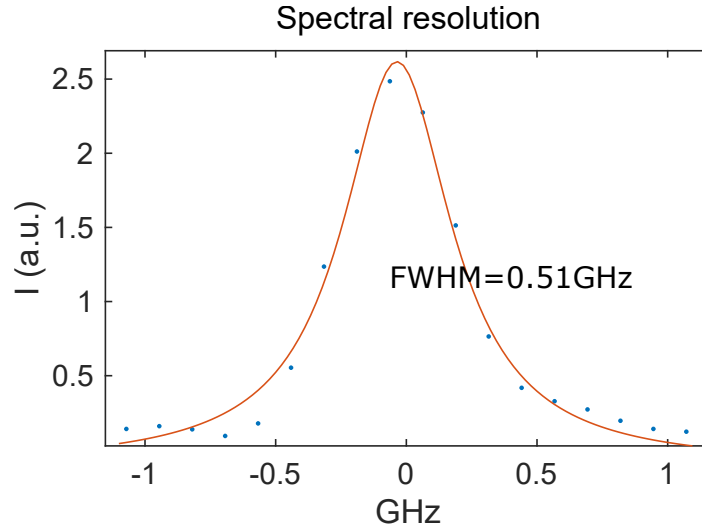


FIGURE 5.20: Spectral resolution of the spectrometer, as measured by the FWHM of the laser line, after applying the reconstruction pipeline (section 5.4). Figure adapted from [65].

spherical and cylindrical lenses relaying the light to the VIPA and the beam profile is only partially spatially filtered (there is a confocal slit instead of a pinhole). Since the VIPA is based on the interference of multiple reflections, wavefront aberrations can significantly impact its performance [126].

5.3.4 Lightsheet fluorescence modality of the LSBM

The following text is adapted from the method section of Bevilacqua et al. [65] and it was written by myself.

The optical schematic of the fluorescence SPIM modality is shown in figure 5.7. We utilized a laser box providing several laser lines for fluorescence excitation (405nm, 488nm, 560nm, 640nm). The fluorescence excitation is introduced into the setup by a single mode fiber (P1-460Y-FC-1, Thorlabs) whose output is collimated by an achromatic lens ($f=4\text{mm}$), producing a $\approx 0.8\text{mm}$ ($1/e^2$, theoretical) beam. A fiber polarisation controller (FPC030, Thorlabs) is used to adjust the polarization and a polariser rejects potential residual non-linear polarisation. The excitation light is then coupled into the same optical path as the Brillouin illumination by means of a dichroic mirror (FF765-Di01, Semrock). Similarly to the Brillouin illumination path, two lenses (#67-159, Edmund and #49-364, Edmund, shared with the Brillouin path) and mirrors (not shown in figure 5.7) allow for beam adjustment. A 18mm cylindrical lens (#68-041, Edmund) is used in order to generate the light sheet. The corresponding thickness and lateral extent of the light sheet inside the sample are $\approx 4\mu\text{m}$ and $\approx 200\mu\text{m}$ ($1/e^2$, theoretical), respectively.

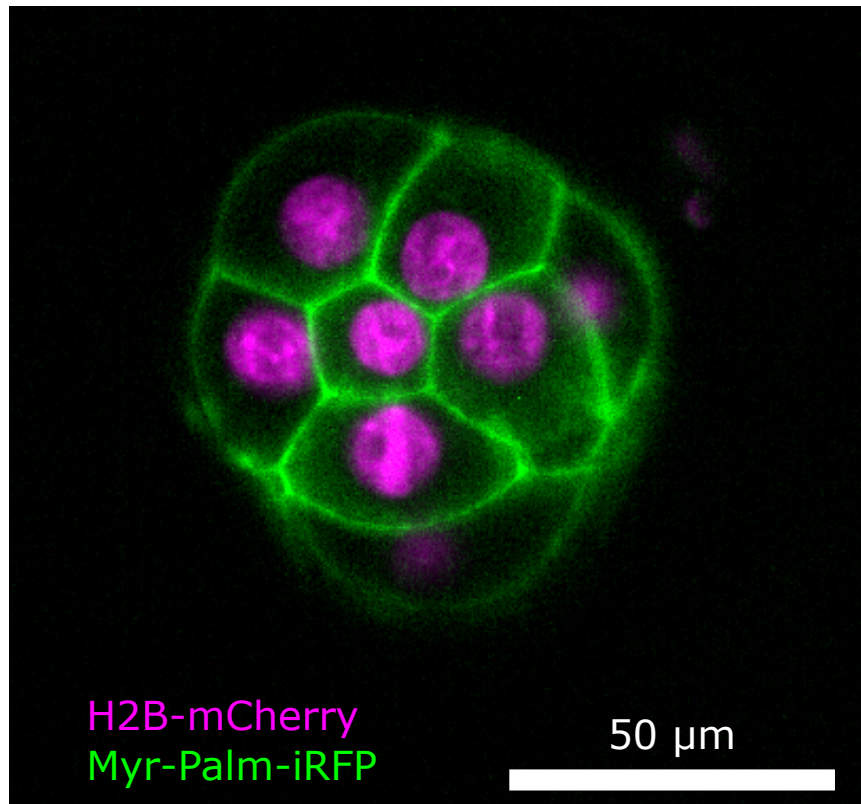


FIGURE 5.21: Example image of a multicolor SPIM image of a mouse embryo where both membranes and nuclei are fluorescently labelled.

The fluorescence and Brillouin signals are split via a dichroic mirror (FF765-Di01, Semrock), reflecting the fluorescence emission. A tube lens (MXA20696, Nikon) focuses the fluorescence image on the SPIM camera (Zyla sCMOS, Andor); a motorized filter wheel (96A361, Ludl) allows for the selection of the proper emission filter. Figure 5.21 shows an example image acquired with the SPIM setup.

5.3.5 Graphical User Interface

I designed and programmed the Graphical User interface for the LSBM to facilitate the selection of the ROI (that is most of the times a 3D volume) and the acquisition of timelapses of multiple samples in an automatic fashion (named Sequential acquisition). The main window of the LabVIEW program is divided in 3 tabs: Fluorescence (figure 5.22), Brillouin (figure 5.23) and Sequential acquisition (figure 5.24).

The "Fluorescence" tab displays the frames continuously acquired by the SPIM camera (see section 5.3.4) and allows to select between imaging a specific fluorophore (selection of both the excitation laser and emission filter) or

brightfield (the light is produced by a small white LED placed in the housing of the incubator). The ROI can be selected by changing the x , y and z parameters in the box in the right bottom corner in figure 5.22. The size of the ROI in the focal plane of the detection objective (x,z axes) can be evaluated directly from the image. Instead, the "depth" (y axis) is determined by moving the sample by a known step (controlled by the slider above the green arrows) and identifying the top and bottom planes that contain the interesting region; for that fluorescence imaging (not brightfield) should be used, if possible, because it is not affected by out of focus light, which makes it hard to precisely determine the plane of interest. Once the ROI is set, the current sample can be added to the list of samples to be imaged by pushing the button "Add current position".

The "Brillouin" tab displays the signal acquired by the Brillouin spectrometer in real time, so that signal strength and quality can be checked and the optical power and exposure time can be adjusted accordingly.

The "Sequential acquisition" tab shows the list of samples included in the current sequential acquisition (left table in figure 5.24). Different modalities (Fluorescence, Brightfield and Brillouin) with different acquisition parameters (exposure time, EM gain, fluorophore) and different timing (period between subsequent acquisitions, maximum number of repetitions and delay of the first acquisition after the start of the imaging session) can be added to the right table. Each of them is automatically assigned an index, which univocally identifies them. The assignment of specific modalities (right table) to the samples (left table) is done by inputting the corresponding indices in the "Acq" column. The modalities and samples are automatically color-coded to help visually identify the matching between the two.

5.4 Processing of raw spectra

In the LSBM spectrometer, multiple interference orders are visible and they can be used to calibrate the spectrometer. As explained in appendix A.1, the interference orders m of the Rayleigh peaks is a function of a second order polynomial of their position on the camera. Therefore, when at least three orders are visible, the non-linear dispersion relationship of the VIPA can be determined and used to remap the spectra onto a linear space. The non-linear dispersion needs to be determined independently for each spectrum in a single acquisition (rows in figure 5.14a) and the position of the Rayleigh peaks needs to be known very precisely for accurate results. To that aim, I

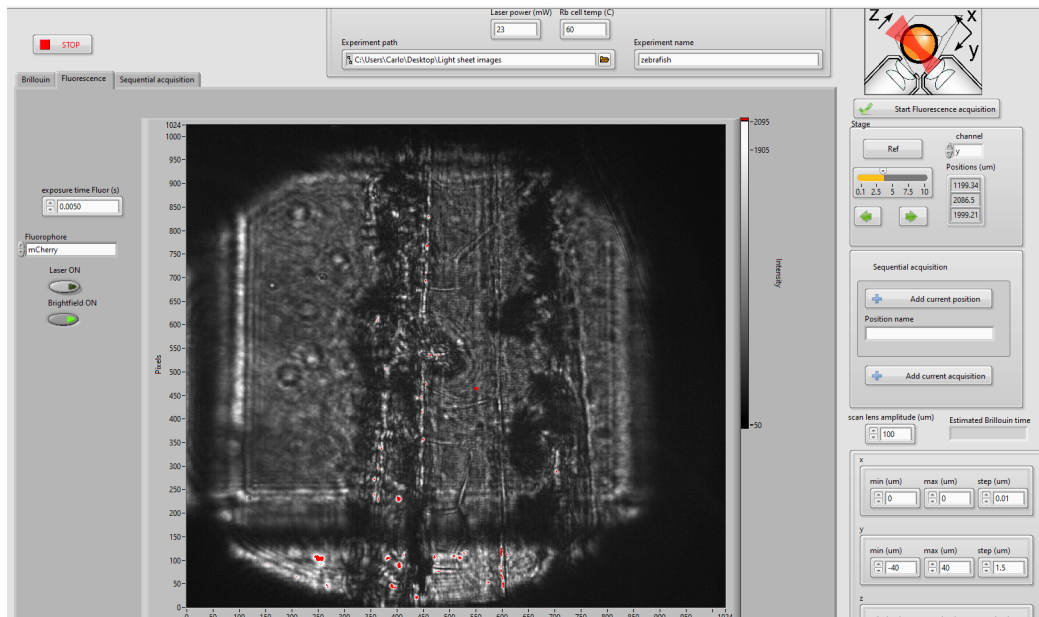


FIGURE 5.22: The "Fluorescence" tab in the LabVIEW program is used to see fluorescence (or brightfield) images from the sample in real time and determine to ROI.

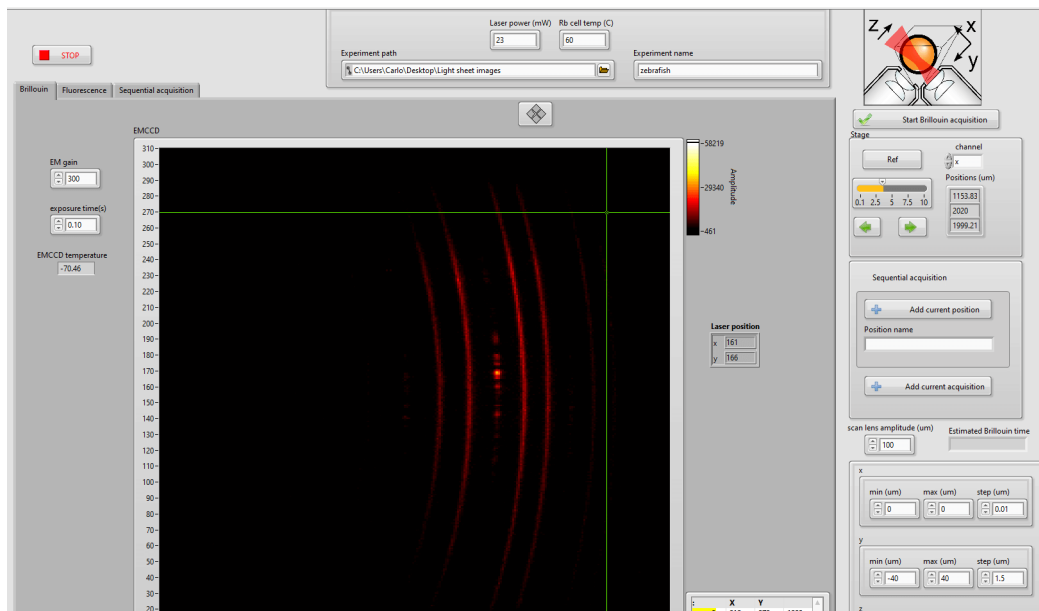


FIGURE 5.23: The "Brillouin" tab in the LabVIEW program is used to see the signal from the Brillouin spectrometer in real time and determine signal strength and quality.

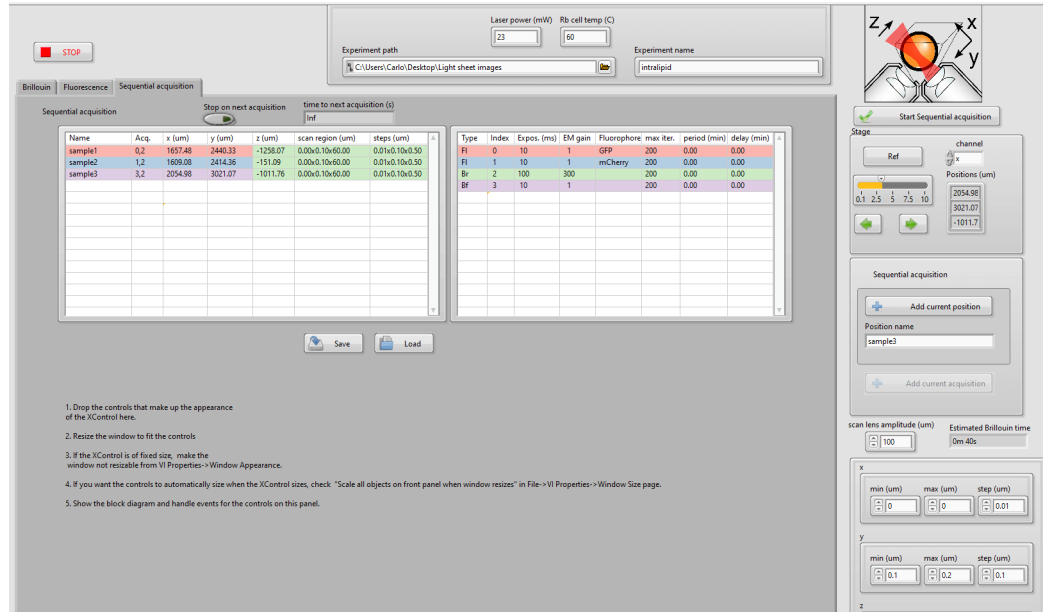


FIGURE 5.24: The "Sequential acquisition" tab in the LabVIEW program controls the assignment of different acquisition modalities (right table) to each sample (left table). Colors help to visually identifying the matching between the two.

derived that the Rayleigh peaks of each order lie on an ellipse (see appendix A.3) and I wrote a Matlab script that allows the user to manually select some points on the Rayleigh lines and fit an ellipse to each of them. From the fitted ellipses, the position of the Rayleigh peaks for each row can be determined. Then each row is processed separately following three main steps:

1. the spectrum is remapped to a linear frequency space and re-sampled (by using spline interpolation) so that the samples are equispaced in frequency. The conversion from pixels to GHz is done by knowing that subsequent orders are spaced by one FSR;
2. the different orders are summed together to increase the SNR (effectively recovering the lost SNR due to the light spreading over several orders);
3. an appropriate function is fitted to the Stokes and anti-Stokes peaks to determine their position.

Regarding the last point, in the E-LSBM configuration, the Brillouin peaks can be fitted by a Lorentzian function, but in the O-LSBM configuration the effect of asymmetric broadening due to high NA is quite pronounced and a Lorentzian lineshape is not appropriate [34]. Unfortunately, there is no analytical solution to the integral that describes the lineshape [34] and we decided to implement it numerically. A big disadvantage is the increase of

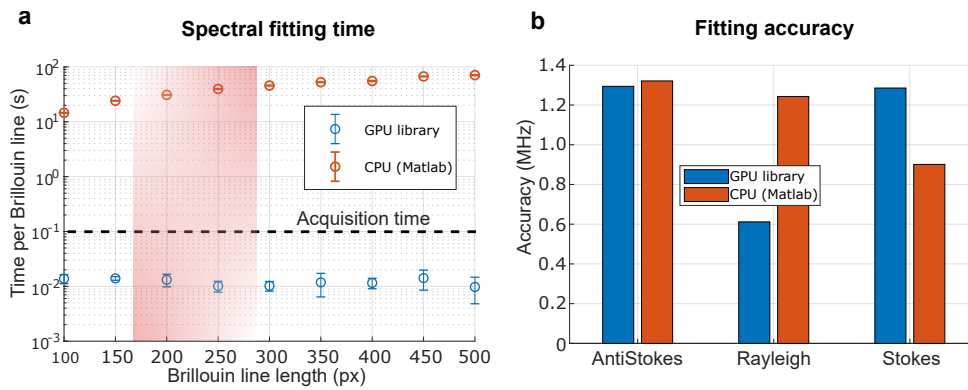


FIGURE 5.25: Performance of the GPU-accelerated spectral analysis pipeline. (a) Brillouin spectrum fitting time as a function of image size (equal to the number of independent spectra), comparing standard, CPU-based fitting routines (Matlab) and our custom GPU-accelerated library. Total analysis time is generally >1000 -fold improved with GPU acceleration, making the processing time smaller than the acquisition time. The shaded red region shows the typical length of the Brillouin line in pixels. Note most error bars are smaller than data points. (b) Fitting accuracy between the CPU- and GPU-based pipelines, showing comparable performance. Note that the accuracy uncertainty (1MHz) is negligible compared to the spectral fitting precision based on realistic, noisy data (10-20MHz). The plots were generated by Sebastian Hambura. Figure taken from [65].

the computational cost for each fit, that, together with the fact that for each camera acquisition hundreds of spectra need to be processed, made the processing time (10s) much longer than the acquisition time (0.1s). However, since each line can be processed independently, the whole pipeline can be implemented on a GPU. The GPU implementation drastically reduces the processing time per camera image (bringing it below the acquisition time of 100ms) while not affecting the fitting accuracy (figure 5.25). The CUDA code was written by Sebastian Hambura and it is available on GitHub: <https://github.com/prevedel-lab/brillouin-gpu-acceleration>.

5.5 Biological demonstrations

To demonstrate the capabilities of the LSBM to image fast processes, large volumes and photosensitive samples with subcellular resolution over time, we imaged several model organisms. I will present the results in the next sections.

5.5.1 *Drosophila* gastrulation

Drosophila melanogaster is a widely used model organism in biology. Gastrulation is an extensively studied process in *Drosophila* [127], that comprises rapid (on the minute timescale) cell rearrangement and cell shape changes. It is thus an interesting process from a mechanical point of view and Brillouin microscopy has the unique advantage of providing 3D mechanical information from deep tissue. In particular, we looked at two different folding events, namely ventral furrow formation (VVF) and posterior midgut invagination (PMG). They are both driven by the same cytoskeletal machinery (actomyosin) but the shape of the contractile domain is different. Both processes are quite fast, lasting about 20 minutes, thus fast acquisition is a strict requirement.

The sample preparation and mounting was done by Juan Manuel Gomez. To ensure proper orientation of the embryo with respect to the objective⁵, he glued the embryos on the FEP foil (with Heptane-glue) and oriented them under a stereoscope. The embryos were glued on the outside of the sample chamber (glued area on the opposite side of the embryo compared to the one imaged) to avoid any possible interference of the gluing process with the morphogenetic event under investigation. In this condition, the sample is directly immersed in the chamber containing the objectives, that was thus filled with a buffer solution (PBS), necessary for proper embryo development.

Figure 5.26a-b illustrates the process of VVF: cells with the mesodermal fate, identified by the expression of the transcription factor Snail (in green), change their shape and position and will eventually invaginate. When we looked at this process in the E-LSBM, together with SPIM imaging of membranes (Gap43-mCherry) (figure 5.26c), we observed a transient increase of the Brillouin shifts of the tissue close to the ventral furrow. By looking at the membrane signal, Juan identified and manually segmented the presumable mesodermal cells (by taking 9 cells on the left and on the right of the center of the furrow and back-tracking them for timepoints where the furrow is not visible) and plotted their average Brillouin shift over time (figure 5.26d); by performing a paired-one-way ANOVA test ($F=44.29$, $p=0.066$), followed by a post-hoc multiple comparison test, he confirmed that there is indeed a statistically significant increase of their Brillouin shift, consistently in 3 different

⁵At this developmental stage, the *Drosophila* embryo is filled with yolk that is quite scattering and has a very different refractive index compared with the surrounding tissue. The embryo must thus be oriented so that the tissue of interest is facing the objective, in order to avoid strong optical aberrations when imaging through the yolk.

embryos.

We then looked at PMG (figure 5.27a) to investigate whether the increase in Brillouin shift is a common feature of invagination events driven by actomyosin, independently of the geometry of the contractile domain. Indeed we observed a transient increase of Brillouin shift in the area close to the invaginating tissue (figure 5.27b), consistently in 3 different embryos.

To understand whether the observed change in mechanical properties is driven by the actomyosin network, future experiments could be performed: firstly one could correlate the myosin levels (having it labeled in a separate fluorescence channel) with the Brillouin shift or perform perturbation experiments with drugs that affect myosin activity or actin polymerisation; finally one could look at folding events that are driven by a different molecular mechanism (e.g. dorsal folds).

To conclude, I want to highlight that the fast acquisition of a spacial resolved Brillouin map was fundamental to determining the transient increase in Brillouin shift: a spatial or temporal average would wash out the interesting dynamics. Also, despite the continuous acquisition of the same volume in the sample, no photodamage was observed and all the imaged embryos progressed to the first larval stage (24hpf).

5.5.2 Phallusia

Phallusia mammillata is a marine tunicate of the ascidian class. Phallusia embryos exhibit a very stereotypical development and they are highly transparent, making them ideal for microscopy. Recently the full single cell transcriptome up to gastrulation was analyzed and made publicly available [128], opening the intriguing possibility of correlating the mechanical properties of individual cells with their gene expression.

We imaged whole embryos (about 180 μ m in diameter), at different stages from 1-cell to 64-cell stage. Ulla-Maj Fiuza was responsible for the sample preparation and biological interpretation of the results. We utilized the OLSBM modality because the high transparency of the sample guarantees reduced artifacts. When looking at the 16-cell stage (figure 5.28a-c), we observed a region with high Brillouin shift localised next to the nucleus of B5.2 cells (figure 5.28e-f). We interpreted it as a dense microtubule bundle, that is known to be present in the B5.2 cells [129]. In fact, the B5.2 cells, progenitors of the germline cells, undergo an asymmetric division and the nucleus is kept to one side of the cell by the microtubule bundle (figure 5.28d). In this case,

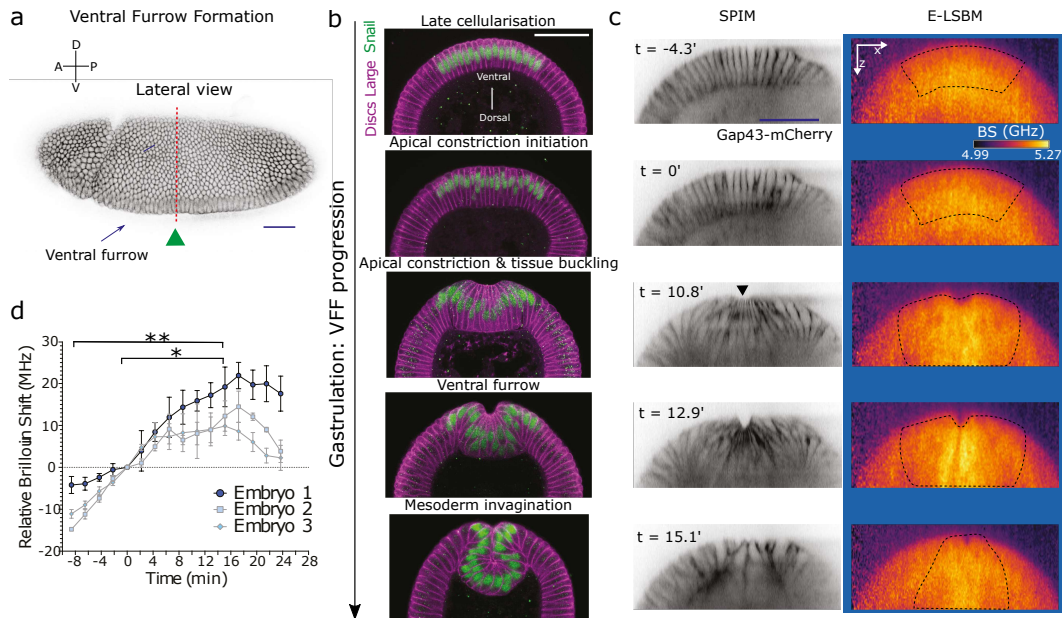


FIGURE 5.26: (a) Superficial view of a fixed *Drosophila* embryo undergoing ventral furrow formation (VFF, arrow). The embryo expresses the membrane marker Gap43-mCherry to visualize cell outlines. The green arrowhead indicates the direction of Brillouin illumination which here is orthogonal to the apical surface of cells. Red segmented line indicates the approximate location of physical cross-sections shown in b and c. (b) Stages of VFF progression shown in physical cross-sections of fixed embryos, stained with a Snail antibody (green) to label the nuclei of cells engaged in VFF and a Discs Large antibody (magenta) to label cell outlines. (c) left: Images from a SPIM recording of an embryo expressing Gap43-mCherry to mark cell membranes; right: median-projected Brillouin shift maps from the same embryo at the same timepoints and positions as shown above (representative embryo of $n = 3$ total). The imaged volume is $22 \times 170 \times 71 \mu\text{m}$ (z -increment of $1.5 \mu\text{m}$) with a time resolution of about 2min. The dotted line encloses the presumable mesoderm region within the Brillouin shift maps used for quantification in d. The apical side of cells faces the outer surface of the embryo. (d) Quantification of Brillouin shift averaged over 18 cells engaged in apical constriction and invagination during VFF progression, as inferred from SPIM slices (dotted line in c). Changes in Brillouin shift are shown relative to the Brillouin shift at time-point $0'$, which corresponds to the initiation of apical constriction. Data points are average Brillouin shift within the contractile domain, error bars denote S.D. over different slices. Statistical significance was evaluated using a paired-one-way ANOVA test ($F = 44.29$, $p = 0.066$), followed by a post-hoc multiple comparison test (FDR corrected, $\alpha = 0.05$, $q\text{-value} = 0.1$); * $p = 0.039$, ** $p = 0.0054$. Timescale is minutes. Scale bars are $50 \mu\text{m}$. Figure adapted from [65] and made by Juan Manuel Gomez.

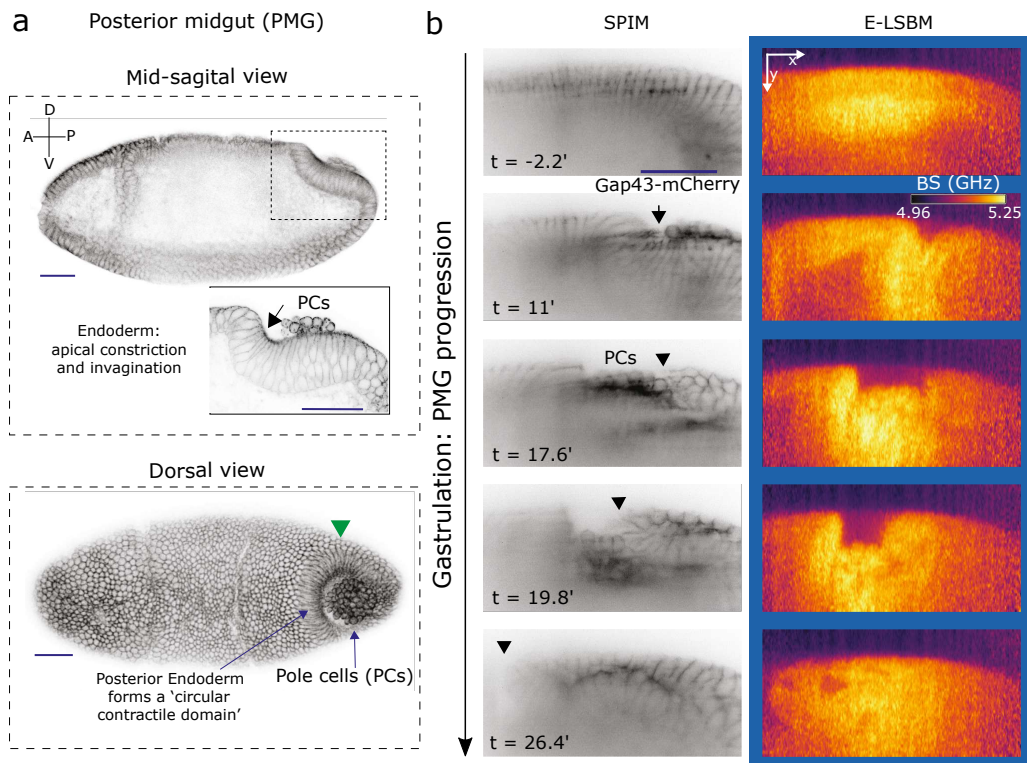


FIGURE 5.27: (a) Posterior midgut invagination (PMG) in embryos at a similar stage as in figure 5.26. (Top) mid-sagittal section; inset: higher magnification of the posterior midgut region showing apical constriction and invagination during PMG formation; (bottom) superficial-dorsal view a *Drosophila* embryo showing the formation of the circular contractile domain of the PMG that encloses the Pole Cells (PCs, arrow). The embryo expresses the membrane marker Gap43-mCherry to visualize cell outlines. The green arrowhead indicates the direction of Brillouin illumination which here is orthogonal to the lateral surface of cells. (b) Representative SPIM images (left) and median-projected Brillouin shift maps (right) at five timepoints during invagination (out of $n = 3$ total). The imaged volume is $83 \times 141 \times 46 \mu\text{m}$ (z-increment of $2.5 \mu\text{m}$) with a time resolution of about 2min. Arrowhead indicates the displacement of the posterior end during PMG invagination. The initiation of apical constriction was set as $0'$ time point. Images in Gap43-mCherry and Brillouin panels are median projections of 3 slices of the re-sliced ROI. Timescale is minutes. Scale bars are $50 \mu\text{m}$. Figure adapted from [65] and made by Juan Manuel Gomez.

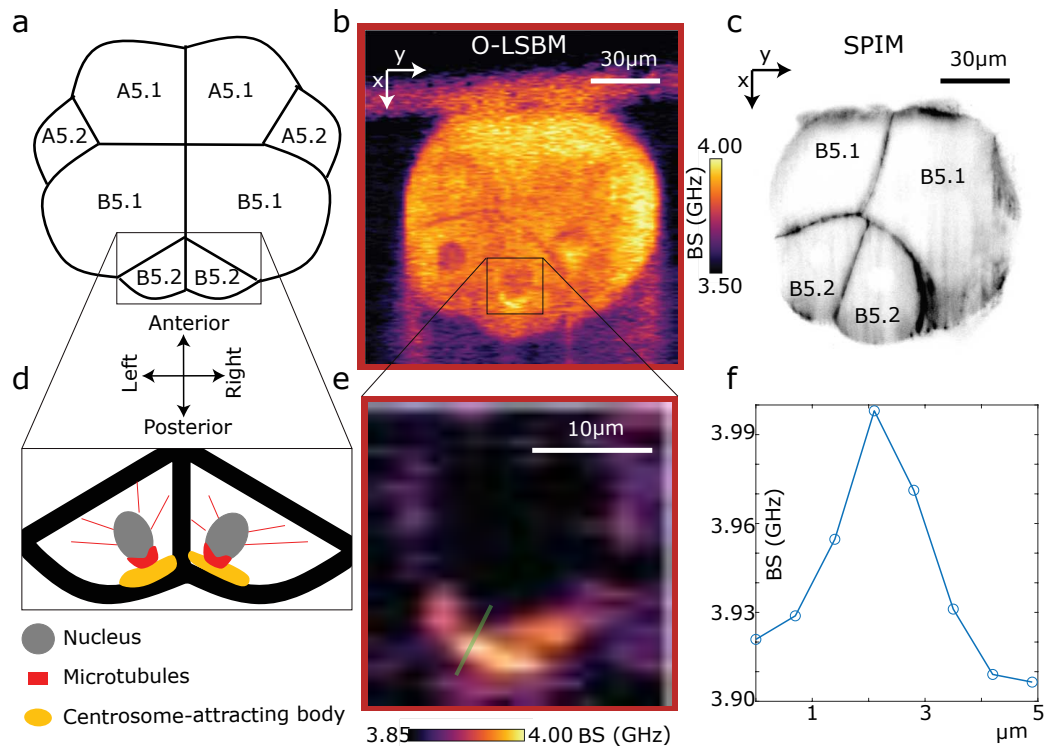


FIGURE 5.28: Schematic of the vegetal hemisphere of a late 16 cells stage *Phalusia* embryo (a), showing the bilateral symmetry. Exemplary O-LSBM image (b) and corresponding SPIM image (c) (membranes labeled with lipophilic dye FM4-64) of the same stage as shown in a (out of $n = 2$ total). The imaged volume is $165 \times 186 \times 172 \mu\text{m}$ (z-increment of $2.5 \mu\text{m}$) within a time of about 17 min. Cartoon of the machinery for asymmetric division in two B5.2 germline progenitor cells (d): a thick microtubules bundle directed to the centrosome-attracting body forms on the posterior side of the nucleus. Zoom-in of the gray square in panel b (e) showing a high Brillouin shift in the vicinity of the nucleus that is indicative of a microtubule bundle. Line profile along the line shown in panel e (f). BS, Brillouin shift. Figure adapted from [65].

the LSBM allowed us to image the whole embryo (165x186x172 μ m) within about 17 minutes (smaller than the transition time to the next stage), while still retaining a sufficiently high resolution to visualize subcellular structures.

We also imaged a later stage (late tailbud I) with the E-LSBM modality (figure 5.29a-c). Here, by looking at the membranes stained with the lipophilic dye FM4-64, Ulla could segment three different tissue types in the head of the embryo: epidermis, central nervous system (CNS) and mesoderm/endoderm. Using this segmentation, I generated the violin plot in figure 5.29d, which shows different distributions for the three tissue types, suggesting that they have different mechanical properties.

We proceeded to image three embryos for 14 hours with a time resolution of 30min, not observing significant changes of the Brillouin shift of the different tissue types but demonstrating that we could follow development over a long period of time without apparent photodamage in this time window.

In conclusion, by looking at an early stage of *Pallusia*, we demonstrated that the high resolution of the LSBM allowed us to detect subcellular modulations in mechanical properties; at a later stage, the possibility of imaging large volumes, in combination with the concurrent SPIM modality, allowed us to segment different tissue types and determine their mechanical properties in 3D.

5.5.3 Mouse embryo development

The mouse embryo is a widely used and notoriously light sensitive model organism. To test whether the reduced phototoxicity of the O-LSBM allows imaging of such a delicate sample, we performed volumetric imaging of six embryos over two days with a time resolution of approximately 1 hour and a half and less than 20mW optical power on the sample, in the time window from early morula to late blastocyst (figure 5.30a). The design of the microscope was critical to keeping the embryos in physiological conditions while following development. First of all, mouse embryos are typically cultured in micro-drops of medium covered by mineral oil to prevent evaporation, while conventional sample mounting techniques for lightsheet microscopy rely on embedding the sample in an agarose cylinder and thus they are not compatible with mouse embryos. Following Strnad et al. [122], we designed a sample holder with a groove that can support a thin FEP foil (see section 5.2.1). The embryos can sit at the bottom of individual micro-wells (created by "deforming" the foil with a glass capillary having a closed tip of about 100 μ m) filled

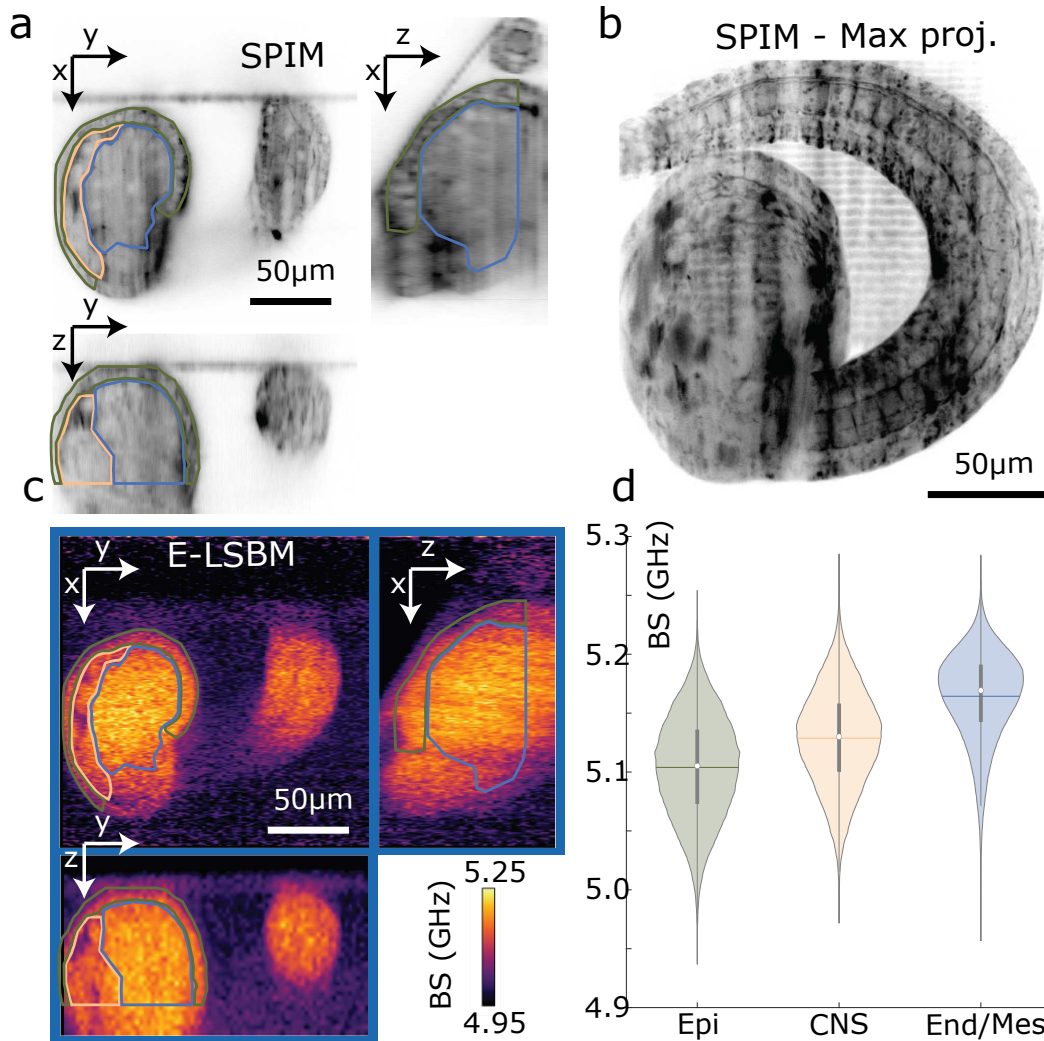


FIGURE 5.29: Imaging of a *Phallusia* embryo at the tailbud stage (out 389 of $n = 3$ total) (a-d). Orthogonal views (a) and maximum intensity projection (MIP) (b) from the SPIM volume ($195\mu\text{m} \times 191\mu\text{m} \times 111\mu\text{m}$) of membranes labeled with lipophilic dye FM4-64 of a *Phallusia* embryo at the tailbud stage (late tailbud I). Corresponding orthogonal views (c), acquired with E-LSBM modality, of the volume in panel a. Violin plot (d) showing the Brillouin shift differences of three distinct tissue regions (Epidermis, Central Nervous System (CNS) and Endoderm/Mesoderm) manually-segmented in 3D according to SPIM data in a. The green, yellow and light-blue outlines in panels a and c show the segmented regions for Epidermis, CNS and Endoderm/Mesoderm respectively. BS, Brillouin shift. Figure adapted from [65].

with the medium and covered with oil. Additionally, the temperature needs to be kept at 37C and the CO₂ at 5%: this was achieved by enclosing the imaging chamber with a 3D printed cover, heating the immersion water of the objective with resistors, controlled via a feedback loop, and flowing pre-mixed air+CO₂ at the adequate concentration inside the chamber (see section 5.3.1.1).

The embryos were derived from a transgenic mouse line having the nuclei fluorescently-labeled (H2B-mCherry) and were micro-injected with mRNA to have fluorescently-labeled membranes (Myr-Palm-iRFP). The samples were prepared and micro-injected by Manuel Eguren and mounted in the imaging chamber by Chii Jou Chan. Four out of six imaged embryos developed properly, as confirmed by morphology - in comparison with embryos that were kept in the same imaging chamber but not imaged - (figure 5.31a) and by cell fate staining and cell number (figure 5.31b). This is in stark contrast with imaging in the 532 confocal Brillouin microscope, where the mouse embryos undergo cell death after imaging a single plane for few timepoints (figure 5.32).

In conclusion, we demonstrated that O-LSBM has sufficiently low phototoxicity to image a very delicate sample (mouse embryo) over two days with a time resolution of about 1 hour and a half.

5.5.4 Conclusions and outlook

I want to summarise the key advancements of the LSBM and the avenues that it could open in biology. We showed that the LSBM enabled, for the first time, the measurement of mechanical properties of entire organisms at high spatial resolution in 3D and over an extended period of time. Indeed we could observe a transient increase in Brillouin shift in different tissue folding processes during *Drosophila* gastrulation (section 5.5.1). This observation required very high temporal resolution (around 2 minutes for each volume, consisting of both fluorescence and Brillouin imaging) in order to follow such fast processes (around 20 minutes). We could also detect differences in the mechanical properties at the subcellular level in *Phallusia*, that are likely related to microtubules (section 5.5.2). Finally, we could follow the development of mouse embryos over 2 days with a time resolution of about 1 hour and a half without observing any apparent photodamage (section 5.5.3).

In conclusion, the reduced phototoxicity and the improved acquisition time of the LSBM could open exciting avenues in mechanobiology and, in

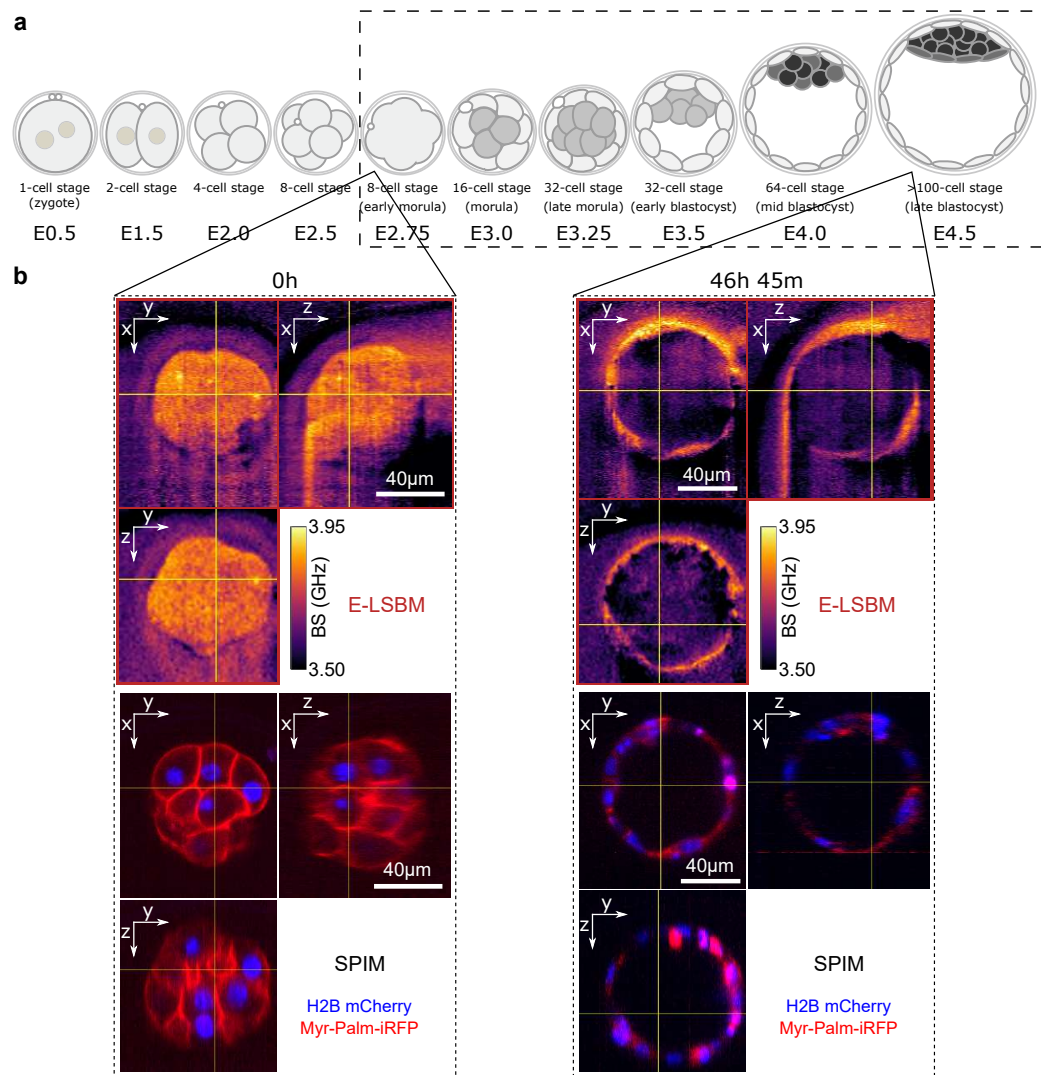


FIGURE 5.30: (a) Timeline of mouse embryo development from the one cell stage to late blastocyst. The dashed rectangle encloses the developmental window that was imaged. (b) Exemplary orthogonal views of Brillouin volumes (top, acquired in the O-LSBM) and SPIM volumes (bottom) of a single mouse embryo at the beginning (left) and at end of the timelapse (right, 46h45m after the first timepoint). The acquisition time for one volume in the Brillouin modality was 11-17min, the time interval between volumes is between 77 to 92 minutes. Representative result from $n=4$ embryos. Figure adapted from [65].

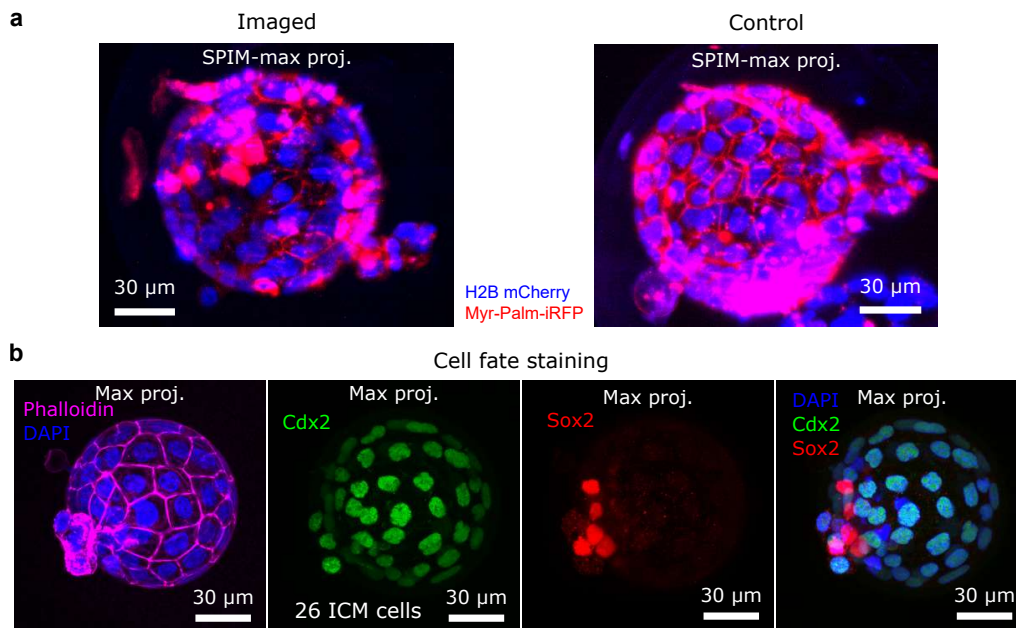


FIGURE 5.31: (a) Top: SPIM volume (maximum intensity projection - MIP) of an embryo that underwent Brillouin time-lapse imaging, taken at the end of the timelapse. Bottom: SPIM image (MIP) of a control embryo (taken at the same time as the embryo in top panel), that was in the same imaging chamber but not imaged by Brillouin or SPIM, showing qualitatively similar morphology. (b) To further confirm embryo viability, we fixed the embryos after imaging and stained them for cell fate. MIPs through the volume where the outer trophoctoderm cells are CDX2-positive (green), a marker for trophoctoderm cell fate. The inner cell mass are SOX2-positive (red) and CDX2-negative, indicating proper epiblast fate in the ICM at late blastocyst stage. The number of cells in the ICM is 26, consistent with the reported values in literature [130]. Figure adapted from [65].

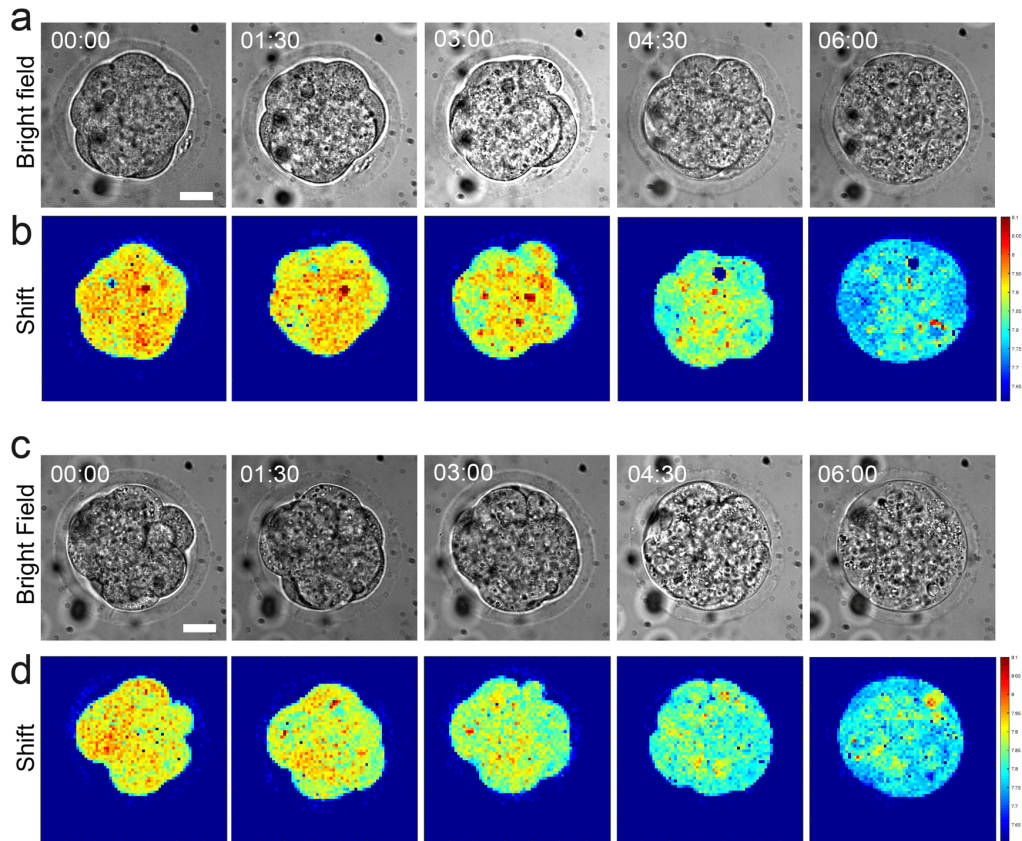


FIGURE 5.32: a. Brightfield images of an 8-cell stage mouse embryo that eventually undergoes cell death. b. Images of Brillouin shift for the same embryo in (a), showing a loss of Brillouin signals within 6 hours, which is a clear sign of embryo death. The embryo also appears round and decompact, a sign of abnormality. c. Another representative embryo undergoing cell death under the same imaging condition. Time is shown in hh:mm. Scale bar = 20 μm . Data collected by Chii Jou Chan. Figure taken from [65] and made by Chii Jou Chan.

particular, in the study of developmental processes. Here, the mechanical information provided by the LSBM could be correlated with cell fate or molecular information provided by fluorescence reporters or with ultra-structural information provided by electron microscopy. That would help get a more complete picture of developmental processes, which encompass a complex interplay between genetics, biochemical signal and mechanics, where the latter is still not as extensively explored as the others [4].

Chapter 6

Outlook and conclusions

In the last chapter I want to discuss about the future directions of Brillouin microscopy that can be explored in our lab and, more in general, what is the foreseeable future in the Bio-Brillouin field.

In the last decade Brillouin microscopy has emerged to be a powerful tool to study the role of mechanical properties not only in biological processes at the cellular and organismal level but also in diseases diagnosis and treatment. Yet a deep understanding of the physical origin of Brillouin signal in complex, heterogeneous materials, such as biological samples, is lacking. This issue can be approached from different directions. A bottom-up approach can be used, whereby few cell constituents are combined *in vitro* and the viscoelastic properties of the mixture are analyzed under varying conditions. Along that line, Scarcelli et al. [49] showed that the Brillouin shift of reconstituted actin gels increases during actin polymerization and branching of actin fibers. Additionally, the Guck lab [33] explored the Brillouin signature of phase-separated protein aggregates both *in vitro* and in living cells. Such studies could provide insights in systems with lower complexity which might be the building blocks to understanding more complex biological systems. Another approach would be to use theoretical modeling, together with numerical simulation, of cells and tissues to understand how the mechanical properties and dynamics of the single constituents contribute to the measured longitudinal modulus. Finally, following what has already been done in several studies [49, 50, 52], drug perturbations of the main cytoskeletal components (actin, microtubules) can be performed and the change in Brillouin signature measured. The studies have so far focused on single cells and the perturbation experiments were rather reported as validation for Brillouin microscopy. Performing more systematic experiments, extending them on organismal or tissue scale and taking advantage of optogenetic tools (that allow to alter cellular constituents with high temporal and spatial selectivity) could help unravel the contribution of cytoskeletal components to tissue elasticity.

Altogether the final goal should be to understand the role of high-frequency longitudinal (Brillouin) modulus in biological processes, which could prove to be itself relevant, without assuming that is a proxy for the quasi-static Young's modulus.

The advancement in the fundamental understanding of the physical origin of the Brillouin signal in biological samples should go hand-in-hand with further improvement of the instrumentation. My PhD work was in that direction. In fact, I improved a state-of-the-art confocal Brillouin setup to make it suitable for addressing biological questions and easy to use by non-experts. I also designed and built a line-scanning Brillouin microscope (LSBM) that improves the speed by a factor of 100 over the confocal implementation while ensuring physiological mounting of the sample, low photodamage and high spatial resolution. LSBM opened the doors to studying fast processes and light-sensitive samples that were not accessible before. Depending on the requirements of the specific experiment, both setups can be used in the future in our lab to address new biological questions or investigate the origin of Brillouin signal (as I highlighted in the previous paragraph). In particular, the confocal Brillouin setup is more suited for experiments where very high spatial resolution and mounting of the sample in standard dishes or coverslips are favored over fast acquisition and low photodamage.

In future LSBM can be further improved by combining it with an optical method which can measure the refractive index in 3D (e.g. holography-based [124] or intensity-based [125] reconstruction algorithms). The advantage of having a 3D map of refractive index would be twofold: on one side, one could numerically simulate the effect of refraction and determine the scattering angle at each point so that the image quality can be improved in the O-LSBM modality (see section 5.2.6); on the other side, refractive index, together with fluorescence imaging of lipids, can be used to convert Brillouin shift to the actual longitudinal modulus (see section 2.5 and Schlüßler et al. [33]).

On the instrument side, another direction that we are exploring in our lab is the use of stimulated Brillouin microscopy [37]. It is based on the transfer of energy between two counterpropagating beams (pump and probe) when the difference in their optical frequencies is matching the natural frequency of the acoustic wave. Being a stimulated process, it overcomes the main limitation of spontaneous Brillouin scattering (that is low cross section, thus weak signal) and the signal can be detected electronically with a lock-in amplifier without needing a spectrometer. Despite the complication of needing optical

access from two opposite sides of the sample, it has the potential to reduce the acquisition time, have high spectral resolution and allows the determination of material density within the scattering volume from the signal intensity. I collaborated with Fan Yang, who designed and built a stimulated Brillouin microscope that uses pulsed pump and probe (in contrast with the first demonstration by Remer et al. [37] that used CW lasers) and can thus achieve the same SNR with much lower power.

Appendix A

VIPA dispersion and spectrometer calibration

A.1 VIPA dispersion

Xiao, Weiner, and Lin [131] derived the dispersion law for VIPA using the Fresnel diffraction analysis. Solving equation (14) from their paper for θ_λ and taking the first order approximation in θ_i (the typical incidence angle is few degrees):

$$\theta_\lambda \approx -\theta_i \pm \sqrt{2n} \sqrt{1 - \frac{m\lambda}{2nt}} \quad (\text{A.1})$$

where n is the refractive index of the VIPA, m is the interference order and the other parameters are shown in figure A.1. By squaring equation A.1:

$$m\lambda \approx 2nt \left[1 - \frac{(\theta_\lambda + \theta_i)^2}{2n^2} \right] \quad (\text{A.2})$$

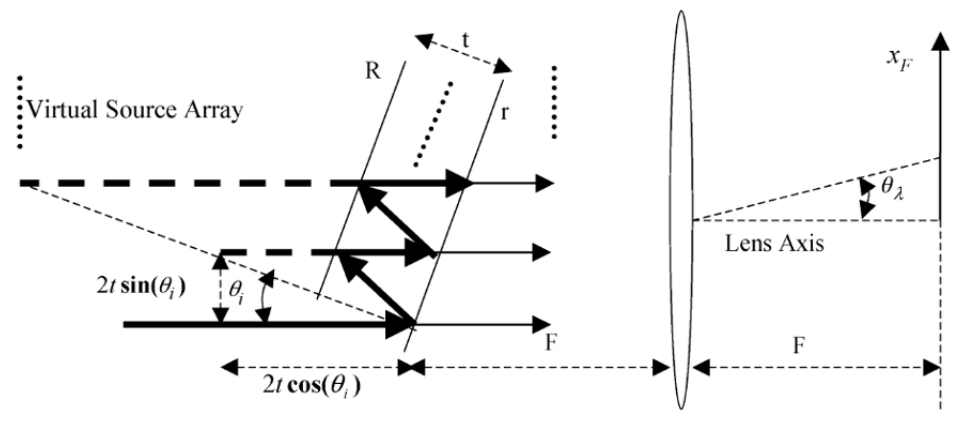


FIGURE A.1: Schematic of the VIPA with the relevant parameters from [131]

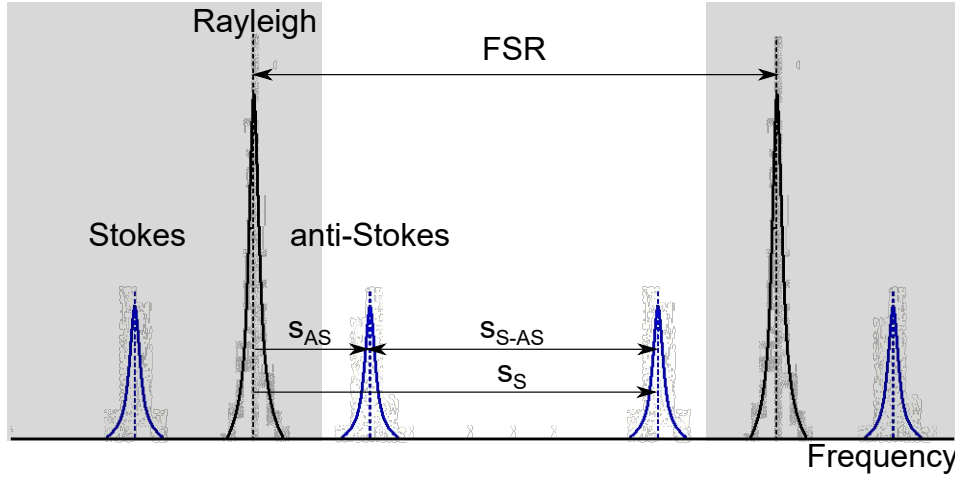


FIGURE A.2: Representation of the periodic pattern created by the spectrometer on the camera. In the confocal Brillouin microscope, the shaded grey area is not accessible during the measurement because is blocked by the slits.

Given that the position on the camera is proportional to $\tan(\theta_\lambda) \approx \theta_\lambda$ (the largest angle that is imaged on the camera is $\approx 0.04rad$), the diffraction order or the wavelength depends on the square of the position on the camera. Note that, in general, the change in wavelength $\Delta\lambda$ is not proportional to the change in frequency $\Delta\nu$ (equivalent to the Brillouin shift s) because they are inversely proportional ($\nu\lambda = c$). But since the typical frequency shifts are on the order of 0.001% of the optical frequency the approximation $s \propto \Delta\lambda$ is very good.

In conclusion, in our experimental conditions, $m \cdot s$ can be expressed as a second order polynomial of the position on the camera.

A.2 Two-stage VIPA spectrometer calibration

Figure A.2 shows the pattern created by the spectrometer on the camera. The objective is to measure s_{AS} but it is not possible to do it directly since the strong laser peaks are blocked by the slits. From the figure it is clear that the measurement of s_{S-AS} and the knowledge of FSR allows to calculate

$$s_{AS} = \frac{FSR - s_{S-AS}}{2} \quad (A.3)$$

s_{S-AS} is measured from the distance between the Stokes and anti-Stokes peaks in pixels and must be converted to GHz in order to apply equation A.3. As shown in section A.1, the generic relationship between the distance

in pixels d and the frequency shift s can be written as:

$$s = \alpha \cdot d^2 + \beta \cdot d \quad (\text{A.4})$$

Keeping the same convention for the subscripts of d as the ones for s , one can write:

$$s_{S-AS} = s_S - s_{AS} = \alpha \cdot (d_S^2 - d_{AS}^2) + \beta \cdot (d_S - d_{AS}) = (d_S - d_{AS}) \cdot [\alpha \cdot (d_S + d_{AS}) + \beta] \quad (\text{A.5})$$

$d_{meas} = d_S - d_{AS}$ is the distance between the Stokes and anti-Stokes peaks in pixel that is measured directly, while $k = d_S + d_{AS}$ cannot be measured. Intuitively k should be similar to the FSR in pixels (indeed it would be exactly that if the dispersion of the VIPA were linear), thus be constant. In that case,

$$s_{S-AS} = c \cdot d_{meas} \quad (\text{A.6})$$

where $c = \alpha \cdot k + \beta \approx const.$ I will show that the approximation is valid in our experimental conditions.

By collecting a spectrum where both the water signal and the laser peaks are visible and fitting the peaks with a Lorentzian function I found:

First laser peak	0
anti-Stokes peak	64.4px
Stokes peak	207.0px
Second laser peak	288.1px

Using the Brillouin shift of water from literature ($\Omega_{H_2O} = 7.46\text{GHz}$ from [83]) and the FSR of the VIPA from the manufacturer (30GHz) I calculated $\alpha = -5.65 \cdot 10^{-5}\text{GHz}/\text{px}^2$ and $\beta = 0.12\text{GHz}/\text{px}$.

Using equation A.4 to calculate k at the Brillouin shift of water k_{H_2O} and at 1GHz above the Brillouin shift of water¹ $k_{H_2O+1\text{GHz}}$, I found $k_{H_2O} = 272.35\text{px}$ and $k_{H_2O+1\text{GHz}} = 270.96\text{px}$. This corresponds to $c_{H_2O} = 0.10461\text{GHz}/\text{px}$ and $c_{H_2O+1\text{GHz}} = 0.10469\text{GHz}/\text{px}$, that are the same within less than 0.1% error.

Therefore equation A.6 is valid with constant c and, by combining it with equation A.3,

$$c = \frac{FSR - 2\Omega_{H_2O}}{d_{meas}^{H_2O}} \quad (\text{A.7})$$

$d_{meas}^{H_2O}$ is measured from the spectrum of the water in the calibration arm.

¹Typical biological samples are within this range.

A.3 Line-scanning spectrometer calibration

As already described in section 5.3.3, the Rayleigh light coming from different spatial positions in the sample is dispersed into a curved line by the spectrometer. In this section I will show that its shape can be approximated by an ellipse.

Calling α_i and θ_i the angles to the normal of the VIPA, the angles inside the VIPA (after the refraction at the interface between air and glass, whose refractive index is n) are $\alpha_{in} \approx \alpha_i/n$ and $\theta_{in} \approx \theta_i/n$ (the approximation is valid for small angles). In the approximation of geometrical optics, the optical path length difference between two subsequent virtual sources is:

$$OPL = 2nt\sqrt{\cos^2(\alpha_{in}) + \cos^2(\theta_{in})} \quad (\text{A.8})$$

where t is the thickness of the VIPA.

Since $\alpha_{in}, \theta_{in} \ll 1$, $\cos^2(\alpha_{in}) \approx 1 - \alpha_{in}^2$ and $\cos^2(\theta_{in}) \approx 1 - \theta_{in}^2$. Under the same approximation, the position on the camera x and y are given by $x = f_1 \tan \theta_i \approx n \cdot f_1 \theta_{in}$ and $y = f_2 \tan \alpha_i \approx n \cdot f_2 \alpha_{in}$, where f_1 and f_2 are the focal lengths of the two cylindrical lenses after the VIPA.

Under the previous approximations:

$$OPL \approx 2t\sqrt{2n^2 - \left(\frac{x}{f_1}\right)^2 - \left(\frac{y}{f_2}\right)^2} \quad (\text{A.9})$$

In order to have constructive interference the condition $OPL = m \cdot \lambda$ must hold:

$$m^2\left(\frac{\lambda}{2t}\right)^2 = 2n^2 - \left(\frac{x}{f_1}\right)^2 - \left(\frac{y}{f_2}\right)^2 \quad (\text{A.10})$$

Introducing the parameters $a = \frac{\lambda f_1}{2t}$, $b = \frac{f_2}{f_1}a$ and $A = \frac{8n^2 t^2}{\lambda^2}$ the previous equation can be written as:

$$\left(\frac{x}{a}\right)^2 + \left(\frac{y}{b}\right)^2 = A^2 - m^2 \quad (\text{A.11})$$

that is the equation of an ellipse.

Bibliography

- [1] Robert Prevedel et al. “Brillouin microscopy: an emerging tool for mechanobiology”. In: *Nature methods* 16.10 (2019), pp. 969–977.
- [2] Ray Keller. “Physical biology returns to morphogenesis”. In: *Science* 338.6104 (2012), pp. 201–203.
- [3] Jeroen Eyckmans et al. “A hitchhiker’s guide to mechanobiology”. In: *Developmental cell* 21.1 (2011), pp. 35–47.
- [4] M Shane Hutson and Xiaoyan Ma. “Mechanical aspects of developmental biology: perspectives on growth and form in the (post)-genomic age”. In: *Physical biology* 5.1 (2008), p. 015001.
- [5] Gabriel YH Lee and Chwee T Lim. “Biomechanics approaches to studying human diseases”. In: *Trends in biotechnology* 25.3 (2007), pp. 111–118.
- [6] Yanping Cao et al. “Elastodiagnosis of diseases: A review”. In: *Extreme Mechanics Letters* 27 (2019), pp. 102–123.
- [7] Jochen Guck et al. “Optical deformability as an inherent cell marker for testing malignant transformation and metastatic competence”. In: *Biophysical journal* 88.5 (2005), pp. 3689–3698.
- [8] Adam J Engler et al. “Matrix elasticity directs stem cell lineage specification”. In: *Cell* 126.4 (2006), pp. 677–689.
- [9] Mei Rosa Ng et al. “Substrate stiffness regulates cadherin-dependent collective migration through myosin-II contractility”. In: *Journal of Cell Biology* 199.3 (2012), pp. 545–563.
- [10] Michael Krieg et al. “Atomic force microscopy-based mechanobiology”. In: *Nature Reviews Physics* 1.1 (2019), pp. 41–57.
- [11] Robert M Hochmuth. “Micropipette aspiration of living cells”. In: *Journal of biomechanics* 33.1 (2000), pp. 15–22.
- [12] Oliver Otto et al. “Real-time deformability cytometry: on-the-fly cell mechanical phenotyping”. In: *Nature methods* 12.3 (2015), pp. 199–202.

- [13] Hu Zhang and Kuo-Kang Liu. "Optical tweezers for single cells". In: *Journal of the Royal Society interface* 5.24 (2008), pp. 671–690.
- [14] Friedhelm Serwane et al. "In vivo quantification of spatially varying mechanical properties in developing tissues". In: *Nature methods* 14.2 (2017), pp. 181–186.
- [15] Brendan F Kennedy, Philip Wijesinghe, and David D Sampson. "The emergence of optical elastography in biomedicine". In: *Nature Photonics* 11.4 (2017), pp. 215–221.
- [16] Antonio Fiore, Carlo Bevilacqua, and Giuliano Scarcelli. "Direct three-dimensional measurement of refractive index via dual photon-phonon scattering". In: *Physical review letters* 122.10 (2019), p. 103901.
- [17] Robert W Boyd. *Nonlinear optics*. Academic press, 2020.
- [18] Moonseok Kim et al. "Shear Brillouin light scattering microscope". In: *Optics Express* 24.1 (2016), pp. 319–328.
- [19] Fedor I Fedorov. *Theory of elastic waves in crystals*. Springer Science & Business Media, 2013.
- [20] *Isotropic elasticity: Longitudinal Modulus and Young's Modulus*. <http://koski.ucdavis.edu/BRILLOUIN/CRYSTALS/LongitudinalModulus.html>. Accessed: 2022-06-07.
- [21] Kristie J Koski et al. "Non-invasive determination of the complete elastic moduli of spider silks". In: *Nature materials* 12.3 (2013), pp. 262–267.
- [22] D Ouis. "On the frequency dependence of the modulus of elasticity of wood". In: *Wood science and technology* 36.4 (2002), pp. 335–346.
- [23] Sara Mattana et al. "Viscoelasticity of amyloid plaques in transgenic mouse brain studied by Brillouin microspectroscopy and correlative Raman analysis". In: *Journal of innovative optical health sciences* 10.06 (2017), p. 1742001.
- [24] Michelle Bailey et al. "Viscoelastic properties of biopolymer hydrogels determined by Brillouin spectroscopy: A probe of tissue micromechanics". In: *Science advances* 6.44 (2020), eabc1937.
- [25] *Resolution Criteria and Performance Issues*. <https://www.olympus-lifescience.com/de/microscope-resource/primer/digitalimaging/deconvolution/deconresolution/>. Accessed: 2022-06-09.

- [26] Silvia Caponi, Daniele Fioretto, and Maurizio Mattarelli. "On the actual spatial resolution of Brillouin Imaging". In: *Optics Letters* 45.5 (2020), pp. 1063–1066.
- [27] Yangang Liu and Peter H Daum. "Relationship of refractive index to mass density and self-consistency of mixing rules for multicomponent mixtures like ambient aerosols". In: *Journal of Aerosol Science* 39.11 (2008), pp. 974–986.
- [28] Robert Barer. "Refractometry and interferometry of living cells". In: *JOSA* 47.6 (1957), pp. 545–556.
- [29] Huaying Zhao, Patrick H Brown, and Peter Schuck. "On the distribution of protein refractive index increments". In: *Biophysical journal* 100.9 (2011), pp. 2309–2317.
- [30] Raimund Schlüßler et al. "Mechanical mapping of spinal cord growth and repair in living zebrafish larvae by Brillouin imaging". In: *Biophysical journal* 115.5 (2018), pp. 911–923.
- [31] Patricia Yang Liu et al. "Cell refractive index for cell biology and disease diagnosis: past, present and future". In: *Lab on a Chip* 16.4 (2016), pp. 634–644.
- [32] Giuliano Scarcelli, Roberto Pineda, and Seok Hyun Yun. "Brillouin optical microscopy for corneal biomechanics". In: *Investigative ophthalmology & visual science* 53.1 (2012), pp. 185–190.
- [33] Raimund Schlüßler et al. "Correlative all-optical quantification of mass density and mechanics of subcellular compartments with fluorescence specificity". In: *Elife* 11 (2022), e68490.
- [34] Giuseppe Antonacci et al. "Spectral broadening in Brillouin imaging". In: *Applied Physics Letters* 103.22 (2013), p. 221105.
- [35] Kareem Elsayad et al. "Mechanical Properties of cellulose fibers measured by Brillouin spectroscopy". In: *Cellulose* 27.8 (2020), pp. 4209–4220.
- [36] Carlo Bevilacqua et al. "Imaging mechanical properties of sub-micron ECM in live zebrafish using Brillouin microscopy". In: *Biomedical Optics Express* 10.3 (2019), pp. 1420–1431.
- [37] Itay Remer et al. "High-sensitivity and high-specificity biomechanical imaging by stimulated Brillouin scattering microscopy". In: *Nature Methods* 17.9 (2020), pp. 913–916.

- [38] Jeremie Margueritat et al. "High-frequency mechanical properties of tumors measured by Brillouin light scattering". In: *Physical review letters* 122.1 (2019), p. 018101.
- [39] Chii Jou Chan, Carlo Bevilacqua, and Robert Prevedel. "Mechanical mapping of mammalian follicle development using Brillouin microscopy". In: *Communications biology* 4.1 (2021), pp. 1–10.
- [40] F Palombo et al. "Mechanical mapping with chemical specificity by confocal Brillouin and Raman microscopy". In: *Analyst* 139.4 (2014), pp. 729–733.
- [41] Antonio Fiore. "Brillouin confocal microscopy in off-axis configuration". PhD thesis. University of Maryland, College Park, 2021.
- [42] Giuliano Scarcelli, Pilhan Kim, and Seok Hyun Yun. "In vivo measurement of age-related stiffening in the crystalline lens by Brillouin optical microscopy". In: *Biophysical journal* 101.6 (2011), pp. 1539–1545.
- [43] Francesca Palombo and Daniele Fioretto. "Brillouin light scattering: applications in biomedical sciences". In: *Chemical reviews* 119.13 (2019), pp. 7833–7847.
- [44] Kareem Elsayad, Silvia Polakova, and Juraj Gregan. "Probing mechanical properties in biology using Brillouin microscopy". In: *Trends in Cell Biology* 29.8 (2019), pp. 608–611.
- [45] Christine Poon et al. "Brillouin imaging for studies of micromechanics in biology and biomedicine: from current state-of-the-art to future clinical translation". In: *Journal of Physics: Photonics* 3.1 (2020), p. 012002.
- [46] Giuseppe Antonacci et al. "Recent progress and current opinions in Brillouin microscopy for life science applications". In: *Biophysical Reviews* 12.3 (2020), pp. 615–624.
- [47] Rafael J Jiménez Rioboó et al. "Brillouin Spectroscopy: From Biomedical Research to New Generation Pathology Diagnosis". In: *International Journal of Molecular Sciences* 22.15 (2021), p. 8055.
- [48] Giuseppe Antonacci et al. "Background-deflection Brillouin microscopy reveals altered biomechanics of intracellular stress granules by ALS protein FUS". In: *Communications biology* 1.1 (2018), pp. 1–8.
- [49] Giuliano Scarcelli et al. "Noncontact three-dimensional mapping of intracellular hydromechanical properties by Brillouin microscopy". In: *Nature methods* 12.12 (2015), pp. 1132–1134.

- [50] Giuseppe Antonacci and Sietse Braakman. “Biomechanics of subcellular structures by non-invasive Brillouin microscopy”. In: *Scientific Reports* 6.1 (2016), pp. 1–6.
- [51] Stefano Coppola et al. “Quantifying cellular forces and biomechanical properties by correlative micropillar traction force and Brillouin microscopy”. In: *Biomedical optics express* 10.5 (2019), pp. 2202–2212.
- [52] Jitao Zhang et al. “Nuclear mechanics within intact cells is regulated by cytoskeletal network and internal nanostructures”. In: *Small* 16.18 (2020), p. 1907688.
- [53] Jitao Zhang et al. “Brillouin flow cytometry for label-free mechanical phenotyping of the nucleus”. In: *Lab on a Chip* 17.4 (2017), pp. 663–670.
- [54] Sara Mattana et al. “Non-contact mechanical and chemical analysis of single living cells by microspectroscopic techniques”. In: *Light: Science & Applications* 7.2 (2018), pp. 17139–17139.
- [55] Jan Rix et al. “Correlation of biomechanics and cancer cell phenotype by combined Brillouin and Raman spectroscopy of U87-MG glioblastoma cells”. In: *bioRxiv* (2022).
- [56] Marketa Samalova et al. “Expansin-controlled cell wall stiffness regulates root growth in Arabidopsis”. In: *BioRxiv* (2020).
- [57] Kareem Elsayad et al. “Mapping the subcellular mechanical properties of live cells in tissues with fluorescence emission–Brillouin imaging”. In: *Science signaling* 9.435 (2016), rs5–rs5.
- [58] Bara Altartouri et al. “Pectin chemistry and cellulose crystallinity govern pavement cell morphogenesis in a multi-step mechanism”. In: *Plant physiology* 181.1 (2019), pp. 127–141.
- [59] Bacete Laura et al. “THESEUS1 modulates cell wall stiffness and abscisic acid production in Arabidopsis thaliana”. In: (2022).
- [60] Daniel R Williams et al. “Elasticity of bamboo fiber variants from Brillouin spectroscopy”. In: *Materialia* 5 (2019), p. 100240.
- [61] Camilo Riquelme-Guzmán et al. “In vivo assessment of mechanical properties during axolotl development and regeneration using confocal Brillouin microscopy”. In: *bioRxiv* (2022). DOI: [10.1101/2022.03.01.482501](https://doi.org/10.1101/2022.03.01.482501). eprint: <https://www.biorxiv.org/content/early/2022/03/04/2022.03.01.482501.full.pdf>. URL: <https://www.biorxiv.org/content/early/2022/03/04/2022.03.01.482501>.

- [62] Jitao Zhang et al. "Tissue biomechanics during cranial neural tube closure measured by Brillouin microscopy and optical coherence tomography". In: *Birth defects research* 111.14 (2019), pp. 991–998.
- [63] Rana Amini et al. "Amoeboid-like migration ensures correct horizontal cell layer formation in the developing vertebrate retina". In: *eLife* 11 (May 2022). Ed. by Marianne E Bronner, e76408. ISSN: 2050-084X. DOI: [10.7554/eLife.76408](https://doi.org/10.7554/eLife.76408). URL: <https://doi.org/10.7554/eLife.76408>.
- [64] Florian Geisler et al. "Intestinal intermediate filament polypeptides in *C. elegans*: Common and isotype-specific contributions to intestinal ultrastructure and function". In: *Scientific reports* 10.1 (2020), pp. 1–18.
- [65] Carlo Bevilacqua et al. "High-resolution line-scan Brillouin microscopy for live-imaging of mechanical properties during embryo development". In: *bioRxiv* (2022). DOI: [10.1101/2022.04.25.489364](https://doi.org/10.1101/2022.04.25.489364). eprint: <https://www.biorxiv.org/content/early/2022/04/26/2022.04.25.489364.full.pdf>. URL: <https://www.biorxiv.org/content/early/2022/04/26/2022.04.25.489364>.
- [66] Ekaterina Pukhlyakova et al. " β -Catenin-dependent mechanotransduction dates back to the common ancestor of Cnidaria and Bilateria". In: *Proceedings of the National Academy of Sciences* 115.24 (2018), pp. 6231–6236.
- [67] Francesca Palombo et al. "Chemico-mechanical imaging of Barrett's oesophagus". In: *Journal of biophotonics* 9.7 (2016), pp. 694–700.
- [68] Zachary Steelman et al. "Brillouin spectroscopy as a new method of screening for increased CSF total protein during bacterial meningitis". In: *Journal of biophotonics* 8.5 (2015), pp. 408–414.
- [69] WHO: *cardiovascular diseases*. <https://www.who.int/health-topics/cardiovascular-diseases>. Accessed: 2022-06-05.
- [70] Giuseppe Antonacci et al. "Quantification of plaque stiffness by Brillouin microscopy in experimental thin cap fibroatheroma". In: *Journal of the Royal Society Interface* 12.112 (2015), p. 20150843.
- [71] Anett Jannasch et al. "Brillouin Spectroscopy as an Innovative Tool to Investigate Biomechanical Properties of Native Human Aortic Valve and Bioprostheses Tissue". In: *Structural Heart* 5 (2021), p. 29.

- [72] María Villalba-Orero et al. "Assessment of myocardial viscoelasticity with Brillouin spectroscopy in myocardial infarction and aortic stenosis models". In: *Scientific reports* 11.1 (2021), pp. 1–15.
- [73] Maria Troyanova-Wood et al. "Optical assessment of changes in mechanical and chemical properties of adipose tissue in diet-induced obese rats". In: *Journal of biophotonics* 10.12 (2017), pp. 1694–1702.
- [74] Sara Mattana et al. "Viscoelasticity of amyloid plaques in transgenic mouse brain studied by Brillouin microspectroscopy and correlative Raman analysis". In: *Journal of innovative optical health sciences* 10.06 (2017), p. 1742001.
- [75] Francesca Palombo et al. "Hyperspectral analysis applied to micro-Brillouin maps of amyloid-beta plaques in Alzheimer's disease brains". In: *Analyst* 143.24 (2018), pp. 6095–6102.
- [76] Tijana Lainović et al. "Micromechanical imaging of dentin with Brillouin microscopy". In: *Acta Biomaterialia* 105 (2020), pp. 214–222.
- [77] Pei-Jung Wu et al. "Detection of proteoglycan loss from articular cartilage using Brillouin microscopy, with applications to osteoarthritis". In: *Biomedical optics express* 10.5 (2019), pp. 2457–2466.
- [78] Irina V Kabakova et al. "Fiber-integrated Brillouin microspectroscopy: towards Brillouin endoscopy". In: *Journal of Innovative Optical Health Sciences* 10.06 (2017), p. 1742002.
- [79] YuChen Xiang et al. "Background-free fibre optic Brillouin probe for remote mapping of micromechanics". In: *Biomedical optics express* 11.11 (2020), pp. 6687–6698.
- [80] Seungmi Ryu et al. "Label-free histological imaging of tissues using Brillouin light scattering contrast". In: *Biomedical optics express* 12.3 (2021), pp. 1437–1448.
- [81] Rafael J Jiménez Riobóo, Manuel Desco, and María Victoria Gómez-Gavero. "Impact of optical tissue clearing on the Brillouin signal from biological tissue samples". In: *Biomedical Optics Express* 10.6 (2019), pp. 2674–2683.
- [82] JM Vaughan and JT Randall. "Brillouin scattering, density and elastic properties of the lens and cornea of the eye". In: *Nature* 284.5755 (1980), pp. 489–491.

- [83] Giuliano Scarcelli and Seok Hyun Yun. "Confocal Brillouin microscopy for three-dimensional mechanical imaging". In: *Nature photonics* 2.1 (2008), pp. 39–43.
- [84] Giuliano Scarcelli and Seok Hyun Yun. "In vivo Brillouin optical microscopy of the human eye". In: *Optics express* 20.8 (2012), pp. 9197–9202.
- [85] Sheldon T Bailey et al. "Light-scattering study of the normal human eye lens: elastic properties and age dependence". In: *IEEE transactions on biomedical engineering* 57.12 (2010), pp. 2910–2917.
- [86] Stephan Reiß et al. "Spatially resolved Brillouin spectroscopy to determine the rheological properties of the eye lens". In: *Biomedical optics express* 2.8 (2011), pp. 2144–2159.
- [87] Joshua N Webb et al. "Detecting mechanical anisotropy of the cornea using Brillouin microscopy". In: *Translational Vision Science & Technology* 9.7 (2020), pp. 26–26.
- [88] Amira M Eltony, Peng Shao, and Seok-Hyun Yun. "Measuring mechanical anisotropy of the cornea with Brillouin microscopy". In: *Nature Communications* 13.1 (2022), pp. 1–11.
- [89] Seok Hyun Yun and Dimitri Chernyak. "Brillouin microscopy: assessing ocular tissue biomechanics". In: *Current opinion in ophthalmology* 29.4 (2018), p. 299.
- [90] Sebastien Besner et al. "In vivo Brillouin analysis of the aging crystalline lens". In: *Investigative ophthalmology & visual science* 57.13 (2016), pp. 5093–5100.
- [91] Giuliano Scarcelli et al. "Biomechanical characterization of keratoconus corneas ex vivo with Brillouin microscopy". In: *Investigative ophthalmology & visual science* 55.7 (2014), pp. 4490–4495.
- [92] Giuliano Scarcelli et al. "In vivo biomechanical mapping of normal and keratoconus corneas". In: *JAMA ophthalmology* 133.4 (2015), pp. 480–482.
- [93] Theo G Seiler et al. "Brillouin spectroscopy of normal and keratoconus corneas". In: *American journal of ophthalmology* 202 (2019), pp. 118–125.
- [94] Peng Shao et al. "Spatially-resolved Brillouin spectroscopy reveals biomechanical abnormalities in mild to advanced keratoconus in vivo". In: *Scientific reports* 9.1 (2019), pp. 1–12.

- [95] Giuliano Scarcelli et al. "Brillouin microscopy of collagen crosslinking: noncontact depth-dependent analysis of corneal elastic modulus". In: *Investigative ophthalmology & visual science* 54.2 (2013), pp. 1418–1425.
- [96] Sheldon JJ Kwok et al. "Selective two-photon collagen crosslinking in situ measured by Brillouin microscopy". In: *Optica* 3.5 (2016), pp. 469–472.
- [97] Joshua N Webb, Johnny P Su, and Giuliano Scarcelli. "Mechanical outcome of accelerated corneal crosslinking evaluated by Brillouin microscopy". In: *Journal of Cataract & Refractive Surgery* 43.11 (2017), pp. 1458–1463.
- [98] Hongyuan Zhang et al. "Depth-dependent reduction of biomechanical efficacy of contact lens–assisted corneal cross-linking analyzed by Brillouin microscopy". In: *Journal of Refractive Surgery* 35.11 (2019), pp. 721–728.
- [99] Hongyuan Zhang et al. "Brillouin microscopic depth-dependent analysis of corneal crosslinking performed over or under the LASIK flap". In: *Journal of Cataract & Refractive Surgery* 46.11 (2020), pp. 1543–1547.
- [100] Guillaume Lepert et al. "Assessing corneal biomechanics with Brillouin spectro-microscopy". In: *Faraday discussions* 187 (2016), pp. 415–428.
- [101] Peng Shao et al. "Effects of corneal hydration on Brillouin microscopy in vivo". In: *Investigative ophthalmology & visual science* 59.7 (2018), pp. 3020–3027.
- [102] Amira M Eltony et al. "Longitudinal Brillouin measurements of the human cornea before and after LASIK". In: *Investigative Ophthalmology & Visual Science* 59.9 (2018), pp. 1400–1400.
- [103] Yogeshwari S Ambekar et al. "Multimodal quantitative optical elastography of the crystalline lens with optical coherence elastography and Brillouin microscopy". In: *Biomedical Optics Express* 11.4 (2020), pp. 2041–2051.
- [104] Christina Conrad et al. "Mechanical characterization of 3D ovarian cancer nodules using Brillouin confocal microscopy". In: *Cellular and molecular bioengineering* 12.3 (2019), pp. 215–226.

- [105] Vaibhav Mahajan et al. “Mapping tumor spheroid mechanics in dependence of 3D microenvironment stiffness and degradability by Brillouin microscopy”. In: *Cancers* 13.21 (2021), p. 5549.
- [106] Miloš Nikolić, Giuliano Scarcelli, and Kandice Tanner. “Multimodal microscale mechanical mapping of cancer cells in complex microenvironments”. In: *bioRxiv* (2022). DOI: [10.1101/2022.03.28.486131](https://doi.org/10.1101/2022.03.28.486131). eprint: <https://www.biorxiv.org/content/early/2022/03/29/2022.03.28.486131.full.pdf>. URL: <https://www.biorxiv.org/content/early/2022/03/29/2022.03.28.486131>.
- [107] Anya B Roberts et al. “Tumor cell nuclei soften during transendothelial migration”. In: *Journal of Biomechanics* 121 (2021), p. 110400.
- [108] Maria Troyanova-Wood, Zhaokai Meng, and Vladislav V Yakovlev. “Differentiating melanoma and healthy tissues based on elasticity-specific Brillouin microspectroscopy”. In: *Biomedical optics express* 10.4 (2019), pp. 1774–1781.
- [109] Miloš Nikolić and Giuliano Scarcelli. “Long-term Brillouin imaging of live cells with reduced absorption-mediated damage at 660nm wavelength”. In: *Biomedical Optics Express* 10.4 (2019), pp. 1567–1580.
- [110] Giuliano Scarcelli and Seok Hyun Yun. “Multistage VIPA etalons for high-extinction parallel Brillouin spectroscopy”. In: *Optics express* 19.11 (2011), pp. 10913–10922.
- [111] Guqi Yan et al. “Evaluation of commercial virtually imaged phase array and Fabry-Pérot based Brillouin spectrometers for applications to biology”. In: *Biomedical optics express* 11.12 (2020), pp. 6933–6944.
- [112] Eitan Edrei, Malte C Gather, and Giuliano Scarcelli. “Integration of spectral coronagraphy within VIPA-based spectrometers for high extinction Brillouin imaging”. In: *Optics express* 25.6 (2017), pp. 6895–6903.
- [113] Johannes Schindelin et al. “Fiji: an open-source platform for biological-image analysis”. In: *Nature methods* 9.7 (2012), pp. 676–682.
- [114] Derek L Stemple. “Structure and function of the notochord: an essential organ for chordate development”. In: (2005).
- [115] John M Gansner et al. “Essential role of lysyl oxidases in notochord development”. In: *Developmental biology* 307.2 (2007), pp. 202–213.

- [116] Francesca Palombo et al. “Biomechanics of fibrous proteins of the extracellular matrix studied by Brillouin scattering”. In: *Journal of The Royal Society Interface* 11.101 (2014), p. 20140739.
- [117] Go Nagamatsu et al. “Mechanical stress accompanied with nuclear rotation is involved in the dormant state of mouse oocytes”. In: *Science advances* 5.6 (2019), eaav9960.
- [118] Thomas IR Hopkins et al. “Micromechanical mapping of the intact ovary interior reveals contrasting mechanical roles for follicles and stroma”. In: *Biomaterials* 277 (2021), p. 121099.
- [119] Hosein Kafian et al. “Light-sheet fluorescence microscopy with scanning non-diffracting beams”. In: *Scientific reports* 10.1 (2020), pp. 1–12.
- [120] Emmanuel G Reynaud et al. “Light sheet-based fluorescence microscopy: more dimensions, more photons, and less photodamage”. In: *HFSP journal* 2.5 (2008), pp. 266–275.
- [121] Jitao Zhang et al. “Line-scanning Brillouin microscopy for rapid non-invasive mechanical imaging”. In: *Scientific reports* 6.1 (2016), pp. 1–8.
- [122] Petr Strnad et al. “Inverted light-sheet microscope for imaging mouse pre-implantation development”. In: *Nature methods* 13.2 (2016), pp. 139–142.
- [123] Loïc A Royer et al. “Adaptive light-sheet microscopy for long-term, high-resolution imaging in living organisms”. In: *Nature biotechnology* 34.12 (2016), pp. 1267–1278.
- [124] Mirjam Schürmann et al. “Refractive index measurements of single, spherical cells using digital holographic microscopy”. In: *Methods in cell biology*. Vol. 125. Elsevier, 2015, pp. 143–159.
- [125] Shwetadwip Chowdhury et al. “High-resolution 3D refractive index microscopy of multiple-scattering samples from intensity images”. In: *Optica* 6.9 (2019), pp. 1211–1219.
- [126] Jakub Czuchnowski and Robert Prevedel. “Improving the sensitivity of planar fabry–pérot cavities via adaptive optics and mode filtering”. In: *Advanced Optical Materials* 9.4 (2021), p. 2001337.
- [127] Adam C Martin. “The physical mechanisms of *Drosophila* gastrulation: mesoderm and endoderm invagination”. In: *Genetics* 214.3 (2020), pp. 543–560.

-
- [128] Hanna L Sladitschek et al. “MorphoSeq: Full single-cell transcriptome dynamics up to gastrulation in a chordate”. In: *Cell* 181.4 (2020), pp. 922–935.
- [129] Takahito Nishikata, Taku Hibino, and Hiroki Nishida. “The centrosome-attracting body, microtubule system, and posterior egg cytoplasm are involved in positioning of cleavage planes in the ascidian embryo”. In: *Developmental biology* 209.1 (1999), pp. 72–85.
- [130] Chii Jou Chan et al. “Hydraulic control of mammalian embryo size and cell fate”. In: *Nature* 571.7763 (2019), pp. 112–116.
- [131] Shijun Xiao, Andrew M Weiner, and Christopher Lin. “A dispersion law for virtually imaged phased-array spectral dispersers based on paraxial wave theory”. In: *IEEE journal of quantum electronics* 40.4 (2004), pp. 420–426.